Politecnico di Torino

Mathematical Engineering

Master's Thesis

Quantifying the impact of vessel topology on oxygen supply to the brain

Author:

Zorzi Emilio

External supervisors:

Gaia Stievano, Dr. Franca Schmid

Internal supervisor:

Prof. Stefano Scialò

Index

Zorzi Emilio - Master's thesis

Emilio Zorzi

October 2025

Abstract

Blood flow disturbances within the brain microvasculature may cause microinfarcts, which are associated with the development of neurodegenerative diseases. Understanding oxygen dynamics in the brain tissue surrounding the microvasculature is essential to assess the vascular network's robustness to microinfarcts. This work investigates whether local blood flow direction influences the contribution of individual vessels to cerebral oxygen supply. An *in silico* approach is adopted, since direct measurements of oxygen concentration are limited. Computational models of blood flow and oxygen dynamics are developed and applied. Simulations are performed on a realistic microvascular network extracted from a mouse somatosensory cortex. The variable *vessel topology* is introduced, classifying vessels into four groups, called *topological configurations*, based on local blood flow direction. Then, additional oxygen-related and topological variables, directly linked to oxygen supply, are defined. The impact of vessel topology is assessed based on the distribution of these variables across different topological configurations. Results indicate that different topological configurations have different roles in oxygen supply to the brain. Vessels with one inflow and two outflows, that tend to be closer to arterioles, most strongly affect oxygen distribution throughout the microvasculature and local tissue oxygenation. In contrast, vessels with one inflow and one outflow are the most important for overall brain oxygenation, efficiently releasing oxygen into the surrounding tissue. However, the microvascular network is globally resistant to their occlusion. Since the majority of blood vessels have one inflow and one outflow, these findings point to an inherent resilience of the brain microvasculature to microinfarcts.

1 Introduction

1.1 Research context and motivation

The brain microvasculature is a network of minute blood vessels responsible for brain oxygenation [Hoque et al., 2021]. Blood flow disturbances within the brain microvasculature may cause local tissue lesions, known as *microinfarcts* [Smith et al., 2012]. Microinfarcts are associated with the development of neurodegenerative diseases such as Alzheimer's disease [Corrada et al., 2016][Kövari et al., 2013]. Moreover, several studies show evidence of correlation between vascular disorders and cognitive decline [Moeini et al., 2018]. To assess the robustness of the microvasculature in this context, it is fundamental to understand the contribution of individual vessels to cerebral oxygen supply. In the past decades, *in vivo* analyses have been conducted in this direction [Nishimura et al., 2007] [Shih et al., 2013] [Lecoq et al., 2011]. However, these studies are limited by the difficulty in measuring oxygen concentration [Zhang et al., 2015]. Furthermore, as certain techniques are complex, they often involve substantial uncertainty and high costs. To overcome these limitations, computational modeling has been introduced [Lücker, 2017].

Accordingly, the current study adopts an *in silico* approach, based on the blood flow model presented in [Schmid et al., 2021], which evaluated the effects of local occlusions on tissue perfusion. Building on this blood flow model, an oxygen supply model is incorporated, resulting in a coupled framework for simulating both perfusion and oxygen delivery. The results of the oxygen simulations are used to assess whether local blood flow direction affects the contribution of individual vessels to cerebral oxygen supply. If this were the case, conclusions about vessels' contributions could be drawn using only the blood flow model. This would eliminate the need for the oxygen supply model and result in a substantial computational saving.

1.2 Biological background

The physiology of oxygen supply to the brain is described, encompassing the key anatomical elements that support it.

1.2.1 Blood

The first anatomical element described is blood, the medium through which oxygen reaches the brain. Blood is a suspension consisting of a liquid part, called the plasma, and of a cellular part, that is composed of three different cell types: white blood cells (leukocytes), platelets (thrombocytes) and red blood cells (erythrocytes), which will be called RBCs hereafter (see figure 1.1).

Plasma is primarily composed of water and exhibits the properties of a fluid.

White blood cells play a role in the human immune response, whereas platelets are involved in the repair of blood vessels injury by coagulation.

RBCs are the most frequent cells, they show a special *biconcave* shape and their diameter is just 6 μm, making them able to pass through the thinnest blood vessels. They are the main characters for oxygen supply. The absence of a nucleus allows them to store the so called *hemoglobin*, a protein that chemically binds to oxygen. Moreover, the special biconcave shape maximises the surface area for the oxygen diffusion across the RBC membrane. RBCs volume

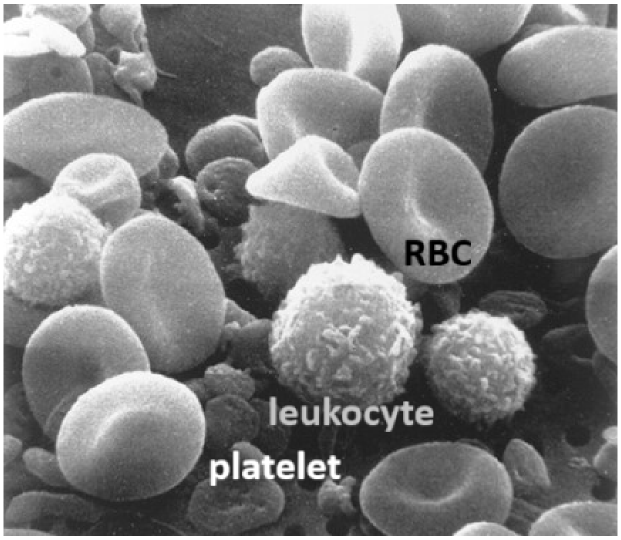

Figure 1.1: Microscopic scan of blood. It is possibe to observe the RBCs, with their tipical biconcave shape, the small disc-shaped platelets and the leukocytes. Image by Bruce Wetzel and Harry Schaefer, from US National Cancer Institute (see `https://visualsonline.cancer.gov/details.cfm?imageid=2129`).

.

fraction in the blood is called hematocrit [Dean, 2005].

1.2.2 Heart and blood vessel

Blood reaches the brain through the cardiovascular system, which is composed of the heart and a network of blood vessels that branch throughout the body.

The heart serves as the primary muscular organ driving the cardiovascular system. This organ is made up of two separate pumps: a *right heart* that sends blood towards the lungs and a *left heart* that pumps it to the organs in the body [Rehman and Rehman, 2023]. The network of blood vessels allows circulation throughout the body. It is possible to distinguish three categories of blood vessels: arteries, that perfuse the tissues, veins, which bring back waste and blood to excretory organs and the heart, and capillaries, the thinnest ones [Taylor and Bordoni, 2025] (in humans, they show a diameter between $4\,\mu m$ and $9\,\mu m$ [Hall and Hall, 2020]). Arteries and veins with a diameter greater than $0.1 - 0.2\,mm$ are involved in the *macrocirculation*, which is primarily responsible for delivering blood flow to organs and back to the heart [Feihl et al., 2009]. The remaining vessels function within the *microcirculation*, where most oxygen exchange takes place [Taylor and Bordoni, 2025]. Oxygen molecules dissociate from hemoglobin in RBCs and travel through plasma and the capillary wall to reach the surrounding cells. This occurs via a diffusion process driven by an oxygen gradient pointing outward from the vessels [Lücker, 2017].

1.2.3 Brain

As mentioned in the introduction, this work focuses on brain microcirculation. To gain a deeper understanding of this process, it is thus necessary to consider the anatomy of the brain.

The human brain is the most complicated organ in the human body. Its presence is essential for a huge number of tasks, including movement, senses, thinking, language and memory [Maldonado and Alsayouri, 2025]. These actions are conducted thanks to the collaboration of more than 100 billion cells, called neurons. Neurons exhibit a high metabolic rate, making the brain unable to rely on anaerobic metabolism. Moreover, the brain is a highly demanding organ, consuming about 15% of the cardiac output, even if its total mass is 2% of the total body mass. These facts make its resistance to the absence of oxygen limited [Hall and Hall, 2020].

From a cardiovascular standpoint, the brain is supplied by the cerebral blood network through four major arteries that converge to form the so-called *circle of Willis*. The arteries originat-

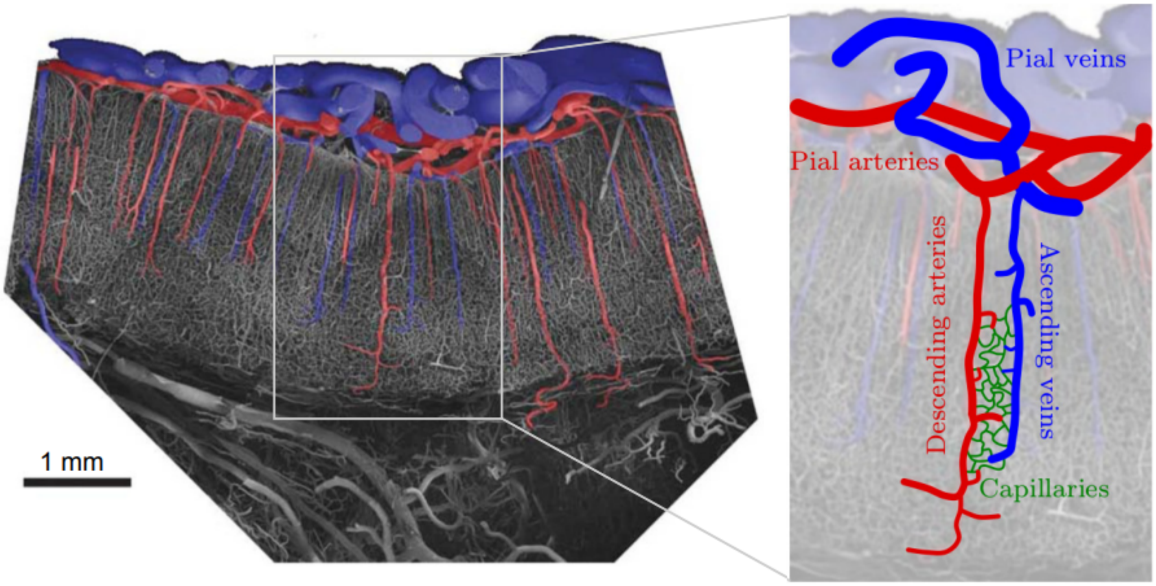

Figure 1.2: Vascular structure of the brain of a monkey. Arteries and arterioles are coloured with red, while veins and venules are in blue. On the left, general perspective of the brain vasculature. On the right, focus on the microcirculation. Pial arteries and veins, arterioles, venules and capillaries are shown. Images by [Hirsch et al., 2012], composed by [Schmid et al., 2017a].

.

ing from the circle of Willis (pial arteries) cover the brain surface, and then penetrate the brain mass branching out into smaller vessels, the descending arteries and arterioles. From these, the capillaries arise [Hall and Hall, 2020]. Then, blood is collected by venules and ascending veins, and is subsequently conveyed by the venous circulation back to the heart [Agarwal and Carare, 2021]. Figure 1.2 illustrates the vascular structure of a monkey brain cortex, whose anatomy closely resembles that of the human brain. [Schmid, 2017].
The brain is characterized by a complex structure: it is composed of different interconnected regions associated with different functions [Sultana et al., 2024]. In the course of this project, the somatosensory region of the cerebral cortex is considered.

1.2.4 Cerebral cortex and somatosensory cortex

The cerebral cortex is the outermost layer of the brain, with a thickness ranging from 2 mm to 4 mm. It is responsible for awareness, communication, memory, sensation, understanding and voluntary movements. Even if its mass is about 40% of the overall brain mass, it makes up 75% of the neuron cell bodies (or *neuron somata*)[1] [Moini et al., 2023]. The somatosen-

---

[1] These are the "central hubs" of the neuron.

sory cortex is the region of the cerebral cortex devoted to the elaboration of environmental stimuli [Raju and Tadi, 2025].
The mouse and human anatomies are analogous with respect to the physiology of oxygen supply to the brain [Schmid et al., 2017b]. This justifies the use of data from the somatosensory cortex of the mouse brain (see figure 1.3) for the simulations performed in this work.

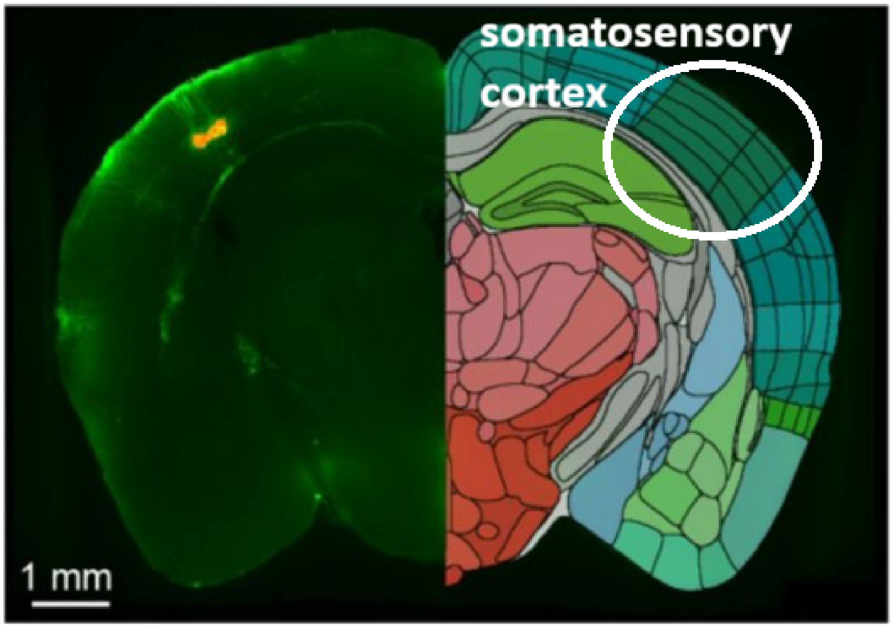

Figure 1.3: Brain mouse section, where the somatosensory cortex is highlighted. The left image is obtained using a green color raw fluorescence signal. The right is obtained via an axon segmentation, that allows one to recognise the different areas of the mouse brain. From [Liu et al., 2024].

.

1.3 History of oxygen supply modeling

An overview of the history of modeling the oxygen supply process is presented here, following [Lücker, 2017].

The first model was developed by August Krogh in 1919 [Krogh, 1919]. He idealized capillaries as cylinders, each surrounded by a cylindrical tissue domain (Krogh cylinder), disregarding variations of oxygen within the capillaries. Using several additional assumptions and with the assistance of mathematician K. Erlang, he derived the Krogh-Erlang equation, which describes the distribution of oxygen partial pressure within the tissue domain. Despite its approximations, this equation continues to serve as a benchmark for modeling tissue oxygen tension.

The perspective changed in 1977, when Hellums incorporated oxygen partial pressure variations within capillaries by explicitly considering the presence of RBCs [Hellums, 1977].

In the following decades, several studies refined Krogh's model by relaxing its assumptions and including additional mechanisms, such as oxygen-hemoglobin kinetics. However, the original cylindrical geometry was preserved [Goldman, 2008].

From the late 1970s onward, oxygen transport modeling advanced toward more realistic geometries. Popel [Popel, 1978] introduced models of parallel capillary arrays that exhibited characteristics distinct from those of the original Krogh model. Later, Secomb and Hsu [Secomb and Hsu, 1988] proposed the Green's function method for network-level modeling, while Goldman and Popel [Goldman and Popel, 2000] applied finite difference techniques to complex capillary networks. Subsequent studies expanded these models to include arterioles, venules [Goldman, 2008], and the explicit role of red blood cells in intravascular transport [Hellums, 1977] [Eggleton et al., 2000] [Goldman and Popel, 2000], linking microscopic oxygen dynamics to whole-network behavior.

In the past decade, Lücker [Lücker, 2017] presented a numerical model for oxygen supply to the brain. This model was designed to enable direct comparison with experimental measurements and to illustrate the physics of capillary-to-tissue oxygen delivery. Nevertheless, it employs approximating assumptions, including approximate hemoglobin–oxygen kinetics. Therefore, the model provides an incomplete description of oxygen transport within the microvasculature.

The numerical framework developed in the present work is based on the approach of Koch [Koch, 2022], which introduced a model for simulating mass transport within thin tubular networks and its exchange with the surrounding tissue. In the present study, this model is extended to simulate oxygen supply to the brain, linking vessel-level dynamics to tissue oxygenation.

1.4 Outline

The overall structure of the thesis is now outlined:

- chapter 2 describes the models and simulations implemented in this work [Stievano, nd], along with the dataset employed [Blinder et al., 2013];
- in chapter 3, vessel topology is introduced. This is a categorical variable that classifies the vessels into four different groups, called topological configurations, based on local

blood flow direction [Schmid et al., 2021];

- in chapters 3 and 4, other variables are presented. They allow for an understanding of the structural and functional differences between topological configurations, as each one of them establishes a ranking among the groups;
- a rigorous statistical analysis, aimed at confirming the observed differences between topological configurations, is subsequently conducted in chapter 5;
- in chapter 6, conclusions are drawn about the impact of vessel topology on brain oxygenation, based on the rankings derived from the other analysed variables.

2 Models and simulations

2.1 Introduction

This chapter shows the mathematical and numerical frameworks that are used for assessing the importance of vessels on brain oxygenation. The purpose is to convey the main ideas behind the models and the simulations, so that the reader can understand the analyses in chapters 3 and 4. Two models, along with their associated simulation tools, are introduced: the blood flow model, concerning blood flow in the brain microvasculature, and the oxygen supply model, involving oxygen delivery from blood to brain tissue. As mentioned in section 1.1, the latter builds upon the first: the oxygen supply model requires information about blood flow in the microvasculature.
First, in section 2.2, the blood flow model is presented. The foundation of this model lies in the Hagen-Poiseuille flow in a single capillary, whereas the communication between blood vessels is regulated by a series of empirical laws. Numerical simulations are then run, performed through a solver called MicroBloom. In section 2.3, the oxygen supply framework is described. Starting from the biological mechanism, a suitable model is shown, considering two interacting compartments, microvasculature and brain tissue, guaranteeing mass conservation. The DuMux software is then presented as a solver of the PDEs equations governing the problem, in order to obtain the functions describing oxygen distribution in brain tissue and blood vessels. Finally, the dataset used in simulations is presented in section 2.4.

2.2 Blood flow

2.2.1 Model

A continuous approach is adopted for the blood flow model. Blood is considered as a homogeneous and Newtonian fluid within each capillary. In the microcirculation setting, the Reynolds number is extremely small [Cho and Cho, 2011], implying that viscous forces outweigh inertial ones. Thus, a creeping-flow regime can be considered. Moreover, the weight of blood in capillaries is negligible. The pulsatile effects due to the heart beats are also disregarded, so that the problem is considered as stationary. Therefore, the Navier-Stokes equations governing blood motion along each capillary can be rewritten as:

$$\begin{cases} -\nabla \mathcal{P}(\boldsymbol{x}) + \mu \Delta \boldsymbol{u}(\boldsymbol{x}) = 0 \\ \nabla \cdot \boldsymbol{u}(\boldsymbol{x}) = 0 \end{cases} \tag{2.1}$$

where the first equation represents the *momentum balance* and the second one the *mass conservation* equation. With regard to the meaning of the variables, $\boldsymbol{u}(\boldsymbol{x}) \in \mathbb{R}^3$ is the blood velocity (each component is measured in m s^{-1}), $\mathcal{P}(\boldsymbol{x}) \in \mathbb{R}$ its pressure (in mmHg) and $\mu \in \mathbb{R}$ its viscosity (in mmHg·s). All these variables are evaluated in a point $\boldsymbol{x}$.

Furthermore, geometrical assumptions are made about the shape of capillaries. They are considered as straight rigid cylinders, that show a constant circular cross-section, with diameter $D = 2a$ (measured in m). The letter L represents their length (in m). Finally, significant remarks are made about the behaviour of the pressure function $\mathcal{P}(\boldsymbol{x})$. Its value is set to be constant on the circular cross-section. Its partial derivative $-\partial_x \mathcal{P}$ is fixed along the axis of the cylinder and equal to $\frac{\Delta \mathcal{P}}{L}$. $\Delta \mathcal{P}$ indicates the difference in pressure between the endpoints of the capillary. Consequently, the assumptions of the Hagen-Poiseuille flow model (see figure 2.1) are satisfied. It is possible to express the volumetric flow rate of blood Q (measured in m^{3}s^{-1}), that is simply called *blood flow* hereafter, as:

$$Q = \frac{\Delta \mathcal{P}}{R}, \quad R = \frac{128 \mu L}{\pi D^4} \tag{2.2}$$

where R is called the *hydraulic resistance* of the capillary. Note that the derivation of 2.2 presented is in line with standard hemodynamic practice [Chandran et al., 2012].

The presence of RBCs is addressed via the hematocrit (see section 1.2.1). To be precise, the adimensional variable *discharged* hematocrit H_D is introduced. This indicates the RBC fraction that you could collect in a reservoir if you cut a capillary and let the blood flow into it for an interval of time Δt [Obrist, 2022]. The movement of RBCs is modelled according to an empirical law, that is reported in [Pries et al., 1990] (phase separation). The Fåhræus effect [Barbee and Cokelet, 1971], typical of microcirculation, is neglected: the velocity of plasma and RBCs are considered the same. Moreover, the Fåhræus-Lindqvist effect [Toksvang and Berg, 2013] is not incorporated, implying that the viscosity of blood is constant across capillaries regardless of their diameter.

The purpose of the blood flow model is to retrieve the values of Q, H_D and $\Delta \mathcal{P}$ across the

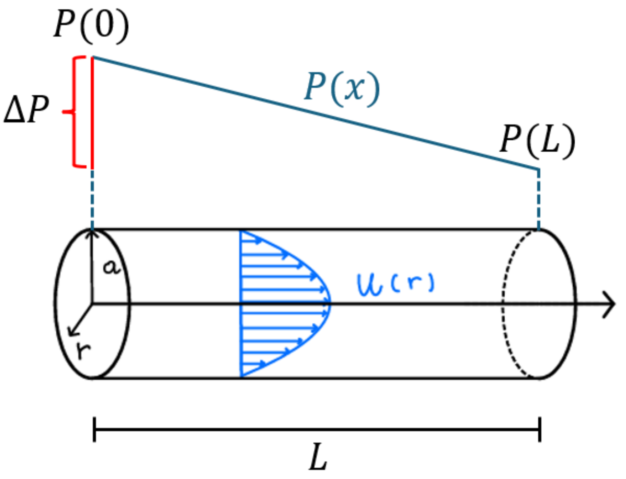

Figure 2.1: Hagen-Poiseuille flow model. Adapted from: Ridolfi, L. & Camporeale, C., *Dispense di Meccanica dei Fluidi*

.

whole microvasculature. To this end, equation 2.2 is applied to each capillary. The values of D, L, μ are known, as well as pressure $\mathcal{P}$ on the inflow and outflow points of the microvasculature [Schmid et al., 2017b]. Conservation of mass at each bifurcation k, i.e. between communicating capillaries, is also ensured, both for blood and RBCs:

$$\begin{cases} \sum\limits_{e_k \in E_k} Q_{e_k} = 0 \\ \sum\limits_{e_k \in E_k} (Q_{e_k} H_{D,e_k}) = 0 \end{cases} \tag{2.3}$$

where E_k is the set of edges incident to k. Moreover, the relationship among the H_D values of the edges in E_k, for each bifurcation k, is governed by the previously mentioned phase separation law. The blood flow value Q of the edges is required for the empirical relationship, making it interdependent with equations 2.2 and 2.3. [Pries et al., 1990].

2.2.2 MicroBloom

The model presented does not admit an analytical solution. As a consequence, a numerical solver called MicroBloom is employed [Schmid et al., 2017b]. This solver adopts an iterative approach, that involves variables $\Delta\mathcal{P}$, Q and H_D. At the beginning, it initialises H_D with predefined values across all the vessels. Afterwards, at every iteration:

- it first updates the parameters Q and $\Delta\mathcal{P}$. This is done by solving the linear system derived from equations 2.2 and 2.3 for each capillary, with H_D held fixed. Note that μ is set to 0.0012 mmHg·s in each capillary of the microvasculature;
- it then updates H_D according to the empirical law in [Pries et al., 1990], with Q held fixed.

This procedure is stopped when convergence is reached. Convergence is defined based on the differences between blood flow values at subsequent iterations. The full documentation for MicroBloom can be found on the github page `https://github.com/Franculino/microBloom/tree/57ba603`.

2.3 Oxygen supply

Building on the blood flow field in the microvasculature computed by MicroBloom, oxygen supply to the brain can be modelled and simulated in order to obtain an accurate description of its distribution in this organ. As described in section 1.2, oxygen reaches the brain through the bloodstream, and is released towards the neurons thanks to a diffusive process that exploits the difference of oxygen concentration between the inside of the vessels and the brain tissue. The structure of this perfusing mechanism suggests considering it as the product of two processes that communicate: the oxygen advection throughout the network and the oxygen diffusion into the tissue. From a mathematical standpoint, this situation can be described through an embedded model, portraying the microvasculature as *embedded* in the brain tissue.

Note that the model that is presented has been developed by Gaia Stievano, PhD student at Bern University and member of the CVE group at ARTORG centre for Biomedical Engineering Research [Stievano, nd].

2.3.1 1d-3d embedded model

The model is aimed at understanding oxygen distribution in the brain tissue. Throughout the whole work, the presence of oxygen, both in blood and tissues, is quantified by its partial pressure, measured in mmHg (as in [Lücker, 2017]). The expression P_l is used to refer to this variable, where l is the location where the partial pressure is considered. In order to obtain the gas concentration, it is sufficient to multiply P_l by a solubility coefficient α_l, measured in $\mathrm{m}^3\mathrm{O}_2$ mmHg^{-1} m^{-3} (also depending on l).

It is important to point out that time t is disregarded in the model. Indeed, the focus is on looking for a stationary solution, that describes brain oxygenation at a physiological equilib-

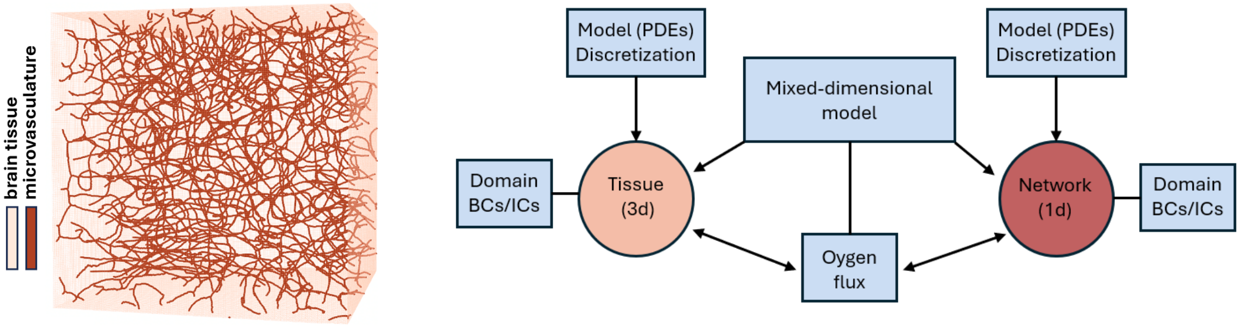

Figure 2.2: On the left, visual representation of the embedded model in a section of the microvascular network. On the right, scheme of the embedded model functioning. Images by Stievano, Gaia

rium.

The model presented is *mixed-dimensional*: capillaries in the vascular network are regarded as being 1d, whereas the tissue in which they are embedded has a 3d structure. Consequently, capillaries are here treated as segments. This choice implies the use of volumetric flow rates and averaged variables over the radial component, that is motivated by a great improvement in computational efficiency [Koch et al., 2018]. A 3d resolution of all the capillaries would require a high computational cost, especially considering the already intricate network structure.

Concerning the structure of the two compartments of the problem, both the 3d and the 1d models show their own partial differential equations, boundary and initial conditions (see figure 2.2). The 3d model describes oxygen diffusion in the brain tissue, whereas the 1d model depicts oxygen advection throughout the brain microvasculature. Their interaction consists in the outflux of oxygen from blood vessels into the tissue, that will be called *transmembrane flux* from now on, as it goes through the *membrane* of the capillaries. Note that, to be precise, this flow is bidirectional, as in some rare cases the flux can go from the tissue into the vessel.

The mathematical description of this interaction is now given. Let Λ indicate the vascular 1d domain, parametrized by λ and Ω the tissue 3d domain, whose points are $x \in \mathbb{R}^3$. The set of points $x \in \Omega$ that lie on the vasculature will be called Ω_Λ. The mapping $\lambda(\cdot)$ allows to retrieve the parameter $\lambda(x)$ corresponding to a point $x \in \Omega_\Lambda$. Moreover, let $\hat{q}_c$ be the transmembrane flux density in the 1d vasculature setting (measured in $\mathrm{m}^3\mathrm{O}_2\ \mathrm{s}^{-1}\ \mathrm{m}^{-1}$, negative when exiting capillaries) and let q_c be the transmembrane flux density in the 3d setting (measured in $\mathrm{m}^3\mathrm{O}_2\ \mathrm{s}^{-1}\ \mathrm{m}^{-3}$, positive when entering tissue). It is possible to define their relation in the following way:

$$\begin{cases} q_c(x) = -\hat{q}_c(\lambda(x))\delta_\Lambda(x) & x \in \Omega_\Lambda \\ q_c(x) = 0 & x \in \Omega \setminus \Omega_\Lambda \end{cases} \tag{2.4}$$

where $\delta_\Lambda(x)$ is a delta Dirac type function, such that $\int_\Omega \delta_\Lambda(x)dx = \int_\Lambda d\lambda$ and that:

$$\int_\Omega f(x)\delta_\lambda(x)dx = \int_\Lambda f_\Lambda(\lambda)d\lambda, \ \ \forall f_\Lambda \in L^1(\Lambda) \tag{2.5}$$

Here, $f_\Lambda(\lambda(x)) = f(x) \ \forall x \in \Omega_\Lambda$. These definitions imply conservation of mass across the capillary membrane, between the 1d and the 3d compartments (see Appendix 8 for the proof). After having studied the interaction between the two models, attention turns to their individual definition, starting from the 3d model.

2.3.2 3d brain tissue compartment

The PDEs governing the diffusion of oxygen into the brain tissue are now presented. There are three mechanisms that specifically come into play in this setting:

1) the transmembrane flux that comes from the vessels, as seen in the previous section 2.3.1, that can be seen as a *source* of oxygen;
2) the diffusive process in the tissue, that naturally arises when there is a gradient of oxygen concentration in it;
3) the oxygen consumption in the tissue, due to the brain metabolic activity.

As 1) has already been described, the main focus is on the modelling of 2) and 3). Let P_T be the oxygen partial pressure in the tissue. The oxygen concentration is given by $\alpha_T P_T$, where α_T is the solubility coefficient in the tissue, viewed as constant. Concerning 2), it is sufficient to employ a classical diffusion term involving $\alpha_T P_T$, i.e. $\nabla \cdot (D_T \alpha_T \nabla P_T)$, where D_T is the diffusion constant in the tissue (expressed in $\mathrm{m}^2\ \mathrm{s}^{-1}$). Indeed, this term describes the balance of outflux and influx of oxygen concentration in a point due to diffusion. With regard to 3) a nonlinear Michaelis-Menten consumption term $M(P_T)$ is used [Goldman and Popel, 2000]:

$$M(P_T) = M_0 \frac{P_T}{P_T + P_{T,crit}} \tag{2.6}$$

Here, M_0 is the maximal metabolic rate of oxygen consumption (in $\mathrm{m}^3\mathrm{O}_2\ \mathrm{s}^{-1}\ \mathrm{m}^{-3}$), while $P_{T,crit}$ is the value of oxygen partial pressure in the tissue such that the oxygen consumption

is half of M_0 [Goldman and Popel, 2000].
In summary, the following PDE describes the oxygen behaviour in the tissue:

$$-\underbrace{q_C}_{\text{source}}+\underbrace{M(P_T)}_{\text{consumption}}-\underbrace{\nabla\cdot(D_T\alpha_T\nabla P_T)}_{\text{diffusion}}=0 \tag{2.7}$$

2.3.3 1d vascular compartment

The oxygen released in the 3d compartment comes from the 1d one, that is responsible for oxygen advection throughout the microvasculature. To describe this mechanism, it is necessary to model the complex interaction between hemoglobin, RBCs and plasma in terms of oxygen flux in a capillary.
The inside of a capillary is abstractly divided into three sections: oxyhemoglobin (hemoglobin carrying oxygen), RBCs and plasma. RBCs contain oxyhemoglobin, implying that there are no direct interactions between oxyhemoglobin and plasma. In addition to this, RBCs are considered to travel through a circle C_{rbc} concentric with the capillary cross-section A. Note that $r_{C_{rbc}} < a$, where $r_{C_{rbc}}$ is the radius of C_{rbc} and a is the radius of A (as defined in section 2.2.1). Instead, plasma is considered to surround RBCs, flowing through the annulus $A \setminus C_{rbc}$. This implies that no RBC is in contact with the capillary wall, in line with in vitro and in vivo observations[1] [Secomb and Pries, 2013].
Let $\mathcal{F}_l$ represent the oxygen flux along the vessel within compartment $l \in \{rbc, pl, S\}$. Here, *rbc* stands for RBCs, *pl* for plasma and S for *saturation*. S represents the oxyhemoglobin section, since saturation S is an adimensional variable indicating the percentage of hemoglobin that is oxygenated. $\mathcal{F}_l$ is directly linked to the blood flow and hematocrit fields computed by MicroBloom (see section 2.2.2):

$$\mathcal{F}_{rbc} = \alpha_{rbc} P_{rbc} Q H_D \tag{2.8}$$

$$\mathcal{F}_{pl} = \alpha_{pl} P_{pl} Q (1 - H_D) \tag{2.9}$$

$$\mathcal{F}_S = QS \tag{2.10}$$

As mentioned in the introduction, the largest amount of oxygen molecules is bound to hemoglobin, and needs to dissociate from it. After doing that, it can travel through plasma to reach the capillary wall, from where it gets to the tissue. This behaviour is modelled employing three fluxes (see figure 2.3):

---

[1] The formation of a cell-free layer around RBCs is observed. This is also linked to the Fåhræus–Lindqvist effect.

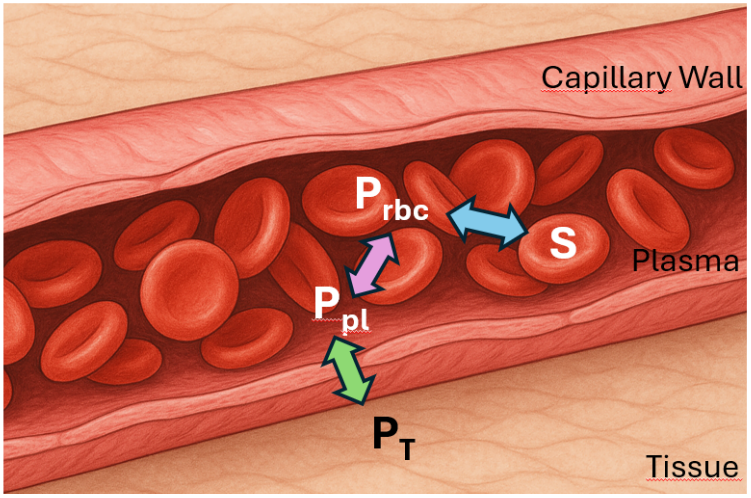

Figure 2.3: Vascular compartment model. In blue $\mathcal{J}(S, P_{rbc})$, in pink $\mathcal{J}(P_{rbc}, P_{pl})$, in green $\hat{q}_c$. Adapted from: Stievano, Gaia [Stievano, nd]

.

1) a bidirectional flux of oxygen from oxyhemoglobin to RBCs, whose linear density is expressed by $\mathcal{J}_1(S, P_{rbc}, H_D)$;
2) a bidirectional flux of oxygen from RBCs to plasma, whose linear density is given by $\mathcal{J}_2(P_{rbc}, P_{pl})$;
3) a flux from plasma into tissue (transmembrane flux), whose linear density is represented by $\hat{q}_c$ (as mentioned in section 2.3.1, in some rare cases this flux can have the opposite direction).

All the linear density of fluxes are expressed in $\mathrm{m}^3\mathrm{O}_2\ \mathrm{s}^{-1}\ \mathrm{m}^{-1}$.
The term $\mathcal{J}_1(S, P_{rbc}, H_D)$ can be written as in [Clark et al., 1985]:

$$\mathcal{J}_1(S, P_{rbc}, H_D) = K\left(S - (1-S)\left(\frac{P_{rbc}}{P_{rbc,50}}\right)^n\right) H_D A_\theta \tag{2.11}$$

where $P_{rbc,50}$ represents the partial pressure in RBCS such that the hemoglobin is half-saturated, A_θ is the cross-sectional area of the vessel (in m^2), K is a dissociation rate constant (in s^{-1}) and n is the so called *Hill exponent* [Lücker, 2017].
The full expression of $\mathcal{J}_2(P_{rbc}, P_{pl})$ is:

$$\mathcal{J}_2(P_{rbc}, P_{pl}) = k_{cell}(P_{rbc} - P_{pl})A_\theta. \tag{2.12}$$

Here, k_{cell} is called the mass transfer coefficient between the RBC and the plasma compartments, expressed in $\mathrm{mmHg}^{-1}\ \mathrm{s}^{-1}$, and A_θ is defined as above.

Finally, following [Koch, 2020], $\hat{q}_C$ can be expressed as:

$$\hat{q}_C = D_W \alpha_{pl}(1-\sigma)(P_T - P_{pl})|C_\theta| \tag{2.13}$$

where D_W is the oxygen diffusion constant in the membrane of the capillary (in $\mathrm{m}^2\ \mathrm{s}^{-1}$), σ is a dimensionless parameter called *oxygen permeability* and $|C_\theta|$ is the length of the circumference of the vessel, measured in m.

To link all the aforementioned oxygen fluxes, the following strategy is employed. Taken an arbitrary $\lambda \in \Lambda$, the difference $\mathcal{F}_l(\lambda + \Delta\lambda) - \mathcal{F}_l(\lambda)$ is expressed by the fluxes between component l and the others (remember that Λ is the vascular domain as described in 2.3.1). In formulas:

(i) $\mathcal{F}_S(\lambda + \Delta\lambda) - \mathcal{F}_S(\lambda) = -\int_\lambda^{\lambda+\Delta\lambda} \mathcal{J}_1(S(\lambda), P_{rbc}(\lambda), H_D(\lambda))d\lambda$;

(ii) $\mathcal{F}_{rbc}(\lambda+\Delta\lambda)-\mathcal{F}_{rbc}(\lambda) = \int_\lambda^{\lambda+\Delta\lambda} \mathcal{J}_1(S(\lambda), P_{rbc}(\lambda), H_D(\lambda))d\lambda - \int_\lambda^{\lambda+\Delta\lambda} \mathcal{J}_2(P_{rbc}(\lambda), P_{pl}(\lambda))d\lambda$;

(iii) $\mathcal{F}_{pl}(\lambda + \Delta\lambda) - \mathcal{F}_{pl}(\lambda) = \int_\lambda^{\lambda+\Delta\lambda} \mathcal{J}_2(P_{rbc}(\lambda), P_{pl}(\lambda))d\lambda + \int_\lambda^{\lambda+\Delta\lambda} \hat{q}_c(P_T(\lambda), P_{pl}(\lambda))d\lambda$.

Dividing both sides of the equations in (i), (ii) and (iii) by $\Delta\lambda$ and considering $\Delta\lambda \to 0$, the PDEs that describe the oxygen behaviour in the 1d vascular compartment are obtained:

$$\begin{cases} \dfrac{\partial \mathcal{F}_S(Q,S)}{\partial \lambda} = -\mathcal{J}_1(S, P_{rbc}, H_D) \\ \dfrac{\partial \mathcal{F}_{rbc}(H_D, Q, P_{rbc})}{\partial \lambda} = \mathcal{J}_1(S, P_{rbc}, H_D) - \mathcal{J}_2(P_{rbc}, P_{pl}) \\ \dfrac{\partial \mathcal{F}_{pl}(H_D, Q, P_{pl})}{\partial \lambda} = \mathcal{J}_2(P_{rbc}, P_{pl}) + \hat{q}_C(P_T, P_{pl}) \end{cases} \tag{2.14}$$

2.3.4 Boundary conditions

The PDEs 2.7 and 2.14 require suitable boundary conditions to be solved.
Concerning the 3d brain tissue compartment Ω, a zero-flux boundary condition is imposed:

$$\frac{\partial P_T(x)}{\partial n} = 0, \ \forall x \in \partial\Omega \tag{2.15}$$

This is a simplification of the oxygen partial pressure behaviour on the boundary, since an oxygen exchange between Ω and the surrounding brain tissue is expected. However, in the absence of data about P_T on $\partial\Omega$, 2.15 is reasonable because it allows one to isolate Ω. Indeed, Ω is treated as if it were solely supplied by the microvasculture Λ embedded in it.

The 1d vascular compartment boundary conditions on P_{rbc}, P_{pl} and S relate to the inflow into the microvasculature Λ and to the outflow out of it. They are of Neumann type. The inflow conditions are given by:

$$\frac{\partial S(\lambda_{in})}{\partial \lambda} = f(\mathcal{F}_{S,in}) \tag{2.16}$$

$$\frac{\partial P_{rbc}(\lambda_{in})}{\partial \lambda} = f(\mathcal{F}_{rbc,in}) \tag{2.17}$$

$$\frac{\partial P_{pl}(\lambda_{in})}{\partial \lambda} = f(\mathcal{F}_{pl,in}) \tag{2.18}$$

for every $\lambda_{in} \in \partial\Lambda$ inflow boundary point. $\mathcal{F}_{S,in}, \mathcal{F}_{rbc,in}$ and $\mathcal{F}_{pl,in}$ are oxygen fluxes based on literature data [Lyons et al., 2016] [Lücker, 2017], while $f(\cdot)$ represents how the DuMux software (see next section) turns these influxes into Neumann conditions[2].
The outflow conditions are defined as:

$$\frac{\partial S(\lambda_{out})}{\partial \lambda} = f(\mathcal{F}_{S}(\lambda_{out})) \tag{2.19}$$

$$\frac{\partial P_{rbc}(\lambda_{out})}{\partial \lambda} = f(\mathcal{F}_{rbc}(\lambda_{out})) \tag{2.20}$$

$$\frac{\partial P_{pl}(\lambda_{out})}{\partial \lambda} = f(\mathcal{F}_{pl}(\lambda_{out})) \tag{2.21}$$

for every $\lambda_{out} \in \partial\Lambda$ outflow boundary point; $f(\cdot)$ is defined as above.
See [Stievano, nd] for further details about boundary conditions.

2.3.5 DuMux setup

The oxygen supply model presented is employed to obtain the distribution of saturation S and of oxygen partial pressure both in the capillary (P_{rbc}, P_{pl}) and in the tissue (P_T). Since there are no analytical solutions to the 2.7 and 2.14 PDEs in the complex geometry of this embedded model, a numerical approach is needed, that involves their discretization in the 3d and 1d domains. This process is performed using the DuMux software, a "simulation framework with a focus on finite volume discretization methods, model coupling for multi-physics applications, and flow and transport applications in porous media" (definition from the DuMux introduction webpage, that can be found at `https://dumux.org/docs/doxygen/master/index.html`). In figure 2.4, DuMux logo is shown. DuMux github page can be found at `https://github.com/dumux`. The Finite Volume Method (FVM) is chosen,

---

[2] See the *Embedded network 1D–3D model (tissue perfusion)* example on the DuMuX website (`https://git.iws.uni-stuttgart.de/dumux-repositories/dumux/-/blob/master/examples/embedded_network_1d3d/README.md`) and the paper [Koch, 2022] for a detailed description of the model.

as the problem is CFD and conservation of mass is desired. In practice, the 3d domain is divided into small cubes of equal size, while the capillaries in the 1d one are divided into smaller segments. Moreover, a Two-Point Flux Approximation (TPFA) scheme is selected. This simple but robust scheme manages the flux of a quantity between two adjacent cells just relying on variables evaluated in their centres and on the distance between these centres. Clearly, the quantity in question in this case is oxygen. Concerning the communication between the two compartments, i.e. the embedding, the Cylinder Surface Method is used, as described in [Koch, 2022]. Briefly, it places the source term q_c in the finite volumes that intersect the capillaries walls, after computing it using an averaged value for P_T. Note that more details about this aspect can be found in the Appendix 8. Finally, the solution is found using a *chopped* Newton solver, that differs from a classical one because it restricts the domain of the solution at the start.
Refer again to the Appendix 8 for the numerical values employed for the model parameters.

Figure 2.4: DuMux logo. From `https://dumux.org/`

.

2.4 Dataset

2.4.1 MVN1

As mentioned in the introduction, this work is aimed at analysing the oxygen supply behaviour in the cerebral cortex of the mouse. In order to do so, a dataset describing a section of mouse brain microvasculature is employed in the simulations described in the previous chapters. The data is obtained using two-photon laser scanning microscopy. A classification of vessels into pial arteries, arterioles, capillaries, venules and pial veins was conducted. The criteria relied on vessel morphology, diameter and on the tracking of penetrating trees [Blinder et al., 2013]. The result is a microvascular network called MVN1 (MicroVascular Network 1, figure 2.5 on the right), which has the following characteristics:

- it can be embedded in a volume of $1\,mm^3$;

- it contains a total of 10 descending arterioles (DAs) and 30 ascending venules (AVs);
- it has around 20000 capillaries in total, that densely perfuse the volume;
- it shows an average capillary diameter of $4\,\mu m$, while the range of diameters dimension in all blood vessels spans from $2.5\,\mu m$ to $55\,\mu m$.

2.4.2 Simulations domain

While the blood flow simulation could be run on the whole network, the oxygen supply was too computationally expensive with the methods explained in 2.3.5. As a consequence, it was necessary to consider subsections of MVN1 (see figure 2.5 on the left). For the analyses reported hereafter, three of them were employed, such that each subsection:

- can be embedded in a volume of $0.064\,mm^3$;
- contains roughly 1200 capillaries.

This translates into around 10 thousand 1d mesh elements and 4 million finite cells per subsection in the DuMux simulation.

The whole somatosensory cortex of a mouse shows a vasculature that is very similar across

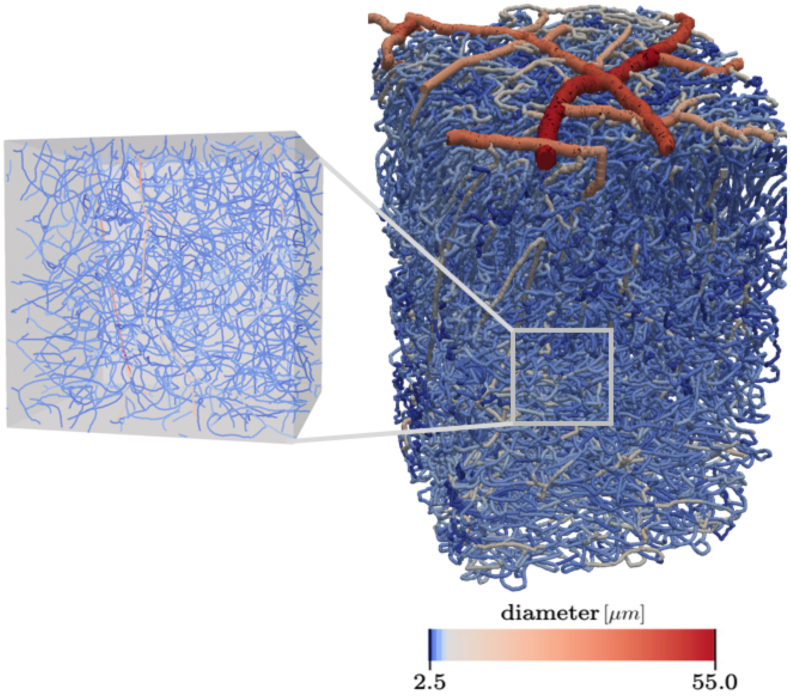

Figure 2.5: On the right, MVN1 representation by [Blinder et al., 2013]. On the left, example of subsection of MVN1 used in simulations.

all of its subregions, in line with a trend that is shared by all brain areas [Ji et al., 2021]. This means that an accurate simulation in small sections can already be insightful.

3 Topological vascular analysis

3.1 Introduction

The oxygen supply simulation presented previously is very computationally demanding. Indeed, the embedded model is complex for two main reasons: the nature of the equations it involves and the intricacy of the geometry where it is defined. Thus, a question arises: is it possible to draw conclusions related to tissue oxygenation from a vessel feature, without running oxygen simulations at all? The vessel topology, introduced in the second section of this chapter, is a suitable candidate for this. Vessel topology is a characteristic related to the *topology* of MVN1. In this context, *topology* is used in a wide sense. As a matter of fact, this word, that derives from the combination of the Greek words τόπος (tópos), meaning *place* and thus *geometry* in a mathematical setting, and λόγος (lógos), meaning *study*, is not interpreted solely as *study of the geometry*. It generically signifies *study of the structure*, where in this context *structure* refers to the foundation of the oxygen supply simulation problem. Therefore, it comprises the study of vessel orientation, a fundamental *structural* aspect of blood perfusion of brain tissue[1].

Other topological features are then presented and put in relation to vessel topology, allowing for a first exploration and interpretation of its relevance. In details:

- length, measured in m;
- tortuosity, indicating how *straight* a vessel is;
- AV factor, assessing how close a vessel is to descending arteries (DAs) or ascending venules (AVs);
- edge-betweenness centrality, measuring how *central* an edge is in the graph.

---

[1] Perhaps the word *histology*, that literally signifies *study of the bearing structure*, would be more adapt, but it is already widely used in biology with a different meaning.

3.2 Vessel topology

As mentioned above, the focus of this work is understanding if certain oxygenation aspects are correlated with vessel topology. This feature represents a way of distinguishing vessels depending on blood flow direction in their proximity (it thus requires running blood flow simulations). Indeed, this is a plausible primary factor influencing oxygenation around a vessel. Each vessel is classified into a topological configuration, or MSC type (it stands for MicroStrokes Configurations, according to the definition by [Schmid et al., 2021]), depending on the direction of blood flow in its neighbouring vessels. Therefore, it is possible to say that this classification is inherently local. Note that the term *vessel topology* is used when talking about this feature in general, while the expression *topological configuration* is employed when talking about the specific categories a vessel can belong to. A formal definition of vessel topology is given in the next section, followed by the methods implemented to classify vessels and by the frequency of the different topological configurations in the sections of the microvascular networks considered.

3.2.1 Definitions

Graphs and degree functions

Before defining topological configurations, it is necessary to mathematically represent the blood vessel network. Let $\mathcal{G} = (\mathcal{V}, \mathcal{E})$ be the undirected graph representing the section of the microvasculature of the brain analysed. Each blood vessel is represented by an edge $e = (u, v)$, where (u, v) is an unordered pair indicating the endpoints of the vessel, $e \in \mathcal{E}$ and $u, v \in \mathcal{V}$. The *directed* graph $\mathcal{G}_d = (\mathcal{V}, E)$ inherits $\mathcal{G}$ nodes, but each blood vessel is instead associated with a *directed* edge $e = (u, v) \in E$, where (u, v) is an ordered pair. The direction of the edge is based on the direction of the blood flow that passes through it.

The *undirected* degree function $\delta : \mathcal{V} \to \mathbb{N}_0$ is such that $\delta(v)$ expresses the degree of node $v \in \mathcal{V}$ according to the undirected graph $\mathcal{G}$. The degree of a node $v \in \mathcal{V}$ is defined as the number of edges linked to v. Instead, the functions $\delta^+ : \mathcal{V} \to \mathbb{N}_0$ and $\delta^- : \mathcal{V} \to \mathbb{N}_0$ are such that $\delta^+(v)$ and $\delta^-(v)$ express respectively the outdegree and the indegree of node $v \in \mathcal{V}$ according to the directed graph $\mathcal{G}_d$. The outdegree and indegree of a node $v \in \mathcal{V}$ are respectively defined as the number of directed edges that start from v and the number of directed edges that end at v.

Topological configurations

Each vessel in the graph is classified into a topological configuration $t \in T = \{0, 22, 21, 12, 11\}$. In order to do so, a function $\tau : E \rightarrow T$ is defined in the following way, $\forall\, e = (u, v) \in E$:

- $\tau(e) = 0$ if $\delta(u) \neq 3 \vee \delta(v) \neq 3$;
- $\tau(e) = 22$ if $\delta(u) = 3, \delta(v) = 3, \delta^-(u) = 2, \delta^+(v) = 2$;
- $\tau(e) = 21$ if $\delta(u) = 3, \delta(v) = 3, \delta^-(u) = 2, \delta^+(v) = 1$;
- $\tau(e) = 12$ if $\delta(u) = 3, \delta(v) = 3, \delta^-(u) = 1, \delta^+(v) = 2$;
- $\tau(e) = 11$ if $\delta(u) = 3, \delta(v) = 3, \delta^-(u) = 1, \delta^+(v) = 1$.

$\tau(e) = 0$ indicates a *null* configuration (e does not belong to any configuration). If there are exactly two edges, besides (u, v), incident to both u and v, then $\tau(e) \neq 0$. It is possible to visualise the four non-null topological configurations in figure 3.1. $\tau(e) = 22$ if u has two inflows and v has two outflows (see a). This topological configuration is consequently called *2-in-2-out*. According to the same logic, configurations *2-in-1-out* (see b), *1-in-2-out* (see c), *1-in-1-out* (see d) are detected, corresponding respectively to $\tau(e) = 21$, $\tau(e) = 12$ and $\tau(e) = 11$.

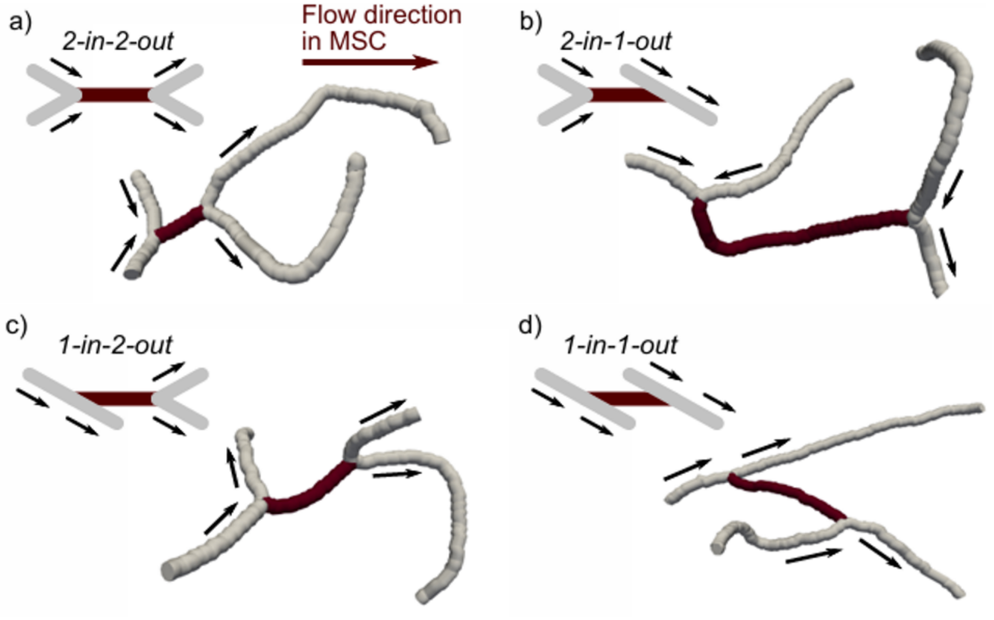

Figure 3.1: Topological configurations. The arrows in black represent the direction of blood flow. *Flow direction in MSC* stands for *Flow direction in the vessel belonging to the different topological configurations*. Image from [Schmid et al., 2021].

Note: edges incident to nodes $v \in \mathcal{V} : \delta(v) \neq 3$

As previously stated, when an edge $e = (u, v) \in \mathcal{E}$ is such that $\delta(u) \neq 3 \vee \delta(v) \neq 3$, its topological configuration is null. Indeed, nodes $u \in \mathcal{V}$ such that $\delta(u) = 1$ are associated with boundary inflow/outflow conditions, so that the classification proposed makes no sense for edges incident to them, and nodes $u \in \mathcal{V}$ such that $\delta(u) = 2$ are not at all present. Concerning nodes with a degree greater than three, only degree four nodes can be found in MVN1. The choice of not classifying edges incident to those nodes is in line with [Schmid et al., 2021], and it is motivated by their rare occurrence (below 0.1%).

3.2.2 Methods

It is necessary to carefully design an algorithm to classify the edges into topological configurations. First, the graphs $\mathcal{G}$ and $\mathcal{G}_d$ are built. Unlike what was presented in 3.2.1, each blood vessel is in practice represented by a sequence of edges, linking a sequence of points. This accounts for the fact that a vessel is not necessarily a straight line. The sequence of edges composing a vessel is derived from the dataset presented in section 2.4. These edges correspond to the 1d elements presented in section 2.3.5, implying that the mesh refinement for the 1d compartment Λ relies on experimental data. A blood vessel θ can thus be expressed as a sequence $\{(u_{i,\theta}, v_{i,\theta})\}_{1\leq i\leq n_\theta}$, where $u_{i+1} = v_i \quad \forall 1 \leq i < n_\theta$ (see figure 3.2). The set of all blood vessels is called Θ, while the set E is redefined to contain all the 1d elements. In this framework, nodes $v \in V$ such that $\delta(v) = 2$ (that would otherwise not exist) arise: they are the *interior* nodes of a blood vessel. More precisely, taken a generic blood vessel $\theta := \{(u_{i,\theta}, v_{i,\theta})\}_{1\leq i\leq n_\theta}$, they are the nodes u_i such that $1 < i \leq n_\theta$ and the nodes v_i such

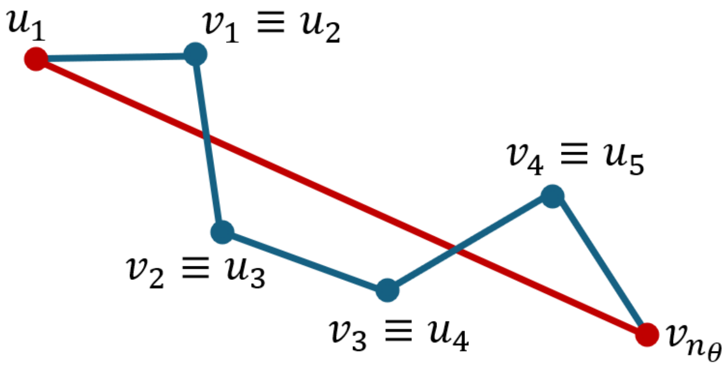

Figure 3.2: Difference in vessel representation between sections 3.2.1 and 3.2.2. In 3.2.1, a vessel is considered as a straight line between u_1 and v_{n_θ} (in red). From now on, a vessel consists of a sequence of edges (in blue).

.

that $1 \leq i < n_\theta$.

After creating the graphs, the label *bifurcation point* is assigned to each node $v \in \mathcal{V}$ such that $\delta(v) = 3$. The set of all bifurcation points will be called B. A bifurcation point $b \in B$ belongs to one of two different sets according to the following rules:

- $b \in B_{12}$ if $\delta^-(b) = 1 \land \delta^+(b) = 2$;
- $b \in B_{21}$ if $\delta^-(b) = 2 \land \delta^+(b) = 1$.

The set B_{12} thus collects *1-2 bifurcations*, i.e., nodes that have one inflow and two outflows, while the set B_{21} contains *2-1 bifurcations*, that is, nodes that have two inflows and one outflow. Successively, the algorithm iterates over B and, at every iteration, makes the following steps for $b \in B$:

1) it stores the information about whether b belongs to B_{12} or B_{21};
2) it iterates over all the possible vessels Θ_b in $\mathcal{G}_d$ that start from b. So, for each $\theta \in \Theta_b$:
    i) it continues along the vessel until reaching node f such that $\delta(f) \neq 2$;
    ii) it classifies $\theta = \{(b, v_{1,\theta}), (u_{2,\theta}, v_{2,\theta}), ..., (u_{n_\theta}, f)\}$ into one configuration.

The classification is conducted as follows:

- $f \notin B \implies \delta(f) \neq 3 \implies \tau(\theta) = 0$;
- $b \in B_{21} \land f \in B_{12} \implies \delta(b) = 3 \land \delta(f) = 3 \land \delta^-(b) = 2 \land \delta^+(f) = 2 \implies \tau(\theta) = 22$;
- $b \in B_{21} \land f \in B_{21} \implies \delta(b) = 3 \land \delta(f) = 3 \land \delta^-(b) = 2 \land \delta^+(f) = 1 \implies \tau(\theta) = 21$;
- $b \in B_{12} \land f \in B_{12} \implies \delta(b) = 3 \land \delta(f) = 3 \land \delta^-(b) = 1 \land \delta^+(f) = 2 \implies \tau(\theta) = 12$;
- $b \in B_{12} \land f \in B_{21} \implies \delta(b) = 3 \land \delta(f) = 3 \land \delta^-(b) = 1 \land \delta^+(f) = 1 \implies \tau(\theta) = 11$.

3.2.3 Frequency of topological configurations

Each vessel in the graph is classified into a topological configuration according to the methods described. The results concerning the frequencies of configurations are displayed in figure 3.3. They do not take into account the null configuration, so that the percentages are computed on the total of vessels classified into a non-null one. It is very immediate to notice that the 1-in-1-out configuration is by far the most common across the vessels in the network, with more than 40% of occurrences. On the contrary, the 2-in-2-out is the rarest, with less than 10% that belong to this category. Finally, 2-in-1-out and 1-in-2-out configurations are approximately on the same level, halfway between the other two, making up around 25% of the total vasculature. These results are in line with what was found in [Schmid et al., 2021] in the whole MVN1, as the data distribution is similar (see figure 3.3).

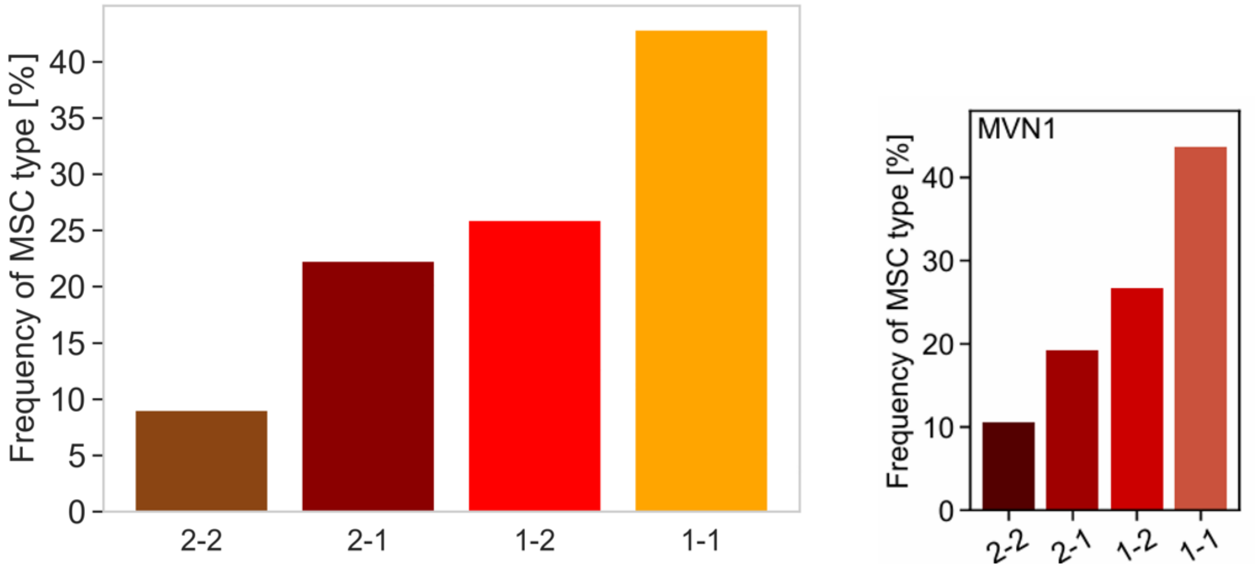

Figure 3.3: Comparison of results about topological configuration frequencies. On the left, the ones detected in the 3 extracted microvascular networks analysed. On the right, the ones retrieved in [Schmid et al., 2021] on the whole MVN1.

3.3 Other topological features

After classifying vessels into topological configurations, other topological features are analysed and put in relation to vessel topology. This allows for an initial understanding of the differences between configurations. The results are displayed and briefly commented for each section. Note they are analysed more rigorously in chapter 5.

3.3.1 Length

The first feature considered is the length of the vessels. It is surely important to account for this information, since it might be an important characteristic for understanding oxygen distribution. Thus, a length l is associated with each vessel $\theta = \{(u_{i,\theta}, v_{i,\theta})\}_{1 \leq i \leq n_\theta}$, according to the following definition:

$$l := \sum_{i=1}^{n_\theta} d_e(u_i, v_i) \tag{3.1}$$

where $d_e(a, b)$ indicates the Euclidean distance between point a and point b. It is important to notice that l differs from the Euclidean distance between the endpoints of θ, i.e.

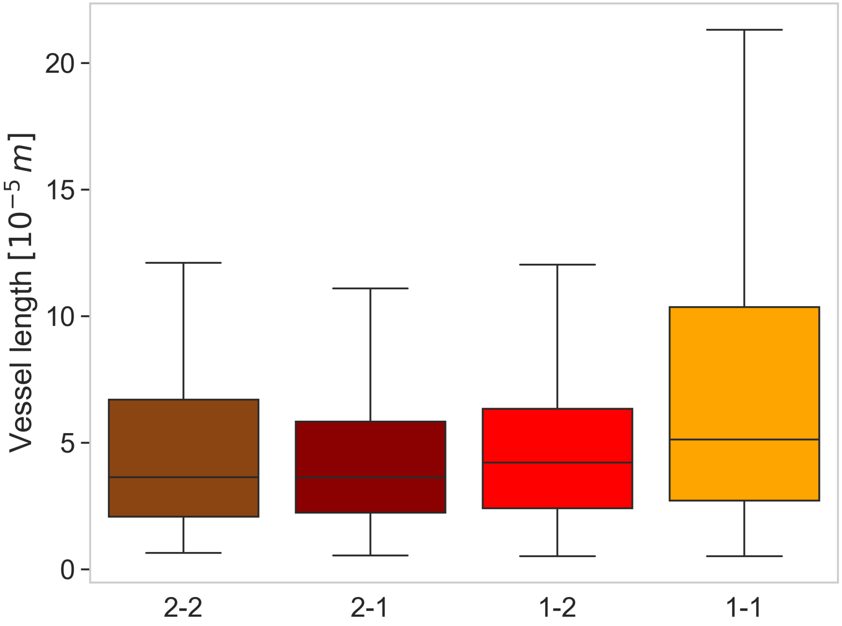

Figure 3.4: Vessel length distribution for each topological configuration, represented via a box plot highlighting the median.

.

$d_e(u_1, v_{n_\theta})$. The relation between l and $d_e(u_1, v_{n_\theta})$ is exactly what is encapsulated by the definition of tortuosity, discussed in the next section. The distribution of lengths per topological configuration is reported in figure 3.4. The medians of the 2-in-2-out, 2-in-1-out, 1-in-2-out configurations are approximately the same, below 50 μm, while the 1-in-1-out configuration shows a median value that is slightly above 50 μm, along with a confidence interval that is noticeably more widely spread. This behaviour suggests that the 1-in-1-out configuration is associated with the longest vessels.

3.3.2 Tortuosity

As anticipated previously in 3.3.1, the tortuosity ψ of a vessel $\theta = \{(u_{i,\theta}, v_{i,\theta})\}_{1 \leq i \leq n_\theta}$ is a feature that involves the relation between its length l and the Euclidean distance between its endpoints $d_e(u_1, v_{n_\theta})$. It is defined as the ratio between the former and the latter (see figure 3.5):

$$\psi(\theta) := \frac{l}{d_e(u_1, v_{n_\theta})} \tag{3.2}$$

This characteristic is aimed at synthesising in a simple manner *how much* a vessel curls up in space, by measuring how much it differs from a straight line between its endpoints. Even if there are other ways of doing this [Han, 2012], the definition in 3.2 is a very straightforward

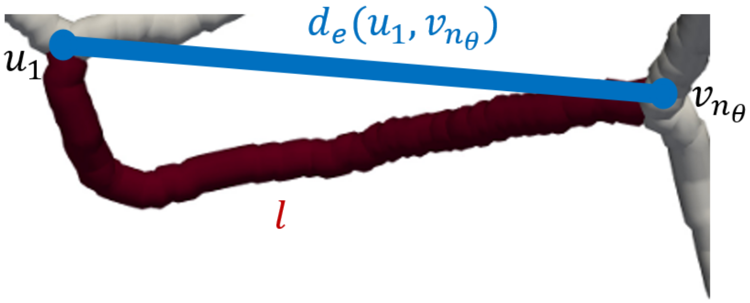

Figure 3.5: Visual representation of the two terms l and $d_e(u_1, v_{n_\theta})$ in the tortuosity definition 3.2.

.

one. Note that 3.2 strongly depends on the number of edges composing θ. The use of this formula is justified by the fact that the definition of θ relies on experimental data (as mentioned in section 3.2.2). In figure 3.6 the length distributions for each configuration are reported. The picture is similar to section 3.3.1. Indeed, the median of tortuosity for the 1-in-1-out configuration seems to be significantly greater than the median of the others, that are approximately on the same level. Moreover, the confidence interval for the 1-in-1-out configuration is noticeably more widely spread. The data displayed points to the idea that the vessels with a 1-in-1-out configuration are usually the most tortuous one, while the other configurations have similar tortuosity distributions.

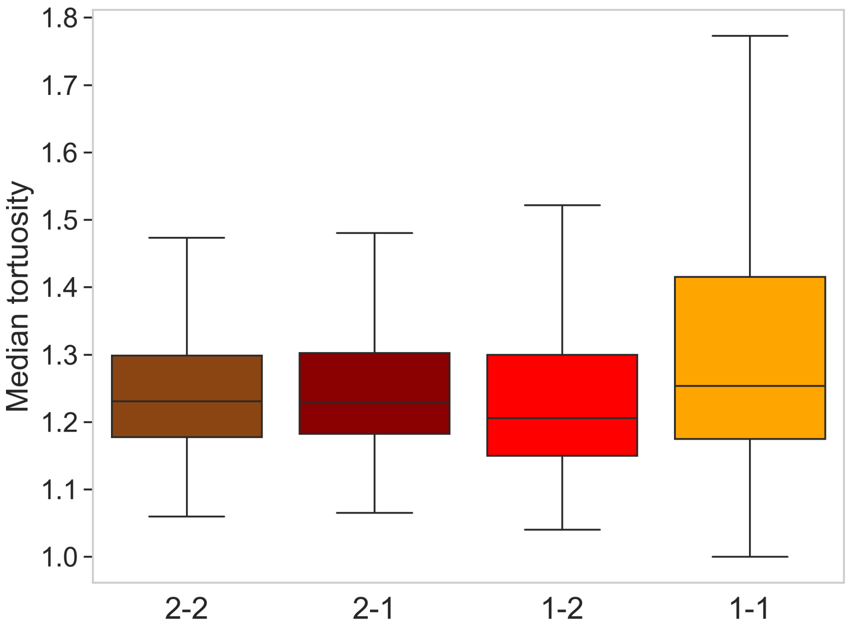

Figure 3.6: Analysis of tortuosity for each topological configuration, via a box plot highlighting the median in black.

3.3.3 AV factor

After having discussed vessel topology, length and tortuosity, the AV factor feature is presented. As introduced in section 3.1, it is a measure that allows to assess how close a vessel is to descending arteries (DAs) or to ascending venules (AVs). The definition here given is taken from [Schmid et al., 2021]. Let $\mathcal{V}_{DA} \subset \mathcal{V}$ be the set of nodes that belong to the descending arterioles and $\mathcal{V}_{AV} \subset \mathcal{V}$ be the set of nodes that belong to the ascending venules. Let $P(A, B)$ return the set of all paths between all the possible combinations of the nodes in set A and in set B. Moreover, let $N_\theta := |P(\mathcal{V}_{DA}, \{u_{1,\theta}\})|$. $\alpha_{DA} : \Theta \to \cup_{\theta\in\Theta}\mathbb{R}^{N_\theta}$ is defined as the function that associates to each vessel $\theta = \{(u_{i,\theta}, v_{i,\theta})\}_{1\leq i\leq n_\theta} \in \Theta$ the lengths of all paths in $P(\mathcal{V}_{DA}, \{u_{1,\theta}\})$. Analogously, let $M_\theta := |P(\{v_{n_\theta}\}, \mathcal{V}_{AV})|$. $\alpha_{AV} : \Theta \to \cup_{\theta\in\Theta}\mathbb{R}^{M_\theta}$ returns for each vessel $\theta = \{(u_{i,\theta}, v_{i,\theta})\}_{1\leq i\leq n_\theta} \in \Theta$ the lengths of all paths in $P(\{v_{n_\theta}\}, \mathcal{V}_{AV})$. Taken a vessel $\theta = \{(u_i, v_i)\}_{1\leq i\leq n_\theta} \in \Theta$, its AV factor, called AV_θ, is:

$$AV_\theta := \frac{\mu(\alpha_{DA}(\theta))}{\mu(\alpha_{DA}(\theta)) + \mu(\alpha_{AV}(\theta))} \in [0, 1] \tag{3.3}$$

where $\mu : \cup_{n\in\mathbb{N}}\mathbb{R}^n \to \mathbb{R}$ is the median function. In practice, the AV factor is the ratio between the median distance of a vessel from the DAs and the sum of the median distances of a vessel from the AVs and the DAs (see figure 3.7 for a schematic representation). The closer to 0 the AV factor value, the closer the vessel is to the descending arterioles, as in this instance $\mu(\alpha_{DA}(\theta)) << \mu(\alpha_{AV}(\theta))$. Instead, the closer to 1 its value, the closer the vessel is to the ascending venules, as in this case $\mu(\alpha_{AV}(\theta)) << \mu(\alpha_{DA}(\theta))$. Since the computation of the AV factor is non-trivial, the following section is devoted to describing in details how it was calculated for each vessel in MVN1.

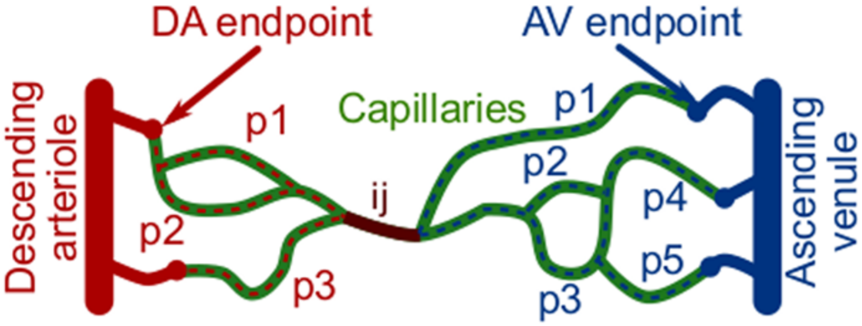

Figure 3.7: Schematic representation of the meaning of the AV factor. Focusing on vessel (i, j), $P(\mathcal{V}_{DA}, \{i\}) = \{p_1, p_2, p_3\}$ and $P(\{j\}, \mathcal{V}_{AV}) = \{p_1, p_2, p_3, p_4, p_5\}$. The AV factor is the ratio between the median length of the paths in $P(\mathcal{V}_{DA}, \{i\})$ and the sum of the median lengths of the paths in $P(\mathcal{V}_{DA}, \{i\})$ and $P(\{j\}, \mathcal{V}_{AV})$. Image from [Schmid et al., 2021].

Classification of nodes

The first thing needed for AV factor computation is the construction of sets $\mathcal{V}_{DA}$ and $\mathcal{V}_{AV}$. In section 2.4, where the dataset is described, it is said that a classification of vessels $\theta \in \Theta$ into pial arteries, arterioles, capillaries, venules and pial veins was conducted. Vessels classified into pial arteries or arterioles are considered belonging to the same class, that is *DAs*. In the same way, those classified into pial veins or venules are assigned the common label *AVs*. The vessels that do not belong to any class are denoted by the letter U. However, there is still the need of classifying *the nodes*. Note that the analysis that follows revolves around the graph $\mathcal{G}_d = (\mathcal{V}, E)$, described in subsection 3.2.2. It is reminded that each vessel $\theta \in \Theta$ can be written as $\{(u_{i,\theta}, v_{i,\theta})\}_{1 \leq i \leq n_\theta}$, where $(u_{i,\theta}, v_{i,\theta}) \in E$, $1 \leq i \leq n_\theta$. The classification of each node $v \in \mathcal{V}$, with $\delta(v) \neq 2$ (that is not an internal node of a vessel), is done according to the steps below:

(i) consider the edges $e = (u, w) \in E$ such that $w = v$. Let E_v^- be the set of these edges;

(ii) let i_{DA}^-, i_{AV}^-, i_C^- and i_U^- be the number of edges in E_v^- that are respectively descending arterioles, ascending venules, capillaries or of unknown nature.

  - if $|\max(i_{DA}^-, i_{AV}^-, i_C^-, i_U^-)| = 1$, v is classified according to the following rules:
    - $\max(i_{DA}^-, i_{AV}^-, i_C^-, i_U^-) = i_{DA}^- \implies v \in \mathcal{V}_{DA}$;
    - $\max(i_{DA}^-, i_{AV}^-, i_C^-, i_U^-) = i_{AV}^- \implies v \in \mathcal{V}_{AV}$;
    - $\max(i_{DA}^-, i_{AV}^-, i_C^-, i_U^-) = i_C^- \vee \max(i_{DA}^-, i_{AV}^-, i_C^-, i_U^-) = i_U^-$ $\implies v \in \mathcal{V} \setminus (\mathcal{V}_{AV} \cup \mathcal{V}_{DA})$.
  - otherwise, go to step (iii).

(iii) consider the edges $e = (u, w) \in E$ such that $u = v$. Let E_v^+ be the set of these edges;

(iv) let i_{DA}^+, i_{AV}^+, i_C^+ and i_U^+ be the number of edges in E_v^+ that are respectively descending arterioles, ascending venules, capillaries or of unknown nature. Define $i_{DA} := i_{DA}^- + i_{DA}^+$, $i_{AV} := i_{AV}^- + i_{AV}^+$, $i_C := i_C^- + i_C^+$ and $i_U := i_U^- + i_U^+$;

  - if $|\max(i_{DA}, i_{AV}, i_C, i_U)| = 1$, v is classified according to the following rules:
    - $\max(i_{DA}, i_{AV}, i_C, i_U) = i_{DA} \implies v \in \mathcal{V}_{DA}$;
    - $\max(i_{DA}, i_{AV}, i_C, i_U) = i_{AV} \implies v \in \mathcal{V}_{AV}$;
    - $\max(i_{DA}, i_{AV}, i_C, i_U) = i_C \vee \max(i_{DA}, i_{AV}, i_C, i_U) = i_U$ $\implies v \in \mathcal{V} \setminus (\mathcal{V}_{AV} \cup \mathcal{V}_{DA})$.

  - otherwise, go to step (v).

(v) go through a series of *if-else* conditions:

  - if $\max(i_{DA}, i_{AV}, i_C, i_U) = 0$, v is an isolated node and it belongs to $\mathcal{V} \setminus (\mathcal{V}_{AV} \cup \mathcal{V}_{DA})$;
  - else if $i_{DA} = \max(i_{DA}, i_{AV}, i_C, i_U) \implies v \in \mathcal{V}_{DA}$;
  - else if $i_{AV} = \max(i_{DA}, i_{AV}, i_C, i_U) \implies v \in \mathcal{V}_{AV}$;
  - else if $i_C = \max(i_{DA}, i_{AV}, i_C, i_U) \implies v \in \mathcal{V} \setminus (\mathcal{V}_{AV} \cup \mathcal{V}_{DA})$.

Note that no more *else if* conditions are needed in point (v) as one value among i_{DA}, i_{AV} and i_C has to be equal to $\max(i_{DA}, i_{AV}, i_C, i_U)$, since $|\max(i_{DA}, i_{AV}, i_C, i_U)| > 1$. Once the vessel points have been classified, it is possible to proceed with the description of the algorithm for the actual AV factor computation.

Algorithm for AV factor computation

It is not possible to adopt a *brute-force* method when it comes to computing the AV factor. What is meant by *brute-force* method is computing iteratively, for each vessel $\theta = \{(u_{i,\theta}, v_{i,\theta})\}_{1 \leq i \leq n_\theta} \in \Theta$, $\alpha_{DA}(\theta)$ and $\alpha_{AV}(\theta)$, that requires finding $P(\mathcal{V}_{DA}, \{u_{1,\theta}\})$ and $P(\{v_{n_\theta,\theta}\}, \mathcal{V}_{AV})$ at each iteration. As this is too computationally complex, it is mandatory to adopt a more refined approach. A dynamic programming method was chosen, as suggested by the structure of the problem itself. Indeed, it is very common that $P(\mathcal{V}_{DA}, \{u_{1,\theta_1}\}) \cap P(\mathcal{V}_{DA}, \{u_{1,\theta_2}\}) \neq \emptyset$ or $P(\{u_{1,\theta_1}\}, \mathcal{V}_{AV}) \cap P(\{u_{1,\theta_2}\}, \mathcal{V}_{AV}) \neq \emptyset$ for $\theta_1 \neq \theta_2 \in \Theta$. This points to the idea of storing $P(\{v_1\}, \{v_2\})$, $\forall\, v_1, v_2 \in \mathcal{V}$ in a dynamically built memory structure, so that, for each $\theta \in \Theta$, $P(\mathcal{V}_{DA}, \{u_{1,\theta}\})$ and $P(\{v_{n_\theta,\theta}\}, \mathcal{V}_{AV})$ are quickly built. In practice, only the lengths of the paths, that are called $L[P(\{v_{n_\theta,\theta}\}, \mathcal{V}_{AV})]$ hereafter, are saved, since it requires less memory. Before doing that, a *topological sorting* $\mathcal{T}(\mathcal{V})$ of the nodes in the graph $\mathcal{G}_d$ is conducted. A topological sorting is a linear ordering of the nodes such that, if any directed edge $e = (u, v) \in E$ is considered, u comes before v in the ordering[2]. This is useful because it can be easily shown that, taken two nodes v_1, v_2 in the graph such that v_1 comes before v_2 in the ordering, there are no paths from v_2 to v_1. Consequently, it is possible to avoid computing $L[P(\{v_2\}, \{v_1\})]$, that can immediately be set equal to $\emptyset$. After this explanation, the algorithms for finding $L[P(\{v_1\}, \{v_2\})]$, $\forall\, v_1, v_2 \in \mathcal{V}$ are presented. First, the main loop (Algorithm 1). Then, the dynamic programming function (Algorithm 2).

The symbol $\oplus$ operator represents a scalar-vector addition, where each entry of the vector is added to the scalar. Also note that the function in Algorithm 2 is *cached*: its outputs are

---

[2] A topological sorting can only be done in a directed acyclic graph (DAG), as $\mathcal{G}_d$ is.

Algorithm 1 Main loop

```
Create an empty dictionary $D$
for $u \in \mathcal{T}(\mathcal{V})$ do
    for $v \in \mathcal{T}(\mathcal{V})$ such that $v$ is after $u$ in $\mathcal{T}(\mathcal{V})$ do
        $L[P(\{u\},\{v\})] = \mathrm{dyn}(\{u\},\{v\})$
        $D(u,v) = L[P(\{u\},\{v\})]$
    end for
end for
```

Algorithm 2 $\mathrm{dyn}(\{u\},\{v\})$

```
if $u = v$ then:
    return $\{0\}$
else
    $L[P(\{u\},\{v\})] = \emptyset$
    for $w \in \mathcal{V}$ such that $(u,w) \in E$ do
        $L[P(\{w\},\{v\})] = \mathrm{dyn}(\{w\},\{v\})$
        $l = d_e(u,w)$
        $L[P(\{u\},\{v\})] = L[P(\{u\},\{v\})] \cup (L[P(\{w\},\{v\})] \oplus l)$
    end for
    return $L[P(\{u\},\{v\})]$
end if
```

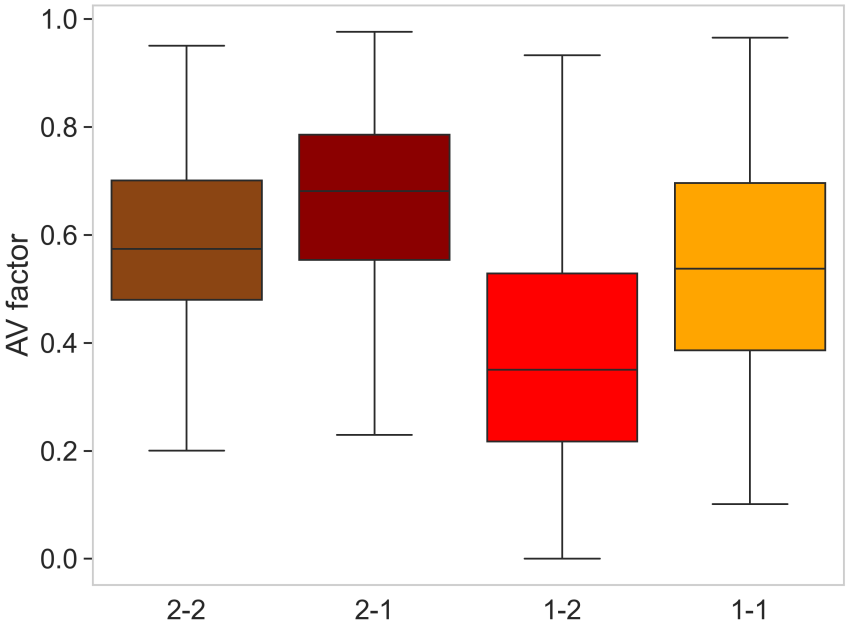

Figure 3.8: AV factor distribution for each topological configuration, represented via a box plot highlighting the median.

.

saved in a high-speed memory location (cache). This means that it is not necessary to recompute the output values if the same input is given. This is how $L[P(\{v_1\},\{v_2\})],\ \forall\, v_1, v_2 \in \mathcal{V}$ is stored. After running Algorithm 1, the computation of the AV factor for each vessel $e \in E$ becomes straightforward. All the information needed is accessible rapidly through a dictionary.

AV factor distributions

The results, displayed in figure 3.8, consider only the three microvascular domains described in 2.4. They suggest that the 2-in-1-out vessels are usually closer to AVs, while the 1-in-2-out ones are more towards the DAs. Instead, the other vessels, both in the 1-in-1-out and in the 2-in-2-out configurations, are evenly distributed around an AV factor of 0.5, pointing to an even distribution in the network. After completing the study of the AV factor, it is time to reason about the centrality of a vessel in the graph.

3.3.4 Edge-betweenness centrality

So far, only geometrical properties have been investigated. Now, a structural property is analysed, concerning the *centrality* of vessels. The concept of centrality in a graph concerns the assessment of the importance of a node or an edge through a numerical value, so that distinct nodes and edges can be compared based on the values assigned [van Steen, 2010]. Different centrality measures can be used depending on the notion of importance that is needed. As the main interest of this work is the impact of *vessels* on tissue oxygenation, the focus in this section is on edges. The choice of edge-betweenness centrality is motivated by its effectiveness in pointing out the edges that are more important for the behaviour of networks in terms of paths. The edge-betweenness centrality $\xi(e)$ of an edge $e \in E$, is defined as:

$$\xi(e) := \sum_{u,v \in \mathcal{V}} \frac{\sigma(u,v|e)}{\sigma(u,v)} \tag{3.4}$$

where $\sigma(u,v)$ is the number of shortest paths between nodes u and v, while $\sigma(u,v|e)$ represents the number of shortest paths between u and v that go through e. In figure 3.9, an example of a central edge in an undirected graph according to 3.4 is reported. The definition 3.4 can be found in [Ulrik, 2008]. Instead, the edge betweennes centrality $\xi(\theta)$ of a vessel $\theta = \{(u_{i,\theta}, v_{i,\theta})\}_{1\le i\le n_\theta} \in \Theta$ is the average of the centrality of the edges that compose it:

$$\xi(\theta) = \frac{1}{n_\theta} \sum_{i=1}^{n_\theta} \xi(u_{i,\theta}, v_{i,\theta}) \tag{3.5}$$

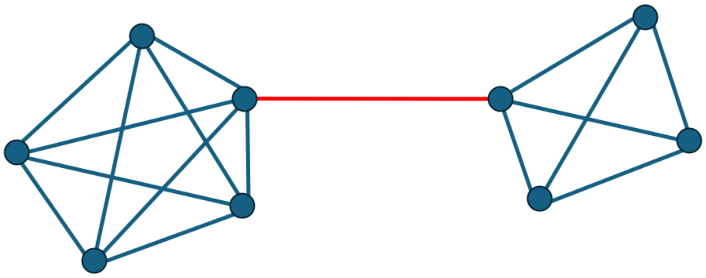

Figure 3.9: Example of an edge with high centrality, coloured with red, in an undirected graph.

.

Note that in the context of the microvasculature of the brain, blood flow does not necessarily flow from one point to the other through shortest paths, so edge-betweenness centrality might not be the optimal centrality measure for assessing the importance of a vessel relying on blood flow distribution. Nevertheless, it was computed on the domain sections of MVN1 described in section 2.4, relying only on the edges in these sections, using an algorithm developed in [Ulrik, 2001]. The results are shown in figure 3.10. They give the idea of a clear ranking in centrality: 2-in-2-out vessels look like the most central ones, followed by 2-in-1-out and 1-in-2-out ones, on the same level, while the 1-in-1-out ones seem the least central.

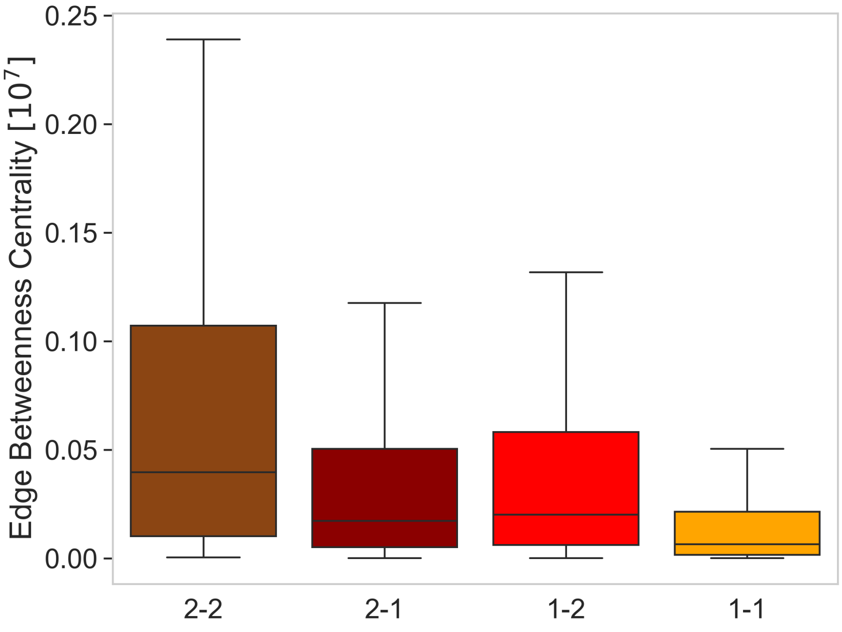

Figure 3.10: Edge-betweenness centrality distribution for each topological configuration, represented via a box plot highlighting the median.

.

4 Oxygen vascular analysis

4.1 Introduction

After having introduced vessel topology, along with other features, the goal is to assess if different topological configurations contribute differently to tissue oxygenation. In order to do so, it is necessary to organize the data derived from the oxygen simulation presented in section 2.3.5. Indeed, oxygen features have to be assigned to capillaries, arterioles and venules in order to understand their role in the oxygenation of brain tissue subsections. The features analysed for each vessel are:

- the oxygen flux, describing the flux of oxygen along the vessel (within blood);
- the transmembrane flux, indicating the flux of oxygen that leaves the vessel and enters tissue;
- the oxygen density, assessing the average concentration of oxygen around the vessel;
- the volume oxygenated, measuring the volume that is oxygenated by the vessel. In other words, it points out the volume reached by its transmembrane flux.

While the first and the second are directly derived from the methods described in chapter 2, the oxygen density and the volume oxygenated still need to be defined. Four different methods are proposed and compared for evaluating the oxygen density, whereas two are investigated for measuring the volume oxygenated.
Note that, throughout this chapter, the methods described are applied to each one of the three subsections of MVN1 described in 2.4.2. The results obtained are then combined, displayed and briefly commented, as was done in chapter 3. More rigorous statistical analysis is available in chapter 5.

4.2 Oxygen flux

The first oxygen feature analysed is the oxygen flux. This property describes how much oxygen leaves a vessel to reach other blood vessels in the microvasculature. Therefore, even if the oxygen flux is not directly related to tissue oxygenation, it gives valuable information about how crucial an arteriole, a capillary or a venule is in the oxygen distribution in the microvasculature. For example, if a vessel is occluded because of a microstroke [Schmid et al., 2021], all the oxygen flowing through it needs to be redirected via different paths.

4.2.1 Definition

A mathematical description of the oxygen flux along a vessel is now given. In section 2.3.3, the variable $\mathcal{F}_l$, with $l \in \{rbc, pl, S\}$ has been introduced, representing the oxygen flux within compartment l. The *pointwise* oxygen flux $\mathcal{F}_{tot}(\lambda)$, $\lambda \in \Lambda$ is defined as[1]:

$$\mathcal{F}_{tot}(\lambda) := \sum_{l \in \{rbc, pl, S\}} \mathcal{F}_l(\lambda) \tag{4.1}$$

Recalling the definitions presented in 3.2.1, the goal is now to associate the oxygen flux with each vessel $\theta = \{(u_{i,\theta}, v_{i,\theta})\}_{1 \leq i \leq n_\theta}$, where $(u_{i,\theta}, v_{i,\theta}) \in E,\ \theta \in \Theta, 1 \leq i \leq n_\theta$. The DuMux simulation returns data about the oxygen flux along each 1d element, i.e. each edge $e = (u_{i,\theta}, v_{i,\theta}) \in E$, for $\theta \in \Theta$ and for i such that $1 \leq i \leq n_\theta$. To be precise, $\mathcal{F}_{tot}(\lambda_{i,\theta})$ is known for each $\theta \in \Theta$, $1 \leq i \leq n_\theta$, where $\lambda_{i,\theta} \in \Lambda$ describes the centre of the 1d element according to the 1d parametrization. This means that the vessel θ is represented by a collection of ordered points $\lambda_{i,\theta}$, $1 \leq i \leq n_\theta$, such that the oxygen flux from point $\lambda_{i,\theta}$ to the following one $\lambda_{i+1,\theta}$ (or out of the vessel if $i = n_\theta$) is given by $\mathcal{F}_{tot}(\lambda_{i,\theta})$. To be coherent with the definition at the start of this section, the oxygen flux $\mathcal{F}_{tot}(\theta)$ along a vessel $\theta \in \Theta$ is defined in the following way:

$$\mathcal{F}_{tot}(\theta) := \mathcal{F}_{tot}(\lambda_{n_\theta,\theta}) \tag{4.2}$$

This is the oxygen flux leaving the vessel to reach other vessels in the microvasculature. As a matter of fact, part of the oxygen flux $\mathcal{F}_{tot}(\lambda_{i,\theta})$, $1 \leq i < n_\theta$ goes out into brain tissue[2], according to the following equation (checked numerically in DuMux), representing mass conservation:

$$\mathcal{F}_{tot}(\lambda_{i,\theta}) = -\hat{q}_c(\lambda_{i+1,\theta}) + \mathcal{F}_{tot}(\lambda_{i+1,\theta}) \tag{4.3}$$

---

[1] The reader is reminded that Λ is the vascular domain as described in 2.3.1.

[2] In some rare cases, there is an oxygen flux from brain tissue to capillaries. The construction made holds anyway.

where $\hat{q}_c(\lambda_{i+1,\theta})$ is the transmembrane flux out of the 1d element centered in $\lambda_{i+1,\theta}$, representing the integral of the transmembrane flux density over this 1d element. $\hat{q}_c(\lambda_{i+1,\theta})$ is known at the center of each 1d element and, consistently with the transmembrane flux density, takes negative values when exiting capillaries (see figure 4.1).

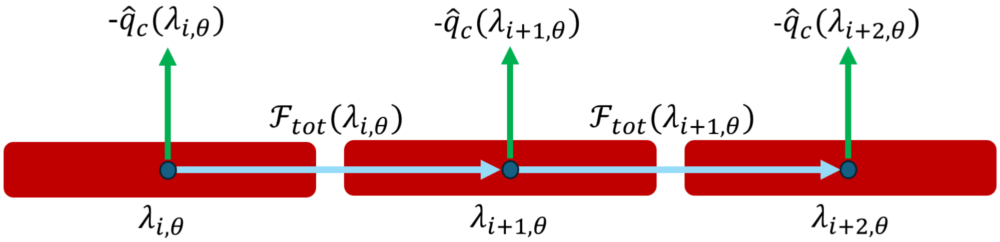

Figure 4.1: Visual representation of equation 4.3. The vectors represent the direction of the fluxes whose magnitude is expressed by the variables $-\hat{q}_C(\cdot)$ and $\mathcal{F}_{tot}(\cdot)$.

4.2.2 Results

After defining the oxygen flux variable, its behaviour across different topological configurations is observed (see figure 4.2). It is interesting to notice that the 1-in-1-out configuration has the lowest median and shows the lowest range of values. This suggests that this configuration is the least relevant in terms of oxygen distribution in the whole network. On the contrary, the 1-in-2-out one has the highest median among all, together with the highest

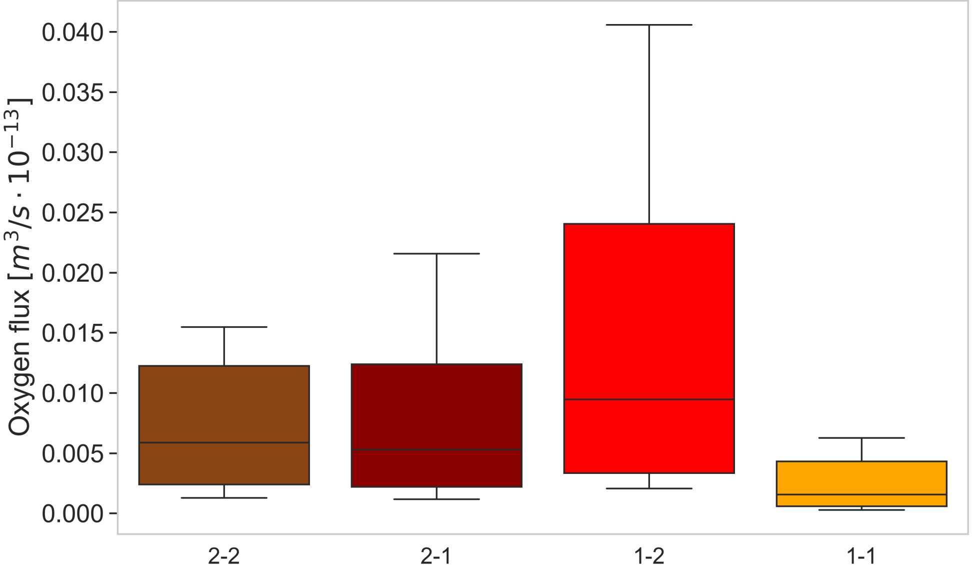

Figure 4.2: Oxygen flux distribution for each topological configuration, represented by a box plot showing whiskers at the 15th and 85th percentiles, highlighting the median.

range of values. This is in line with the fact that the vessels belonging to this configuration tend to be closer to arterioles (see AV factor behaviour, figure 3.8). Indeed, arterioles contain a higher concentration of oxygen, as they are the blood vessels responsible for carrying oxygenated blood into the microvasculature (see section 1.2). Finally, the oxygen flux distributions of the 2-in-2-out and 1-in-2-out configurations are similar, lying in a range between those of the other two configurations.

4.2.3 Correlation with blood flow

An important question that arises when considering oxygen flux is whether it is correlated with blood flow. If this were true, oxygen distribution in the network could be directly inferred by blood behaviour. Thus, a Pearson correlation test from the scipy.stats library in Python was conducted, assessing that there is a significant (p-value $< 10^{-6}$) linear correlation between blood flow and oxygen flux, with a correlation coefficient of approximately 0.967. This is further confirmed by the plot in figure 4.3, showing similar behaviour to the one in figure 4.2. Thus, blood flow and oxygen flux can be used interchangeably.

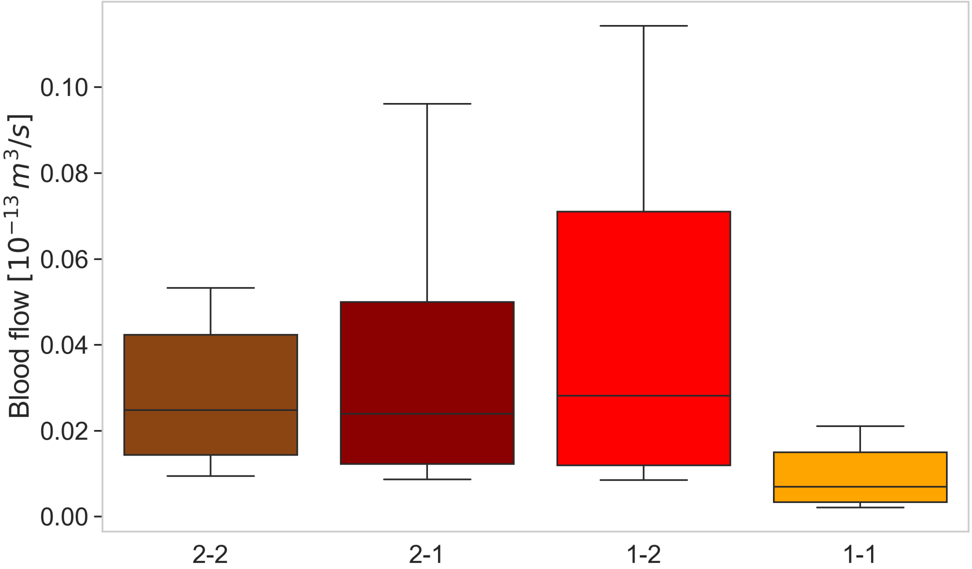

Figure 4.3: Blood flow distribution for each topological configuration, represented by a box plot defined as in 4.2.

4.3 Transmembrane flux

4.3.1 Definition

Closely related to the oxygen flux presented in the previous section is the transmembrane flux. As explained in section 4.2.1, the DuMux simulation returns the transmembrane flux density for each 1d element $\hat{q}_c(\lambda_{i,\theta})$, where $\lambda_{i,\theta} \in \Lambda$, $\theta \in \Theta$ and $1 \leq i \leq n_\theta$. The transmembrane flux $\hat{q}_c(\theta)$ associated with each vessel $\theta = \{(u_{i,\theta}, v_{i,\theta})\}_{1 \leq i \leq n_\theta} \in \Theta$ is defined as:

$$\hat{q}_c(\theta) = \sum_{1 \leq i \leq n_\theta} \hat{q}_c(\lambda_{i,\theta}) \tag{4.4}$$

Thus, $-\hat{q}_c(\theta)$ points out the total transmembrane flux from θ into brain tissue. The following equation must hold:

$$-\hat{q}_c(\theta) = \mathcal{F}^{-}_{tot}(\theta) - \mathcal{F}_{tot}(\theta) \tag{4.5}$$

where $\mathcal{F}_{tot}(\theta)$ is the oxygen flux out of the vessel (as defined in 4.2.1) and $\mathcal{F}^{-}_{tot}(\theta)$ is the oxygen flux into the first 1d element of θ. To show this, two equations (that have been checked numerically in DuMux) are employed:

1) mass conservation for each 1d element of a vessel θ, $\forall\, \theta \in \Theta$ (equation 4.3 from section 4.2.1);
2) mass conservation at bifurcations, so between 1d elements belonging to different vessels.

Mass conservation at bifurcations can be written as:

$$\mathcal{F}^{-}_{tot}(\theta) = \mathcal{F}_{tot}(\lambda_{1,\theta}) - \hat{q}_c(\lambda_{1,\theta}) \quad \forall \theta \in \Theta \tag{4.6}$$

ensuring that the sum of the oxygen fluxes coming into θ is equal to the sum of the oxygen flux and the transmembrane flux out of the first element of θ. An example of 4.6 is now given (see figure 4.4 for a visual representation). If $\theta_1 = \{(u_{i,\theta_1}, v_{i,\theta_1})\}_{1 \leq i \leq n_{\theta_1}}, \theta_2 = \{(u_{i,\theta_2}, v_{i,\theta_2})\}_{1 \leq i \leq n_{\theta_2}}, \theta_3 = \{(u_{i,\theta_3}, v_{i,\theta_3})\}_{1 \leq i \leq n_{\theta_3}}$ are three vessels such that $v_{n_{\theta_1},\theta_1} = v_{n_{\theta_2},\theta_2} = u_{1,\theta_3}$, the following equation holds:

$$\mathcal{F}^{-}_{tot}(\theta_3) = \mathcal{F}_{tot}(\theta_1) + \mathcal{F}_{tot}(\theta_2) = \mathcal{F}_{tot}(\lambda_{1,\theta_3}) - \hat{q}_c(\lambda_{1,\theta_3}). \tag{4.7}$$

Combining equations 4.3 and 4.6, it is possible to demonstrate the validity of equation 4.5.

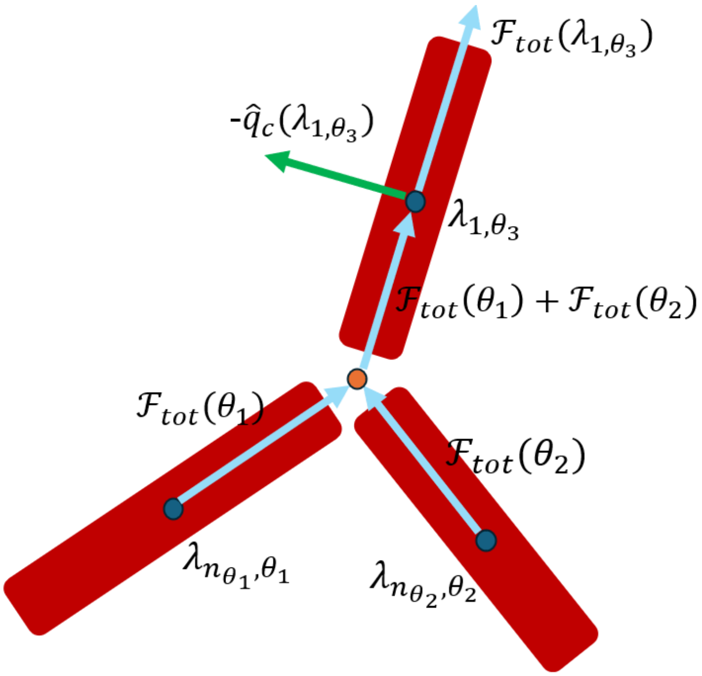

Figure 4.4: Visual representation of equation 4.7. The node $v_{n_{\theta_1},\theta_1} = v_{n_{\theta_2},\theta_2} = u_{1,\theta_3} \in B_{21}$ (see section 3.2.2 for a formal definition of B_{21}) is indicated in orange. It is an example of a bifurcation nodes with two inflows and one outflow.

Starting from 4.3:

$$\mathcal{F}_{tot}(\lambda_{i,\theta}) = -\hat{q}_c(\lambda_{i+1,\theta}) + \mathcal{F}_{tot}(\lambda_{i+1,\theta}),\ 1 \leq i < n_\theta \implies \tag{4.8}$$

$$\sum_{1\leq i<n_\theta} \mathcal{F}_{tot}(\lambda_{i,\theta}) = \sum_{1\leq i<n_\theta} [-\hat{q}_c(\lambda_{i+1,\theta}) + \mathcal{F}_{tot}(\lambda_{i+1,\theta})] \implies \tag{4.9}$$

$$\sum_{1\leq i<n_\theta} [\mathcal{F}_{tot}(\lambda_{i,\theta}) - \mathcal{F}_{tot}(\lambda_{i+1,\theta})] = \sum_{1\leq i<n_\theta} [-\hat{q}_c(\lambda_{i+1,\theta})] \implies \tag{4.10}$$

$$\sum_{1\leq i<n_\theta} [\mathcal{F}_{tot}(\lambda_{i,\theta}) - \mathcal{F}_{tot}(\lambda_{i+1,\theta})] - \hat{q}_c(\lambda_{1,\theta}) = \sum_{1\leq i<n_\theta} [-\hat{q}_c(\lambda_{i+1,\theta})] - \hat{q}_c(\lambda_{1,\theta}) \implies \tag{4.11}$$

$$[\mathcal{F}_{tot}(\lambda_{1,\theta}) - \hat{q}_c(\lambda_{1,\theta})] - \mathcal{F}_{tot}(\lambda_{n_\theta,\theta}) = -\hat{q}_c(\theta) \underset{4.6}{\implies} \mathcal{F}^{-}_{tot}(\theta) - \mathcal{F}_{tot}(\theta) = -\hat{q}_c(\theta) \tag{4.12}$$

4.3.2 Results

The transmembrane flux $\hat{q}_c(\theta)$ is then computed for each vessel and results are displayed in figure 4.5. The picture observed is similar to the oxygen flux one, except for the 1-in-1-out configuration behaviour. Note that the results are commented considering the absolute value

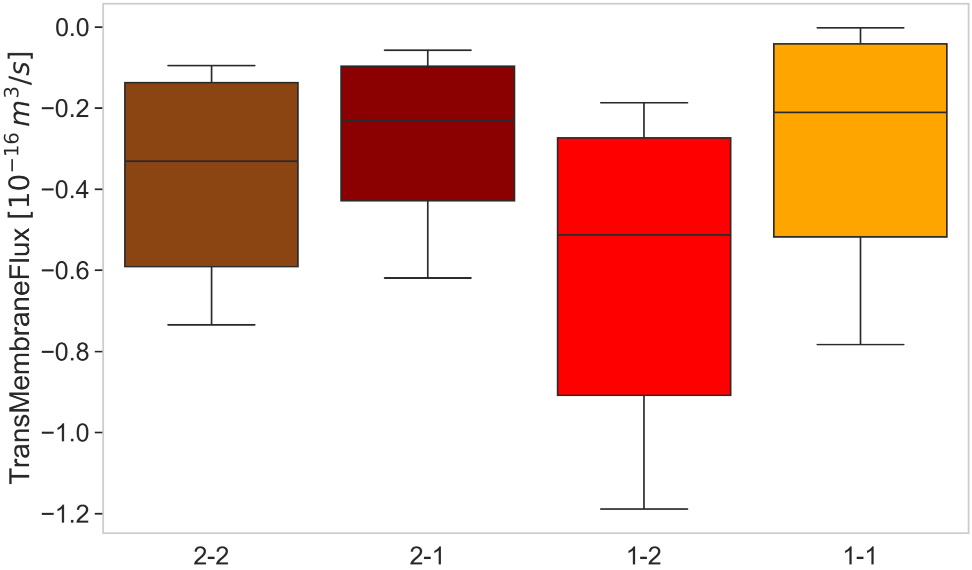

Figure 4.5: Transmembrane flux distribution for each topological configuration, represented by a box plot defined as in 4.2.

$|\hat{q}_c(\theta)|$. For example, a *more negative* value of $\hat{q}_c(\theta)$ is considered to be *higher*. The 1-in-2-out configuration distribution shows the highest median and the highest range of values, followed by the 2-in-2-out. Instead, the 2-in-1-out and 1-in-1-out ones seem to be the least relevant in terms of transmembrane flux. Note that, even if they are not visible in figure 4.5, some vessels $\theta \in \Theta$ are such that $\hat{q}_c(\theta) > 0$: in those cases there is an oxygen flux from brain tissue to capillaries.

4.4 Oxygen density

The idea behind this property is assessing the average oxygen concentration around a vessel. Therefore, data about oxygen concentration $P_T(\omega)$ is needed for each $\omega \in \Omega$, where Ω is the 3d domain (the definition of Ω can be found in 2.3.1). Taken a vessel $\theta \in \Theta$, the *theoretical* oxygen density, called $\mathcal{D}(\theta)$ is defined as:

$$\mathcal{D}(\theta) = \frac{1}{|V_\theta|} \int_{V_\theta} P_T(w) d\Omega \tag{4.13}$$

in which $|V_\theta|$ is the volume of the tissue region V_θ considered around vessel θ. In practice, P_T is only known in each cell centre $\omega_i \in \Omega$, $1 \leq i \leq 4 \cdot 10^6$ of the 3d discretization (see section 2.3.5 for the 3d discrezation description), thanks to the DuMux simulation. Thus, it is only possible to compute an esteem $D(\theta)$ of $\mathcal{D}(\theta)$:

$$D(\theta) = \frac{1}{n_{V_\theta}} \sum_{w_i \in V_\theta} P_T(w_i) \tag{4.14}$$

where n_{V_θ} is the number of cell centres in the tissue region V_θ. $D(\theta)$ is the actual oxygen density computed $\forall \theta \in \Theta$.

The main problem of oxygen density assessment is V_θ. Indeed, there are different concepts of *space around a vessel* where considering oxygen concentration. Literature on the matter [Schmid et al., 2021] [Sakadžić et al., 2014] only takes into account topological features, while suggesting that P_T should be regarded for more precision. Starting from these premises, four methods in this work have been developed to assign a tissue volume to each vessel. The first two of them, that are called oxygen brutal and oxygen refined, embed each capillary, arteriole or venule in a section of the surrounding tissue. These sections do not necessarily add up to the whole 3d domain. Instead, the third and the fourth ones, named oxygen Schmid and oxygen gradient, assign each cell of the 3d discretization to a vessel, so that the whole 3d domain is divided into sections belonging to different vessels. Details about each one of the four methods follow, along with some results.

4.4.1 Oxygen brutal

The most direct way of associating a tissue volume to a vessel $\theta = \{(u_{i,\theta}, v_{i,\theta})\}_{1 \le i \le n_\theta} \in \Theta$ is by enclosing it in a parallelepiped $\mathcal{P}_\theta$. A brief description of how this procedure is conducted is now given. First, notice that θ can also be written as a sequence of nodes $\{p_{i,\theta}\}_{1 \le i \le n_\theta + 1}$, where $p_{i,\theta} = u_{i,\theta}$, $1 \le i \le n_\theta$ and $p_{n_\theta+1,\theta} = v_{n_\theta}$. They are the extrema of the edges that compose the vessel. Then, the following steps are made:

(i) find the closest cell centre $\nu_{i,\theta}$ to $p_{i,\theta}$, $1 \le i \le n_\theta + 1$. Formally, find $\nu_{i,\theta}$, $1 \le i \le n_\theta + 1$, such that:

$$\nu_{i,\theta} = \underset{1 \le j \le 4 \cdot 10^6}{\arg\min} \left[d_e(w_j, p_{i,\theta}) \right] \tag{4.15}$$

(ii) build a list $\mathcal{X}$ containing all the x coordinates $x_{i,\theta}$ of every node $\nu_{i,\theta}$, $1 \le i \le n_\theta + 1$;

(iii) build a list $\mathcal{Y}$ containing all the y coordinates $y_{i,\theta}$ of every node $\nu_{i,\theta}$, $1 \le i \le n_\theta + 1$;

(iv) build a list $\mathcal{Z}$ containing all the z coordinates $z_{i,\theta}$ of every node $\nu_{i,\theta}$, $1 \le i \le n_\theta + 1$;

(v) compute $x_{min} = \min(\mathcal{X})$, $x_{max} = \max(\mathcal{X})$, $y_{min} = \min(\mathcal{Y})$, $y_{max} = \max(\mathcal{Y})$, $z_{min} = \min(\mathcal{Z})$, $z_{max} = \max(\mathcal{Z})$;

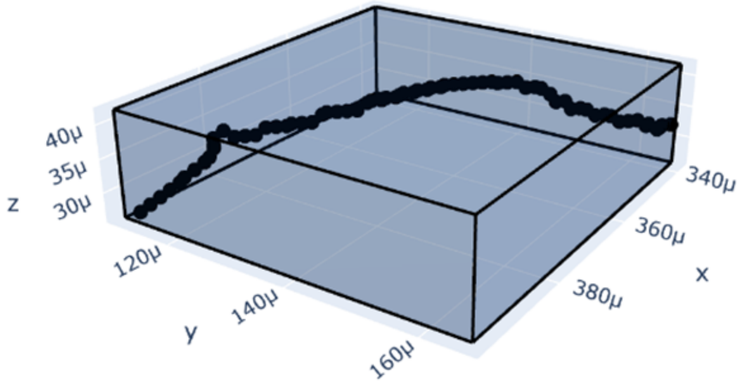

Figure 4.6: Visualisation of a vessel $\theta \in \Theta$ and of $\mathcal{P}_\theta$. In the figure, θ is represented by plotting the nodes $\{p_{i,\theta}\}_{1\le i\le n_\theta+1}$. The unit of measure of the axes is m. μ stands for 10^{-6}, so, for example, $120\mu = 120 \cdot 10^{-6}$.

(vi) compute $\bar{x}_{min} = x_{min} - \frac{d}{2}$, $\bar{x}_{max} = x_{max} + \frac{d}{2}$, $\bar{y}_{min} = y_{min} - \frac{d}{2}$, $\bar{y}_{max} = y_{max} + \frac{d}{2}$, $\bar{z}_{min} = z_{min} - \frac{d}{2}$, $\bar{z}_{max} = z_{max} + \frac{d}{2}$, where d is the side length of the cubic finite element of the 3d discretization[3];

(vii) build $\mathcal{P}_\theta = [\bar{x}_{min}, \bar{x}_{max}] \times [\bar{y}_{min}, \bar{y}_{max}] \times [\bar{z}_{min}, \bar{z}_{max}]$. This is the parallelepiped associated with the vessel.

Step (vi) ensures that $p_{i,\theta} \in \mathcal{P}_\theta, 1 \le i \le n_\theta + 1, \forall\, \theta \in \Theta$. Note that $\mathcal{P}_\theta \equiv V_\theta$ in 4.14. It is possible to find a visual representation of a vessel θ and of the parallelepiped $\mathcal{P}_\theta$ assigned to it in figure 4.6.

4.4.2 Oxygen refined

A more *refined* approach to embed a vessel θ into a tissue region V_θ is by wrapping it in a generalised cylinder with constant cross section. This is the idea behind the oxygen refined method. It is implemented for each $\theta = \{p_{i,\theta}\}_{1\le i\le n_\theta+1} \in \Theta$ as follows:

(i) find the closest cell centre $\nu_{i,\theta}$ to $p_{i,\theta}, 1 \le i \le n_\theta + 1$ (see step (i) of the oxygen brutal method 4.4.1);

(ii) build a cube $\mathcal{C}_{i,\theta}$ centred in $\nu_{i,\theta}, 1 \le i \le n_\theta + 1$. $\mathcal{C}_{i,\theta}$ has a side length of $(2r + 1) \cdot d$, where $d = 2.5 \cdot 10^{-6}\, m$ is the side length of the cubic finite element and $r = 5$ is a parameter specified in input;

(iii) consider the parallelepiped $\mathcal{C}'_{i,\theta} = \mathcal{C}_{i,\theta} \cap \Omega$ (most of the times $\mathcal{C}'_{i,\theta} = \mathcal{C}_{i,\theta}$). This needs to be done as Ω, described in section 2.3.1, is bounded;

---

[3] As mentioned in section 2.3.5, they are all of the same size.

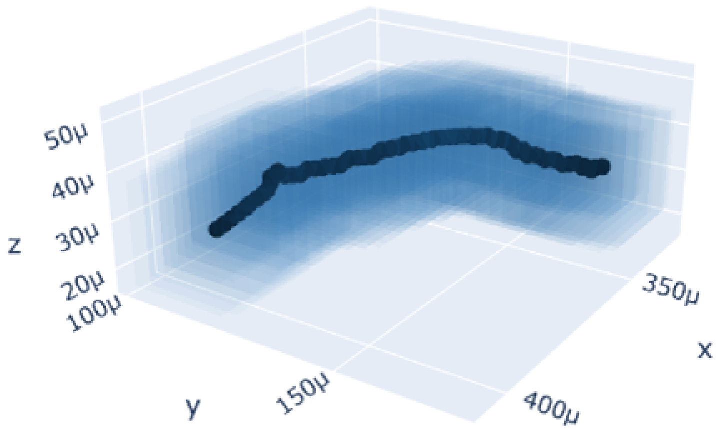

Figure 4.7: Visualisation of a vessel $\theta \in \Theta$ and of V_θ, according to the oxygen refined method. The features of the plot are the same as in 4.6.

(iv) define V_θ, the *generalised cylinder*[4] in which vessel θ is embedded:

$$V_\theta = \bigcup_{1 \le i \le n_\theta + 1} \mathcal{C}'_{i,\theta} \tag{4.16}$$

In point (ii) the size $(2r+1) \cdot d = 27.5 \cdot 10^{-6}$ m is chosen so that the generalised cylinder V_θ has approximately half the radius R_t indicated in [Sakadžić et al., 2014]. In this paper it is established that, in the cerebral cortex of the mouse, if the volume closer to each vessel were deformed into a cylinder, R_t would be its radius. The value of R_t is halved as the oxygen refined method is aimed at finding only the tissue that immediately surrounds a vessel. In figure 4.7 a vessel θ wrapped in V_θ is depicted.

4.4.3 Oxygen Schmid

The following two methods differ from the first two presented as they assign each discretization cell to a different vessel instead of embedding a vessel in a tissue region. The first is called oxygen *Schmid*, as it was suggested by Dr. Franca Schmid, in line with what has been done in her paper [Schmid et al., 2021]. The concept that leads to this method is associating each cell centre $w_j \in \Omega, 1 \le j \le 4 \cdot 10^6$ with the *closest* vessel in Θ[5]. The definition of *closest* vessel $\theta_j = \{p_{i,\theta_j}\}_{1 \le i \le n_{\theta_j}+1} \in \Theta$ to a cell centre $w_j \in \Omega$ is:

$$\theta_j = \arg\min_{\theta \in \Theta} \left[\min_{1 \le i \le n_\theta + 1} d_e(w_j, p_{i,\theta}) \right] \tag{4.17}$$

---

[4] It is just an approximation of a generalised cylinder.

[5] The definition of Θ can be found in 2.3.1.

It is the vessel containing the point that is closest to the cell centre based on the Euclidean distance $d_e(\cdot\,,\cdot)$.

In practice, before performing the assignment according to 4.17, these steps are made:

1) all vessel points are collected in a list $\mathbb{P} := \{p_{i,\theta}\}_{\theta\in\Theta, 1\leq i\leq n_\theta+1}$
2) a KD-tree structure $\mathbb{K}(\mathbb{P})$ is built with $\mathbb{P}$. A KD-tree is a data structure that organizes points in a K dimensional space. Given a set of points (that in this case is $\mathbb{P}$), a KD-tree allows to find the closest among them to an input one in a fast way [Skrodzki, 2019].

$\mathbb{K}(\mathbb{P})$ is then used to find the closest point in $\mathbb{P}$ to each cell centre w_j, $1 \leq j \leq 4 \cdot 10^6$. The algorithm employed for this is *spatial.KDTree.query* of the *scipy* Python library, which is based on [Maneewongvatana and Mount, 1999]. Then, θ_j is retrieved, in line with definition 4.17. Each vessel θ is now associated with a list of cells that have been assigned to it. V_θ is defined as the union of all those cells. In this way, $\cup_{\theta\in\Theta} V_\theta = \Omega$. A visual representation of a vessel and the tissue region associated with it by this method is visible in figure 4.8. Note that the volume assigned by the oxygen Schmid method is strongly related to the length and tortuosity features described in 3.

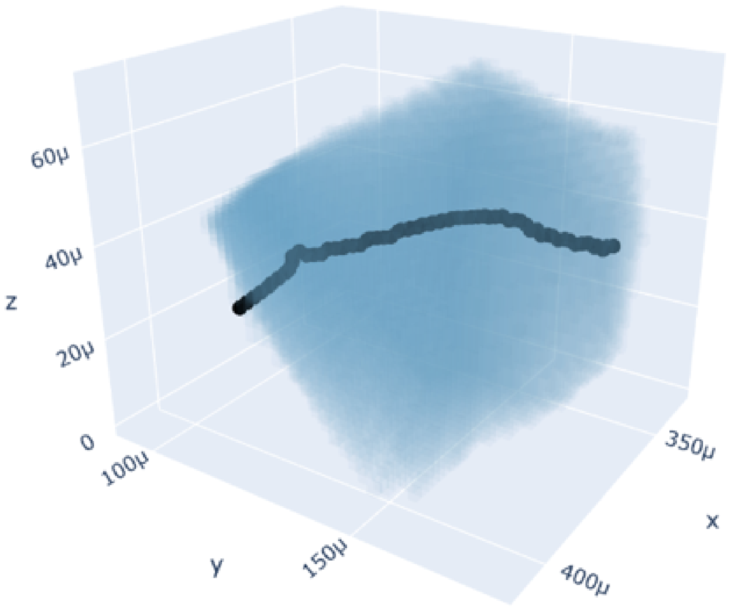

Figure 4.8: Visualisation of a vessel $\theta \in \Theta$ and of V_θ, according to the Schmid method. The features of the plot are the same as in 4.6.

4.4.4 Oxygen gradient

The second method that assigns each cell centre $w_j \in \Omega$ to a vessel $\theta \in \Theta$ is the most sophisticated among all four. Indeed, it involves a *gradient ascent* algorithm to find the vessel that oxygenates a cell. The reason behind this is now briefly and intuitively explained. In the stationary setting adopted in this work, at each cell centre $w_i \in \Omega$ there is a net flux of zero, considering the source, consumption and diffusion terms (see equation 2.7). Concerning diffusion, the direction from which a cell is oxygenated the most is given by ∇P_T. Indeed, this is the term that governs the direction of the oxygen flux due to local differences in oxygen concentration. This suggests that following the direction of ∇P_T, starting from a discretization cell, is a sound way of finding the vessel responsible for oxygenating it. The most straightforward way of doing so is by the aforementioned *gradient ascent* framework. The implementation of the idea presented is done according to an iterative structure. For each cell centre $w_i \in \Omega$, $1 \leq i \leq 4 \cdot 10^6$:

(i) the counter n_{it} is set to 0;

(ii) the gradient $\nabla P_T(w_i)$ is computed thanks to a five point discretization approximation scheme[6];

(iii) a step $s = 1$ is initialised. s is reduced, dividing it by a random int $q \in [2, 20]$, until $||s\nabla P_T(w_i)||_2 < k$, where $k = 4 \cdot 10^{-6}$ is a threshold specified in input;

(iv) $\tau_i' = w_i + s\nabla P_T(w_i)$ is computed;

(v) the closest cell centre ν_i to τ_i' is found, according to expression 4.15 (see figure 4.9);

(vi) the following conditions are considered:

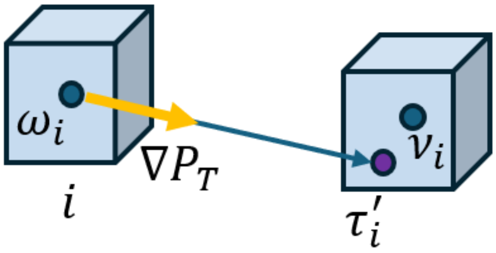

Figure 4.9: Visualisation of step (iv) of the gradient. The closest cell centre ν_i to τ_i' is found.

---

[6] More information in the Appendix 8.

- if the cell centred in ν_i is such that a *vessel θ passes through it* or if this cell has already been assigned to a vessel θ, the algorithm is stopped. w_i is assigned to θ;
- else if $n_{it} < N$, with $N = 1000$, and $||\nabla P_T(w_i)||_2 > m$, with $m = 10^{-6}$, the update $n_{it} = n_{it} + 1$ takes place and the algorithm goes to step (ii), with ν_i in place of w_i;
- else, consider the closest vessel θ to ν_i according to equation 4.17. w_i is assigned to θ.

In (iii), the interval for the value of q and the threshold $k = 4 \cdot 10^{-6}$ are based on several numerical experiments. Note that the value of k is such that the new point detected in (iv) is in a range comparable to the size length $d = 2.5 \cdot 10^{-6}$ m of the discretization cube. In (vi), a vessel is considered to *pass through a cell* if that cell belongs to the V_θ computed with the oxygen refined method 4.7, imposing $r = 3$. Numerical evidence indicates that this value of the radius allows one to balance the need for a small tissue region around a vessel with the requirement of a sufficiently large region that can be reached by the gradient ascent algorithm. Finally, the values of N and m were determined through empirical tuning.

In practice, for computational reasons, the steps (i)-(vi) are performed only for an evenly spaced grid $G \subset \Omega$, coarser than the computational mesh. For each cell $i \in \Omega \setminus G$, its closest cell $j \in G$ is retrieved. Then, i is assigned to the vessel associated with j.

As in section 4.4.3, each V_θ consists of the union of cells that have been assigned to θ. In figure 4.10, a vessel θ and the tissue region V_θ according to the gradient method are de-

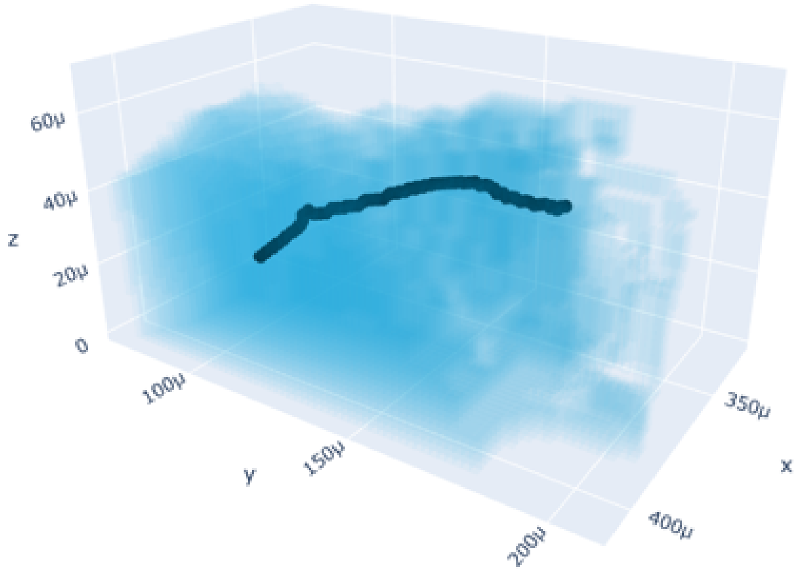

Figure 4.10: Visualisation of a vessel $\theta \in \Theta$ and of V_θ, according to the gradient method. The features of the plot are the same as in 4.6.

picted. Note that V_θ has a more irregular shape with respect to the tissue regions assigned by the other methods. This is because the gradient algorithm can classify differently two cells that share a face. However, this happens mostly for the cells towards the boundary of V_θ.

4.4.5 Results

For all the four methods, after establishing V_θ, the oxygen density $D(\theta)$ is computed $\forall\theta \in \Theta$ according to formula 4.14. To be precise, $\bar{D}(\theta)$ is calculated, defined as follows:

$$\bar{D}(\theta) = \alpha_T V_{cell} D(\theta) = \frac{V_{cell}}{n_{V_\theta}} \sum_{w_i \in V_\theta} \alpha_T P_T(w_i) = \frac{1}{n_{V_\theta}} \sum_{w_i \in V_\theta} [c(w_i) V_{cell}] = \frac{1}{n_{V_\theta}} \sum_{w_i \in V_\theta} [\mathcal{O}(w_i)] \quad (4.18)$$

where V_{cell} is the volume of a discretization cell (a cube)[7], $c(w_i)$ is the concentration of oxygen associated to the cell i and $\mathcal{O}(w_i)$ is the oxygen volume associated to cell i. $\bar{D}(\theta)$ is another way of expressing the oxygen density, that returns the average oxygen volume per cell. It is chosen as it is more intuitive than $D(\theta)$. In figure 4.11, different colour bars are used

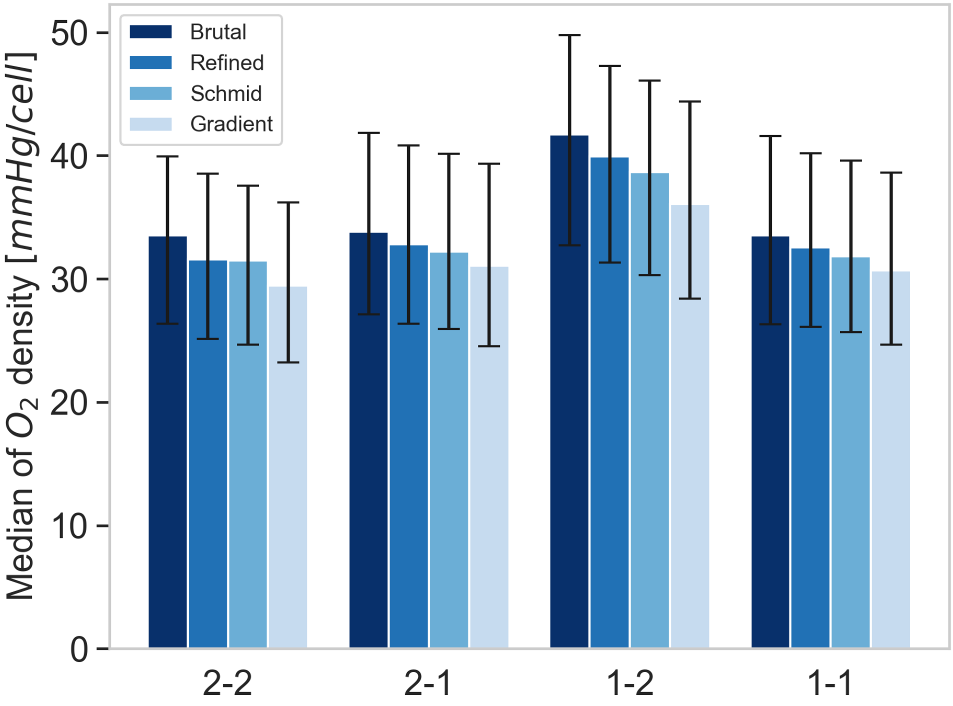

Figure 4.11: Data distribution of oxygen density for each method employed and for each topological configuration.

---

[7] See section 2.3.5 for the description of the discretization.

for representing the median for the different methods across all topological configurations. Whiskers are employed to highlight the 50% of the data distribution centred in the median. The picture shows that the four methods give the same results concerning the ranking of the different configurations in terms of oxygen density. The 1-in-2-out configuration vessels seem to be surrounded by the most oxygenated tissue, in line with the fact that they tend to be closer to the arterioles. Instead, the oxygen density around the vessels belonging to the other configurations looks approximately the same. This suggests that the tissue shows comparable levels of oxygenation across all Ω, with the exception of some regions closer to arterioles.

4.5 Volume oxygenated

As mentioned in the introduction 4.1, the variable volume oxygenated is aimed at retrieving the size of the tissue region oxygenated by a vessel. This cannot be directly inferred from the mathematical framework of the oxygen simulation. However, the oxygen density discussion has led to the definition of a region V_θ associated with each vessel $\theta \in \Theta$, according to different methods. Notice that, in this framework, as the whole Ω is expected to be oxygenated, each discretization cell has to be assigned to a vessel. Thus, oxygen brutal and oxygen refined are

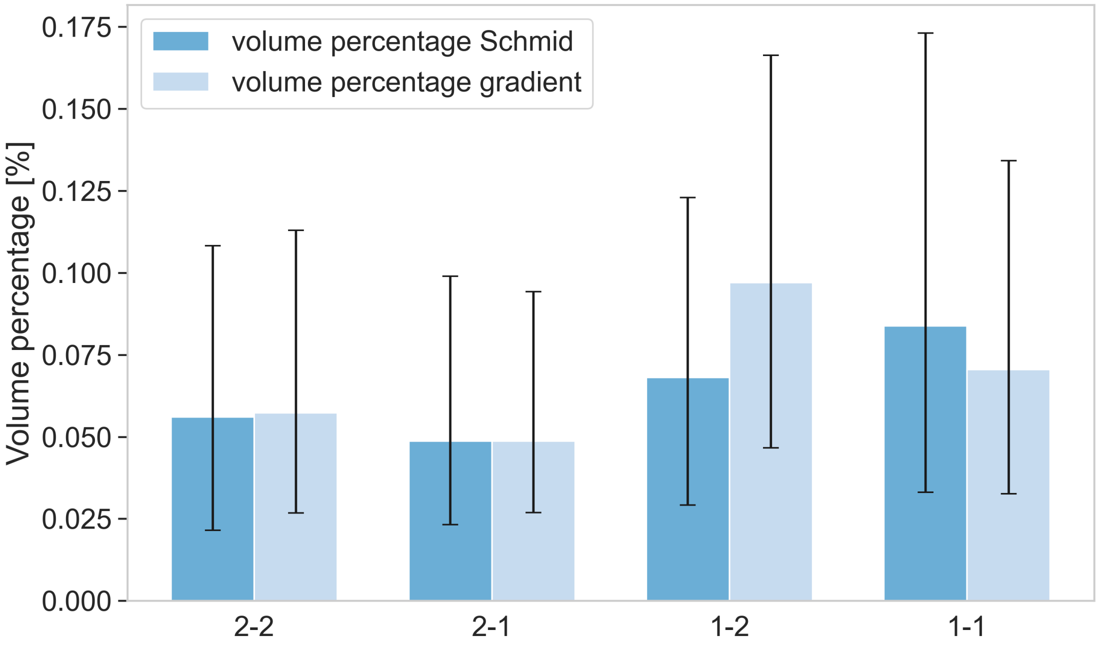

Figure 4.12: Data distribution of oxygen volume for the two methods employed and for each topological configuration. Colour bars are used for representing the medians. Whiskers are employed to highlight the 50% of the data distribution centred in the median.

not suited for this purpose. On the contrary, oxygen Schmid and oxygen gradient methods are aimed at splitting Ω among the different vessels. Thus, they are also used to find the oxygen volume $|V_\theta|$. Each vessel $\theta \in \Theta$ is then associated with the the volume percentage $\mathfrak{P}(\theta)$, defined as:

$$\mathfrak{P}(\theta) := \frac{|V_\theta|}{|\Omega|} \cdot 100 \tag{4.19}$$

$\mathfrak{P}(\theta)$ allows to understand what percentage of the tissue subsection[8] Ω is oxygenated by the vessel θ. The results for the volume percentage are displayed in figure 4.12. For both the Schmid and the gradient methods, the 2-in-2-out and 2-in-1-out configurations appear to be the least important in terms of volume percentage, while the 1-in-2-out and 1-in-1-out configurations seem to have the highest medians. However, the Schmid method ranks as first the 1-in-1-out configuration and as second the 1-in-2-out one, while the gradient does the opposite. Section 5.4 of the next chapter is devoted to validate the volume assignment and to better understand the difference between the two methods.

---

[8] $|\Omega|$ is the same for each one of the three sections analysed. See section 2.4.2.

5 Statistical analysis

5.1 Introduction

Throughout the previous chapters, results about the distribution of vascular properties across different topological configurations have been displayed and briefly commented. However, to draw meaningful conclusions, a more rigorous statistical analysis is needed. This chapter is aimed at providing it. Further analyses are then conducted for a deeper understanding of the data collected.

In section 5.2 the statistical framework is built. Suitable statistical tests to support the deductions made in chapters 3 and 4 are presented. Moreover, the ANCOVA method and its robust version are shown for additional data analysis. In section 5.3, the application of this framework to the data previously obtained is carefully conducted and results are displayed. Finally, further analyses about how the oxygenated volume is assigned to each vessel can be found in section 5.4. Besides giving deeper insights about the results in section 4.5, they serve as a validation of the methods described in chapter 4.

5.2 Statistical framework

This section is devoted to develop the proper mathematical tools to draw rigorous conclusions about the data shown in chapters 3 and 4. Since this work revolves around the contrast between different topological configurations, statistical methods to compare the data distributions of groups are discussed. In line with literature [Kim, 2015] [Midway et al., 2020] [Agbangba et al., 2024], it is first tested if the groups present significant differences, via an ANOVA or a Kruskal-Wallis test. Then, pairwise comparisons are made. In this sense, the t-test and the Mann-Whitney test are introduced. All the explanations for all the aforementioned statistical methods follow [Daniel and Cross, 2013] and [Verma and Abdel-Salam, 2019]. The ANCOVA method is then shown as a way of comparing categories based on a feature controlling for a continuous covariate. The standard description of this general linear model is accompanied by the presentation of a robust version of it, as can be found in [Wilcox, 2021]. Concerning all the methods discussed, particular attention is given to the underlying assumptions.

5.2.1 ANOVA and t-Test

A widely used approach for determining whether the mean of a property varies among different groups is the ANOVA (ANalysis Of VAriance). As ANOVA only tells if at least two groups differ, further analyses are needed to assess a ranking. The t-test is chosen for this purpose, with a Bonferroni correction to account for multiple comparisons. A more in detail description of these two statistical methods is now given.

ANOVA

The ANOVA is structured as follows. The variable whose difference among groups is analysed is called *response variable*. The categorical variable that determines the classification of elements into the groups takes the name of *factor variable*. When there is only one factor variable (as in chapters 3 and 4) it is possible to refer to the ANOVA as a *one-way* ANOVA. The goal of this statistical method is establishing if the variability in the *response variable* between elements in different groups is significantly higher than the variability within the groups. If so, it concludes that at least two groups differ. The one-way ANOVA relies on the following assumptions:

1) randomness: each observation must be collected randomly. This is usually implicit in the study design;
2) independence: the observations both within and between groups need to be independent one from the other. This is a design assumption;
3) normality: the data distribution in each group must be approximately normal. ANOVA is robust to violations of this assumption;
4) homoscedasticity: the variances of different groups must be comparable in size.

Note that it is also good practice to check for the presence of significant outliers, as they can heavily impact the results.

t-Test

If the ANOVA detects a significant difference in the mean of the *response variable* among groups, it is reasonable to establish a ranking. The t-test is the method selected in order to do that. To be accurate, the groups are pairwise compared via an independent two-sample t-test. This allows to state rigorously that the difference in means between the two groups is significant, taking into account the variability of this difference. The t-test relies on the same assumptions of ANOVA and is sensitive to the presence of outliers. Note that, when homoscedasticity is violated but normality is not, it is possible to adopt a variant of the t-test called Welch t-test.

Bonferroni correction

When establishing a ranking among more than two groups, multiple t-tests are conducted simultaneously. Since multiple hypotheses are checked at the same time, the probability of making a type I error[1] increases. To account for this problem, the significance level α for each individual t-test is adjusted according to the *Bonferroni correction*: α is divided by the number of t-tests. This allows for a significance level α for the overall ranking.

5.2.2 Kruskal-Wallis and Mann-Whitney tests

If the ANOVA and t-test assumptions are not satisfied, the Kruskal-Wallis and the Mann Whitney tests are valid alternatives, even if they are less precise in assessing the results. Moreover, they do not detect a difference in means, but a difference in medians or mean ranks[2]. From a statistical standpoint, they are *nonparametric* tests, meaning that they do not rely on premises about the distribution of the data. However, some assumptions still require checking before their usage. The Kruskal-Wallis test tells if there is a significance difference between at least two groups, whereas the Mann Whitney one is used for pairwise group comparison. A brief description of these methods is now presented.

Kruskal-Wallis test

The Kruskal-Wallis test is based upon a ranking of all the observation values across different groups. The ranking is conducted by putting the observation values in ascending order and by assigning ranks to them. Let N be the number of observations, these ranks $\{R_i\}_{i=1}^{N}$ go from 1 to N, associated respectively with the smallest and greatest values. A statistic is then computed relying on $\{R_i\}_{i=1}^{N}$. For the Kruskal-Wallis test to be effective, randomness and independence assumptions (see 5.2.1) need to hold.

---

[1] Rejecting a null hypothesis incorrectly. In the course of this work, saying that there is a difference in distributions between different groups when there is not.

[2] Ranks are defined in the following subparagraph. Details about the kind of difference between groups detected by these tests can be found in [Laerd Statistics, 2025].

Mann-Whitney test

Analogously to 5.2.1, if the Kruskal-Wallis test highlights a significant difference between the groups, a ranking can be found. This is done via pairwise comparisons, the Mann-Whitney test is used, that relies on the same weaker hypotheses of the Kruskal-Wallis test. Moreover, it revolves around a statistic computed using the ranks $\{R_i\}_{i=1}^{N}$ previously defined. Finally, a Bonferroni correction (see 5.2.1) is employed to account for multiple comparisons testing.

5.2.3 ANCOVA

So far, statistical methods involving only a single *response variable* and a single *factor* have been presented. However, the following question arises: is it possible to compare values between groups while controlling for a covariate? Indeed, for example, it could be insightful to compare the transmembrane flux between groups only considering vessels associated with similar values of blood flow (see chapter 4 for the definition of these variables). The standard way of answering this question is by performing an ANCOVA (ANalysis Of COVAriance) [Keppel, 1991]. This method relies on the same assumptions of ANOVA, i.e. independence, randomness, normality and homoscedasticty, plus the following two [Field, 2024]:

1) independence between factor and covariate;
2) homogeneity of the *regression slopes.*

In the second assumption, *regression slopes* refer to the slopes of the regression lines of the response variable on the covariate for every treatment.
As the assumptions of the standard ANCOVA are not always satisfied, robust methods have been developed. The one chosen in this work is taken from [Wilcox, 2021]. Let M be the number of groups in the study, for each group[3] $j \in [1, M]$:

(i) fix a range of N covariate variable values $\{c_i\}_{i=1}^{N}$;
(ii) $\forall i$, create a subgroup P_{ij} of observations that show a covariate value that is *close* to c_i;
(iii) compute the median m_{ij} of the response variable in each subgroup;

Then, groups are compared by fixing i and assessing the difference between medians m_{ij}, with $j \in [1, M]$. The significance of this difference is checked by making pairwise tests between the P_{ij} groups. In this sense, the Mann-Whitney test is employed, since checking the hypotheses for the t-test for each pair would be too computationally expensive. Note that the method presented does not require normality, homoscedasticity and homogeneity of regression slopes.

---

[3] Mathematical details can be found in [Wilcox, 2021].

Moreover, it is robust to the violation of the independence between factor and covariate, due to how the groups for comparisons are made. However, randomness and independence are still required for the Mann-Whitney test to be significant.

5.3 Implementation

The statistical framework developed is now applied to the data displayed in chapters 3 and 4. First, a pipeline is built to detect the significance of overall and pairwise differences between the groups. First the assumptions of the ANOVA and t-test (see 5.2.1) are checked and, if they are not satisfied, the Kruskal-Wallis and Mann-Whitney tests (see 5.2.2) are applied. Then, a further analysis is conducted by means of ANCOVA.

Before proceeding with the implementation description, it is important to discuss the design assumptions of randomness and independence, that underlie both the parametric and nonparametric methods mentioned.

5.3.1 Design assumptions

In the study design of this work, the randomness and independence assumptions are problematic. Concerning randomness, the vessels considered are not rigorously acquired in a random way from the microvasculature. As described in 2.4.2, the dataset consists of three networks embedded in three tissue sections, and not of a random sample extracted from the whole MVN1. However, due to similarities across subregions of the brain [Ji et al., 2021], the difference between the two procedures is considered to be mild. On the contrary, independence is a big issue. Indeed, for some of the previously introduced features (e.g. blood flow), correlation between different vessels can not be neglected, since it is intrinsic in the graph structure. Some methods to deal with this problem have been developed in the social network data analysis setting (see, for example, [Farine and Carter, 2022]). Nevertheless, they have not been employed in this work for two main reasons. The first is related to the complexity of their implementation, that is out of the scope of this work. The second concerns the fact that, in reality, they do not always guarantee to control for non-independence, to the point that in [Hart et al., 2022] it is suggested to rely on standard tests instead.

It follows from these premises that the results presented in the following sections, based on standard statistical tests, should be taken *cum grano salis*. This is especially relevant for the features now listed:

- AV factor, as it is reasonable to think that adjacent vessels have similar values of *closeness* to venules or arteries according to this measure;

- edge-betweeness centrality, because, if a vessel is central, vessels nearby tend to have a high centrality as well;
- blood flow, since it is expected that vessels on the same paths have highly correlated flows.

Note that these features are related to global aspects of the graph, in the sense that they take into account the role of the vessel with respect to the whole microvasculature.

5.3.2 Pipeline

After considering the limitations of the methods employed, the pipeline for statistical testing is now presented. First, it is established if there is an overall difference between the groups, following these steps:

(i) the normality of each group is tested via a Shapiro-Wilk test;

(ii) the homoscedasticity between all groups is tested through a Levene test;

(iii) these conditions are considered:

    - if the Shapiro-Wilk and the Levene test p-values are above a significance level $\alpha = 0.05$ for each group (normality and homoscedasticity hold), perform an ANOVA;
    - else, do a Kruskal-Wallis test.

The Shapiro-Wilk, Levene and Kruskal-Wallis tests are performed using respectively the `shapiro`, `levene` and `kruskal` functions from the scipy.stats library in python. The `f_oneway` function is taken from the same library for the ANOVA.
Afterwards, if the overall difference is detected, each pairwise comparison is conducted, considering the following conditions:

- if the Shapiro-Wilk p-value is below $\alpha_n = 0.01$ for at least one of the two groups (evidence of strong non-normality), do a Mann-Whitney test;
- else, if the Levene test p-value is lower than $\alpha = 0.05/4$ (evidence against homoscedasticity)[4], do a Welch's t-test;
- else, do a standard t-test.

The t-tests are performed using the function `ttest_ind` from scipy.stats, with the option `equal_variances` set to `True` if they are standard, to `False` otherwise. Instead, the Mann-Whitney test is conducted through the `mannwhitneyu` function of the same library.

---

[4] There is the Bonferroni correction mentioned in 5.2.1.

5.3.3 Results

The algorithm described in 5.3.2 always performs Kruskal-Wallis and Mann-Whitney tests. This indicates the presence of strong non-normality in the data within topological configurations and heteroscedasticity across them. The rankings and the significance of the comparisons are displayed in figures 5.1 and 5.2. A configuration that is located higher in the pictures corresponds to a higher rank with respect to the selected feature. Pairwise comparisons between groups are indicated with double-headed arrows. If a significant difference is detected, these arrows are coloured with red, otherwise with blue. Concerning topological features (figure 5.1), the results obtained mainly agree with the descriptive comments made in chapter 3. New aspects of the data concerning the tortuosity and AV factor features are highlighted. The statistical analysis conducted shows that the 1-in-2-out configuration is less

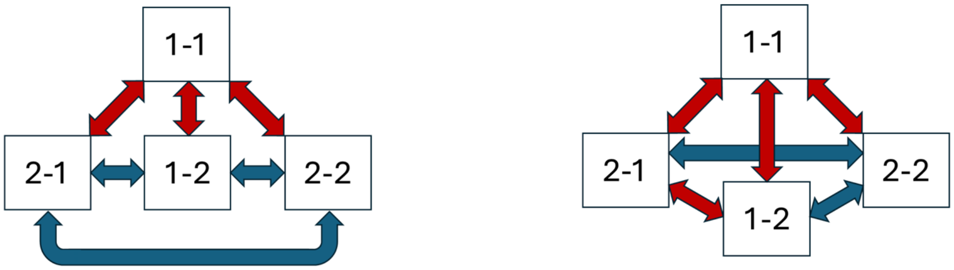

Length

Tortuosity

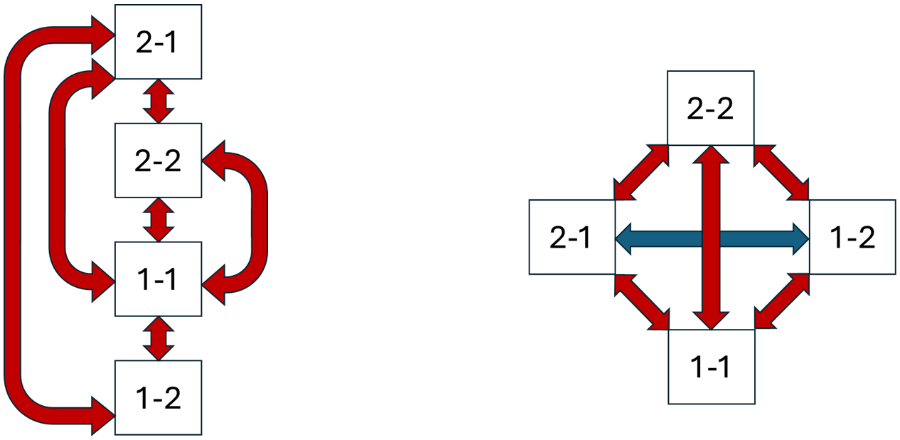

AV factor

Edge-betweenness centrality

Figure 5.1: Rankings of the topological configurations based on topological vascular features. Significant comparisons in red, otherwise in blue.

tortuous (in terms of overall distribution of the data) with respect to the 2-in-1-out and 2-in-2-out ones. This holds because the difference in tortuosity distribution between the 1-in-2-out and 2-in-1-out configurations is significant, even if the difference between the 1-in-2-out and 2-in-2-out ones is not. Moreover, regarding the AV factor, a significance difference is detected also between the 2-in-2-out configuration and the 1-in-1-out one. However, this conclusion must be taken *with a grain of salt*. Indeed, note that the medians of the 2-in-2-out and 1-in-1-out AV factor distributions are very close. In addition to this, the reader is reminded that the AV factor is a problematic feature in standard statistical testing (see 5.3.1).
Results about oxygen vascular features totally agree with what was observed in chapter 4, as shown in figure 5.2. Only the oxygen volume percentage ranking via the gradient method is shown, as the Schmid method leads to the same classification, except for the 1-in-1-out and 1-in-2 configurations, that are swapped. This is in line with the comments in section 4.5.

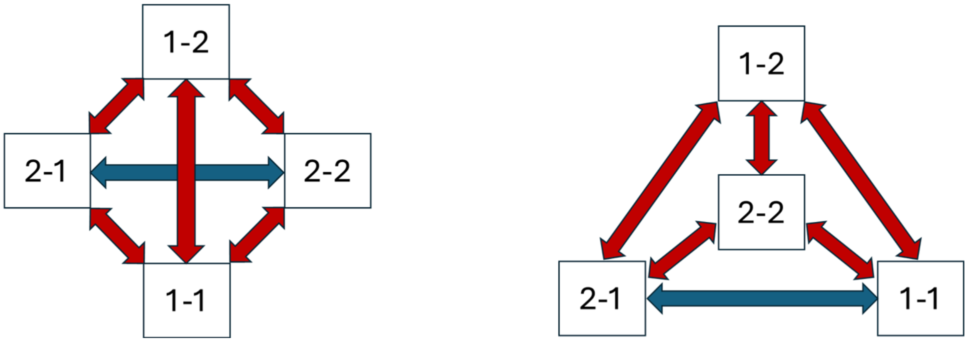

Oxygen flux

Transmembrane flux

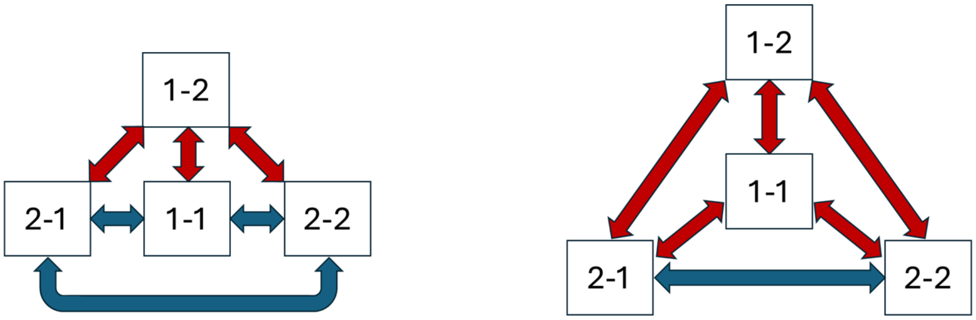

Oxygen density (all methods)

Oxygen volume percentage (gradient method)

Figure 5.2: Rankings of the topological configurations based on oxygen vascular features, as in figure 5.1

Finally, note that the oxygen density ranking is the same for all methods.

5.3.4 ANCOVA analysis

After having classified the topological configurations relying on different features, one may ask whether the rankings would change when controlling for a covariate. In this sense, two analyses are performed, in which configurations are compared based on the transmembrane flux $\hat{q}_C$ while controlling for the hematocrit H_D and the blood flow Q. The robust technique described in 5.2.3 is employed, with $N = 4$ and $\{c_i\}_{i=1}^4$ defined as the $20\%, 40\%, 60\%$ and 80% quantiles of the covariate empirical distribution. Results are displayed in figures 5.3 and 5.4 via a nonlinear regression plot for each topological configuration.

In figure 5.3, it is possible to observe that the transmembrane flux ranking does not change significantly when comparing vessels with similar values of H_D. Indeed, it is possible to observe that the 1-in-2-out configuration has the highest median transmembrane flux[5], followed by the 2-in-2-out and then by the 1-in-1-out and 2-in-1-out, whose medians are not significantly different. The only dissimilarity with the ranking in picture 5.1 lies in the fact that

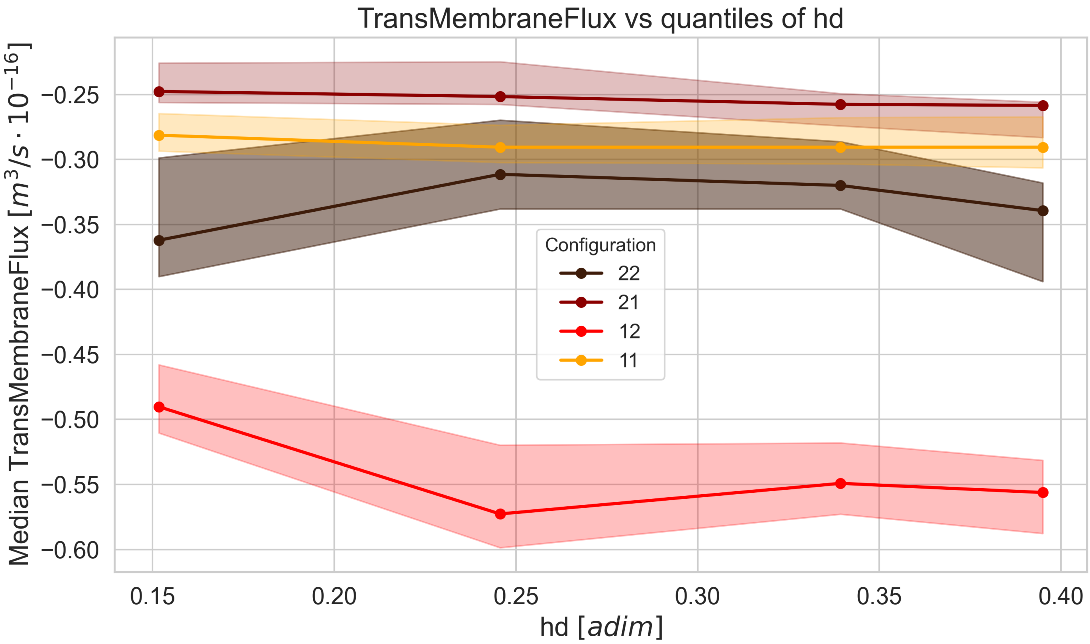

Figure 5.3: ANCOVA robust analysis of transmembrane flux across configurations while controlling for H_d (called *hd* in the plot). The shaded areas connect the 95% confidence intervals for the medians per hd quantile. They are computed using a bootstrapping method.

---

[5] As in section 4.5, note that the results are commented considering the absolute value $|\hat{q}_c(\theta)|$. For example, a *more negative* value of $\hat{q}_c(\theta)$ is considered to be *higher*.

there is no detected difference between the 2-in-2-out configuration and both the 1-in-1-out and 2-in-1-out.

The picture is much different in figure 5.4. When 1-in-1-out configuration vessels have higher values of blood flow, their median transmembrane flux is not significantly different to that of the 1-in-2-out configuration, even if its confidence interval is more widely spread. This points to the conclusion that 1-in-1-out configuration vessels are associated with high transmembrane flux values *relative to their blood flow value*. Therefore, although they are less important for the global perfusion of the graph, they play an important role in oxygenating specific tissue regions.

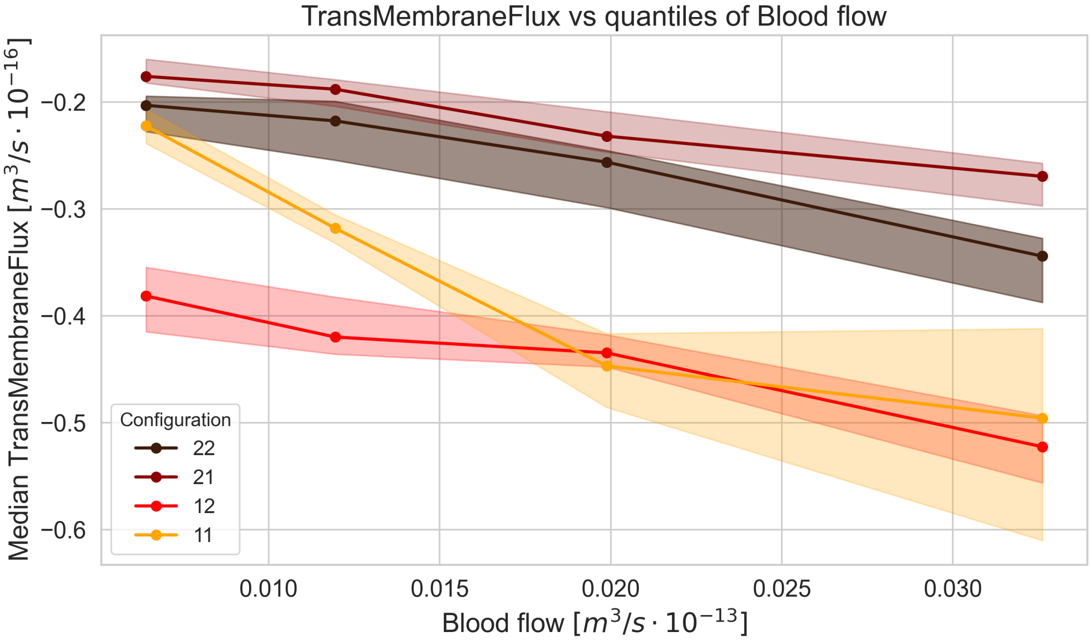

Figure 5.4: ANCOVA robust analysis of transmembrane flux across configurations while controlling for Q (called *Blood flow* in the plot). Shaded areas defined as in 5.3.

5.4 More on volume oxygenated

This section is aimed at checking the methods introduced for volume assignments made in section 4.5 and at better understanding the difference between the Schmid and the gradient method in terms of the results obtained.

5.4.1 Volume assignment check

In order to verify the volume assignment[6], the conservation of mass is checked for each tissue region $V_\theta \subseteq \Omega$. Thus, for both the Schmid and the gradient methods, equation 2.7 (pointwise conservation of mass) is integrated over V_θ:

$$-q_C + M(P_T) - \nabla \cdot (D_T \alpha_T \nabla P_T) = 0 \implies \int_{V_\theta} [-q_C + M(P_T) - \nabla \cdot (D_T \alpha_T \nabla P_T)] d\Omega = 0 \quad (5.1)$$

As the analytical expression of P_T is not known, this is done numerically. It is remembered that the DuMux simulation gives as output the oxygen partial pressure P_T in each cell centre $\omega_i \in \Omega$, so that a discretization of the integral in 5.1 is performed. Furthermore, if the volume assignment is performed correctly, V_θ surrounds θ, implying $\int_{V_\theta} [-q_c] d\Omega = \hat{q}_c(\theta)$. After these premises, equation 5.1 can be rewritten as:

$$\hat{q}(\theta) + \sum_{w_i \in V_\theta} [M(P_T)(w_i) - \nabla \cdot (D_T \alpha_T \nabla P_T(w_i))] = 0 \quad (5.2)$$

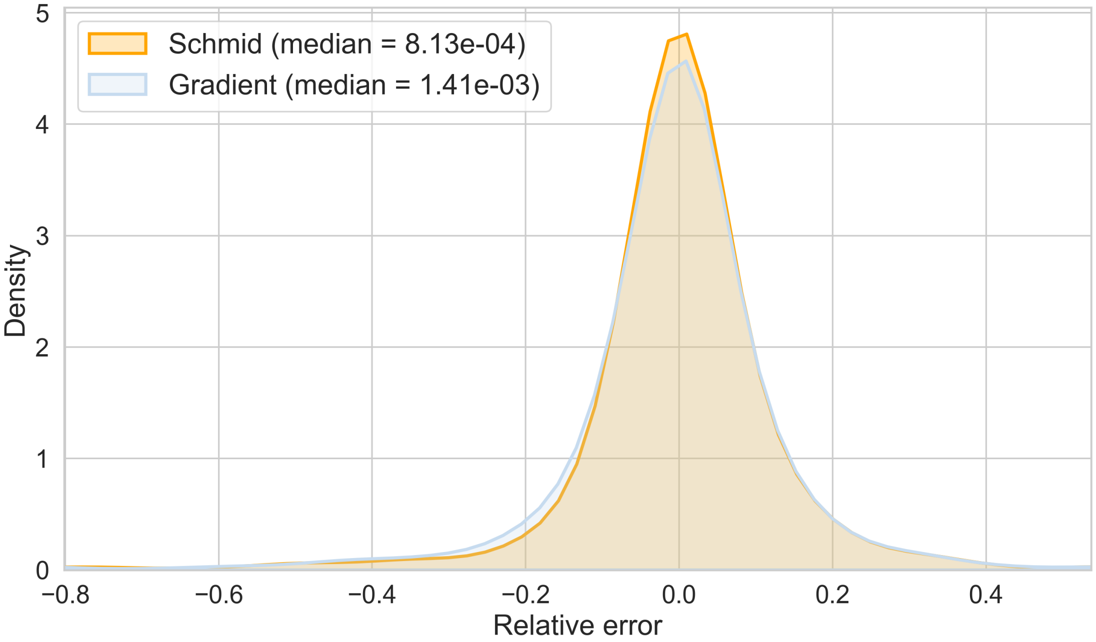

Figure 5.5: $\varepsilon_{rel,\theta}$ density distribution function, both for the Schmid (in orange) and gradient (in blue) methods.

---

[6] The reader is reminded that *volume assignment* means the *process of associating a vessel with the volume it supplies.*

The left side of 5.2, which is labeled as Γ_θ, is then computed. The laplacian term is evaluated via a finite difference approximation using a fourth order central difference scheme (see Appendix 8 for details). To understand if the value of Γ_θ is significantly close to 0, i.e. the volume assignment is correct, the following quantity is calculated:

$$\varepsilon_{rel,\theta} = \frac{3 \cdot \Gamma_\theta}{|M_\theta| + |L_\theta| + |\hat{q}(\theta)|} \tag{5.3}$$

where $M_\theta := \sum_{w_i \in V_\theta} [M(P_T)(w_i)]$ and $L_\theta := \sum_{w_i \in V_\theta} [-\nabla \cdot (D_T \alpha_T \nabla P_T(w_i))]$. This allows to put Γ_θ in relation to the terms that come into play in the mass conservation equation. Indeed, $\varepsilon_{rel,\theta}$ is the ratio between Γ_θ and the average of the absolute values of the terms on the left-hand side of equation 5.2.

The distribution density functions of $\varepsilon_{rel,\theta}$ for both the Schmid and the gradient method are shown in figure 5.5. Considering the presence of discretization and numerical errors, the results are quite satisfactory. Even if some outliers are present, for most of the vessels the relative error is below 10%, a good result considering that the dimensions of V_θ $\forall \theta \in \Theta$. Indeed, the median value of $\mathfrak{P}(\theta)$ is less than 0.1%, meaning that these tissue regions are extremely small if compared to Ω. Also, note that the distribution density functions are symmetrical and centered around 0. This points to the absence of a systematic source of the errors.

5.4.2 Oxygen and Schmid methods difference

After having checked the volume assignment, an analysis is conducted about the difference in volume oxygenated assessed by the Schmid and the gradient methods. While the two methods mostly agree on the overall ranking, they disagree on the comparison between the 1-in-2-out and the 1-in-1-out one configurations.

To understand this divergence in predictions, it is first important to reflect on how the division of Ω into $\{V_\theta\}_{\theta \in \Theta}$ should be conducted. As mentioned in section 4.1, V_θ is considered as the tissue region reached by the transmembrane flux of θ. This can be seen in a different way, in line with section 4.4.4: V_θ is the region that can be reached following the *streamline* of the vector field $-\nabla P_T$, starting from the vessel. Thus, if a vessel is oxygenating V_θ, dicretization cells w_i close to ∂V_θ should be such that $|| - \nabla P_T(w_i)|| \approx 0$[7]. However, vessels with a very small transmembrane flux (or even an ingoing one) exist. Concerning them, it is reasonable to think that V_θ is oxygenated by other vessels, implying that $||-\nabla P_T(w_i)|| \neq 0$ and $\nabla P_T(w_i)$ points towards them, for w_i close to ∂V_θ. Vessels of this kind are called *passive* vessels,

---

[7] If this were not true, other cells could be reached from ∂V_θ, but this leads to a contradiction.

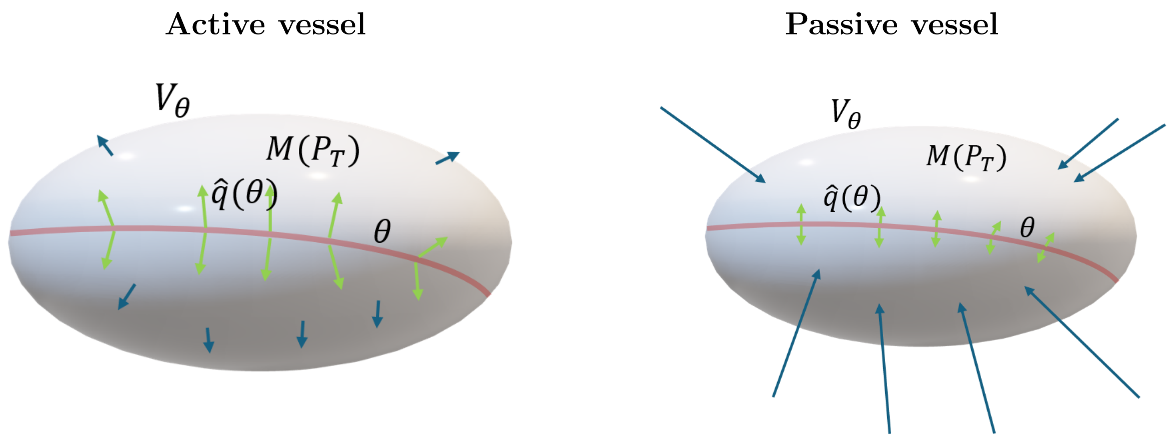

Figure 5.6: Visual representation of an active vessel (on the left) and of a passive one (on the right). The green arrows represent the transmembrane flux, while the blue ones represent the gradient on the surface (its magnitude is greater for the vessel on the right, as longer arrows indicate). The red line depicts the vessel, the white ellipsoid the volume assigned to it.

to underline the difference with respect to the ones described previously, that are instead labelled as *active* vessels (see figure 5.6).

After having described what is expected to happen, a procedure is developed to assess if the oxygen and Schmid method lead to results that agree with these premises. The key point is evaluating the gradient $-\nabla P_T$ on ∂V_θ, for all $\theta \in \Theta$. Since the point-wise evaluation of $-\nabla P_T$ on ∂V_θ is very computationally costly, a *weak* approach is chosen. In this sense, $\int_{\partial V_\theta}(-\nabla P_T \cdot \boldsymbol{n})d\Sigma$ is calculated $\forall \theta \in \Theta$, where $\boldsymbol{n}$ is the outward normal vector. Notice that, as D_T and α_T are constants:

$$\int_{\partial V_\theta}(-\nabla P_T \cdot \boldsymbol{n})d\Sigma \overset{(1)}{=} \int_{V_\theta} -\Delta P_T d\Omega \propto \int_{V_\theta} -\nabla \cdot (D_T \alpha_T \nabla P_T(w_i))d\Omega \approx L_\theta \tag{5.4}$$

where in (1) the divergence theorem is employed and L_θ is defined as in section 5.1.

To understand if L_θ can be considered negligible, as it is expected for the highest majority of vessels, $\varepsilon'_{rel,\theta} = L_\theta/\hat{q}(\theta)$ is calculated. Indeed, putting L_θ in relation to the transmembrane flux of the vessel allows for a more precise assessment of its closeness to 0 in the problem setting. Note that active vessels are expected to be such that $|\varepsilon'_{rel,\theta}| << 1$, as $L_\theta \approx 0$ in this case, while the passive ones should be such that $|\varepsilon'_{rel,\theta}| >> 1$, since $L_\theta >> \hat{q}(\theta)$ in this instance[8] . Two different distribution functions of $\varepsilon'_{rel,\theta}$ are represented for each method in

---

[8] The term evaluating the integral of the gradient on the surface is much bigger than the transmembrane flux of the vessel.

figures 5.7 and 5.8. One concerns the vessels such that $|\varepsilon'_{rel,\theta}| < 1$, the other those such that $|\varepsilon'_{rel,\theta}| > 1$. They are respectively called the active and passive ranges of $|\varepsilon'_{rel,\theta}|$. The motivation of this choice consists in the interest in understanding the difference between the two methods in the active and passive ranges of the $|\varepsilon'_{rel,\theta}|$ distribution, where active and

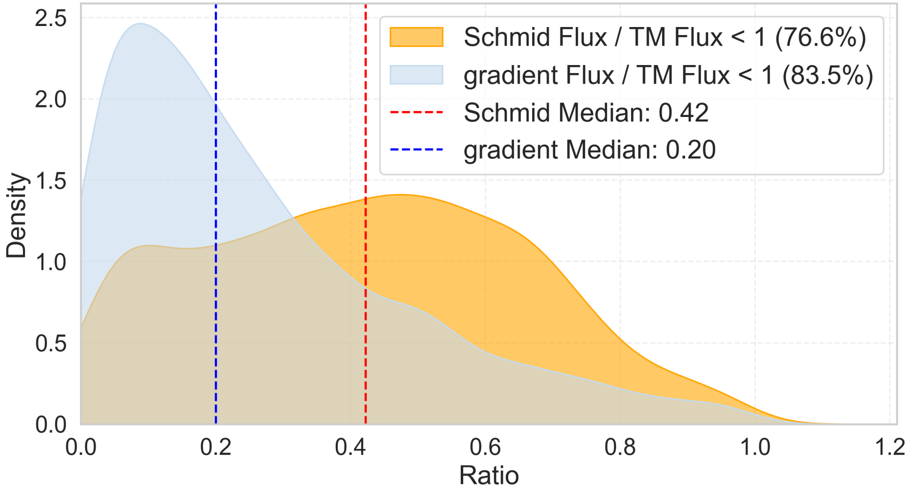

Figure 5.7: Density distribution of $|\varepsilon'_{rel,\theta}|$ (called *ratio* in the plot) in the active range ($|\varepsilon'_{rel,\theta}| < 1$), for the Schmid (in orange) and gradient (in blue) methods. The dotted vertical lines represent the median values of the distributions (shown in red and in blue for the Schmid and gradient methods, respectively). The percentage of the active vessels detected by each method is displayed in the legend.

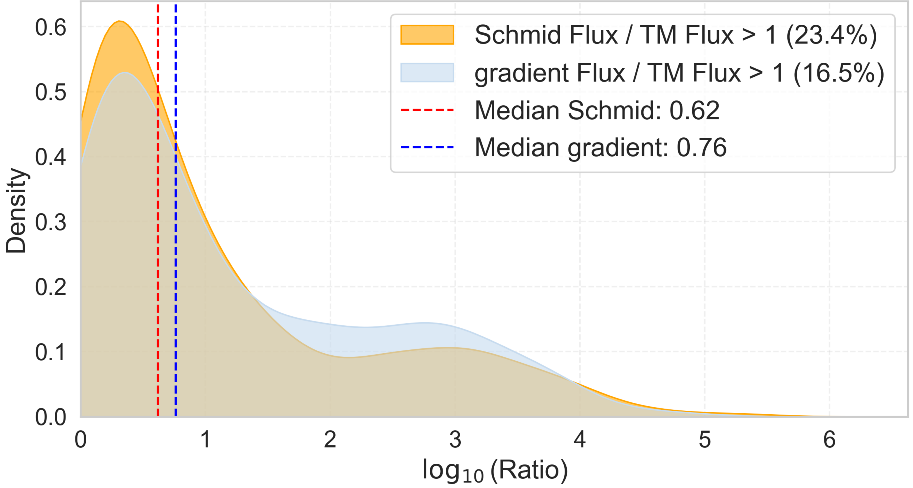

Figure 5.8: Plot (analogous to figure 5.7) of distributions of $|\varepsilon'_{rel,\theta}|$ (called *ratio* in the plot) in the passive range ($|\varepsilon'_{rel,\theta}| > 1$). The choice of the logarithmic scale for the x axis is motivated by the fact that the values of $|\varepsilon'_{rel,\theta}|$ are very spread out. The percentage of the passive vessels detected by each method is displayed in the legend.

passive vessels should respectively be found. While both methods find that more than 75% of the vessel lie in the active range, the gradient one leads to distributions that are more in line with theory. Values of $|\varepsilon'_{rel,\theta}|$ such that $|\varepsilon'_{rel,\theta}| < 1$ are closer to 0, while values of $|\varepsilon'_{rel,\theta}|$ such that $|\varepsilon'_{rel,\theta}| > 1$ are much greater with respect to the ones given by the Schmid method. This strongly suggests that the gradient method is more precise for the assessment of the oxygen volume percentage. When it comes to the comparison between the 1-in-2-out and 1-in-1-out configurations, the gradient method successfully accounts for the fact that the transmembrane flux exiting 1-in-2-out configuration vessels is higher and thus reaches a greater volume. Nevertheless, the Schmid method is useful: it just serves another purpose, evaluating the space around a vessel from a topological point of view.

6 Discussion

6.1 Introduction

This chapter is devoted to explaining how the results obtained so far can be used for the comprehension of the impact of vessel topology on oxygen supply to the brain.

In section 6.2, different strategies to assess the impact of a vessel on oxygen supply are discussed. The relation between these strategies and the features extracted in the previous chapters is analysed. Then, relying on the distribution of these features across the different topological configurations, in section 6.3 conclusions are made about the role of vessel topology in oxygen supply. The limitations of this work and its future developments are finally discussed in section 6.4.

6.2 Importance in oxygen supply

This section is dedicated to measuring the *importance* of vessels in oxygen supply. Three interpretations of importance are analysed:

- local, examining the tissue region surrounding each vessel;
- global, concerning the overall oxygenation of the brain tissue section of MVN1;
- network-related, assessing how crucial a vessel is for oxygen distribution in the microvasculature.

The first listed encapsulates the idea of considering the role of a vessel in oxygenating the region nearby. It is aimed at answering the following question: if a capillary were occluded, how would the oxygenation change in its proximity? To quantify the local importance, it is reasonable to employ the transmembrane flux, the oxygen density and the oxygen volume percentage. As a matter of fact, the first indicates how much oxygen exits the vessel to oxygenate the tissue region nearby, the second how well oxygenated this tissue region is, the third how far the transmembrane flux goes. The oxygen volume percentage mentioned derives from the gradient method. However, the same variable evaluated via the Schmid method can also be used to comprehend if a vessel can be replaced by other ones close to it when it comes to the oxygenation process. Indeed, it evaluates the space around it from a topological point of view. Note that the relation between local importance in oxygen supply and oxygen density is inverse. The more oxygenated the tissue region around a vessel is[1], the less (locally) important is the vessel, as the transmembrane fluxes of the vessels nearby are more likely to *fill* the region if the vessel is occluded.

The global importance concerns a more intuitive notion. The vessels are put in relation to the *overall oxygenation* of the MVN1 section. Here, *overall oxygenation* refers to the total oxygen stored in the tissue[2] and the total space that needs to be oxygenated. It is a descriptive idea, not related to structural aspects of the model. To measure it, the frequency, the length, the tortuosity, the oxygen density and the oxygen volume percentage features are used. The first three allow to understand the fraction of the total graph length that is covered by a vessel and how it curls up in space. Oxygen density serves a different purpose from the local importance setting. Its value for each vessel is divided by their sum over all vessels, in order to assess the importance of a capillary relative to the overall oxygenation.

The goal of the network-related importance is to comprehend the role of a vessel in the distribution of oxygen throughout the microvasculature. In particular, one might ask how the occlusion of a capillary impacts the perfusion of the whole tissue section [Schmid et al., 2021]. The key features for finding the answer are the AV factor, the edge-betweenness centrality and the oxygen flux[3]. The first is fundamental, as occlusions of capillaries close to arterioles or to venules, corresponding respectively to low and high AV factor values, are known to be dangerous for microcirculation in the brain [Shih et al., 2013]. Edge-betweenness centrality is also employed, giving valuable information about how a vessel relates to the different blood flow paths in the graph. Finally, the oxygen flux is the most straightforward feature for understanding the interaction between a capillary and the rest of the microvasculature in terms of oxygen distribution.

Figure 6.1 visually summarizes the three interpretations. In the local importance picture a), the transmembrane flux is represented by means of green vectors, the volume with a white elliposid and the blood vessel with a red line. Instead, in b), the global interpretation is rendered by highlighting a vessel and its oxygen volume in comparison to the tissue section. Finally, in the network-related importance figure c), the direction of blood flow is indicated

---

[1] All other features being equal (*controlling for* the other variables into play).

[2] The reader is reminded that a stationary solution is found in this work via the Dumux simulation. See section 2.3.

[3] Or blood flow, since highly correlated (see section 4.2.3).

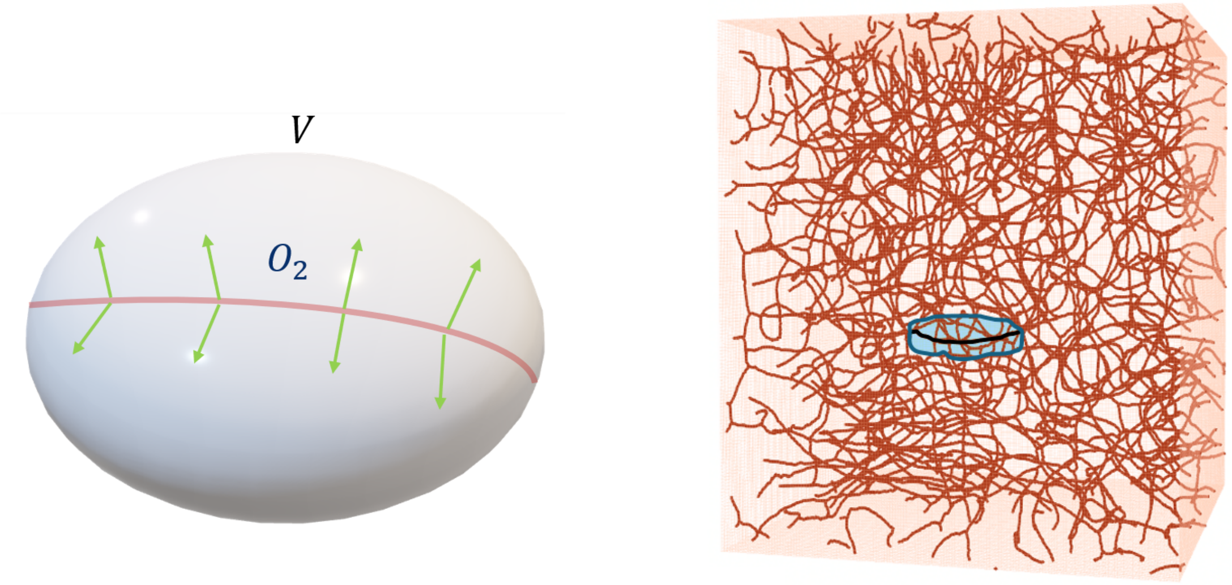

a) Local importance **b) Global importance**

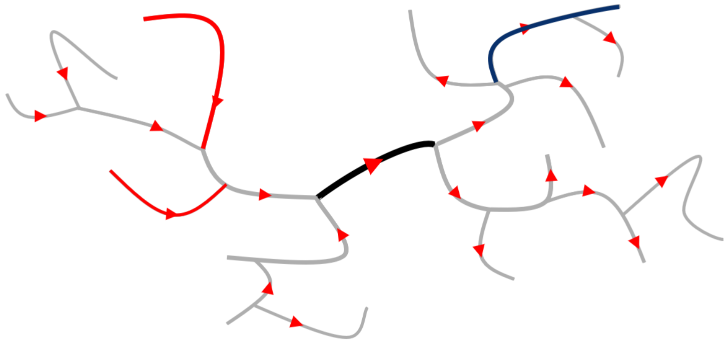

c) Network-related importance

Figure 6.1: Schematic visualisation of the three interpretations of importance of a vessel in oxygen supply. See pages 67-68 for in detail description.

with a red arrow, arterioles are coloured with red, venules with blue and capillaries with grey. The blood vessel under analysis is depicted in black

6.3 Conclusions

Based on their rankings concerning the vascular features mentioned in the previous section (see section 5.3.3), conclusions can now be drawn about the role of different topological configurations in oxygen supply.

6.3.1 2-in-2-out configuration

The 2-in-2-out configuration is the last in terms of oxygen volume percentage, the second with respect to the transmembrane flux and tied for second place with the 2-in-1-out and the 1-in-1-out configurations regarding oxygen density. For these reasons, its local importance is average. Indeed, even if the transmembrane flux is high for vessels belonging to this configuration, its range of action is low. This means that other capillaries, close to vessels belonging to this configuration, can assume their role (in terms of local oxygenation) in case of occlusion. When it comes to global importance, this configuration is negligible. This derives from the combination of its rare occurrence in the graphs and the fact that it does not stand out in terms of length, tortuosity, oxygen volume percentage or oxygen density. On the other hand, the 2-in-2-out vessels are relevant for the network-related importance. Although their AV factor behaviour points to an even distribution in the network, they are associated with high centrality values and significative oxygen flux levels.

6.3.2 2-in-1-out configuration

The 2-in-1-out configuration is joint last concerning oxygen volume percentage and transmembrane flux, and it is in line with the 1-in-1-out and the 2-in-2-out in terms of oxygen density. This allows to state that it has a minor local importance. Moreover, this configuration has an average global importance. It has an average behaviour concerning length, tortuosity, frequency and oxygen density, together with a low rank with respect to oxygen volume percentage. Howevever, its relevance in network-related terms is not negligible. The fact that vessels belonging to the 2-in-1-out configuration tend to be closer to venules make their potential occlusion dangerous. In addition to this, these capillaries are associated with significant values of edge-betweenness centrality and oxygen flux.

6.3.3 1-in-2-out configuration

The oxygen density of the 1-in-2-out configuration vessels tends to be the highest. This suggests that the tissue region around them is more robust to occlusions. Futhermore, 1-in-2-out vessels are associated with the greatest values of transmembrane flux and oxygen volume percentage, making them locally crucial. They are also slightly more relevant than 2-in-1-out vessels in global terms. Indeed, while these two configurations have similar distributions of length, tortuosity and frequency, the 1-in-2-out is superior when oxygen density is considered. Moreover, the 1-in-2-out configuration is fundamental for the distribution of oxygen throughout the whole microvasculature, i.e. in network-related terms. 1-in-2-out vessels are inclined to be closer to arterioles (AV factor distribution closer to 0), tend to be very central and are associated with very high oxygen flux values.

6.3.4 1-in-1-out configuration

The 1-in-1-out configuration is joint last with respect to transmembrane flux and it shows the same behaviour of the 2-in-1-out and the 2-in-2-out with respect to oxygen density. When it comes to the oxygen gradient method, this configuration is ranked second with respect to oxygen volume percentage. However, it is first in terms of the same feature according to the Schmid method, implying that 1-in-1-out vessels are surrounded by a higher extravascular tissue volume. All these considerations imply that the local importance of the 1-in-1-out configuration is not negligible. Instead, it is fundamental in global terms. Indeed, it is the most frequent topological configuration, together with being associated with the greatest tortuosity and length. Additionally, its oxygen volume percentage distribution is prominent both via the Schmid and gradient methods. Also note that the transmembrane flux of the 1-in-1-out configuration -relative to blood flow- distribution lies above those of the other configurations for average to high values of blood flow (see section 5.3.4, figure 5.4). This is a sign of the role of 1-in-1-out vessels in efficient oxygen release into tissue. Finally, their network-related importance is minor: their AV factor values indicate an even distribution in the network, and they are ranked last in terms of edge-betweenness centrality and oxygen flux.

6.3.5 Summary

Since a constant oxygen supply to the brain is fundamental for survival, any kind of disturbance in this sense can cause significant health issues. In particular, occlusions of capillaries in the microcirculation are associated with neurodegenerative diseases. Therefore, to better understand the genesis of these conditions, the role of capillaries in brain oxygenation must be examined.

In this work, a numerical framework simulating oxygen supply to the brain is employed. Then, the results obtained are analysed to understand if the impact on brain oxygenation of

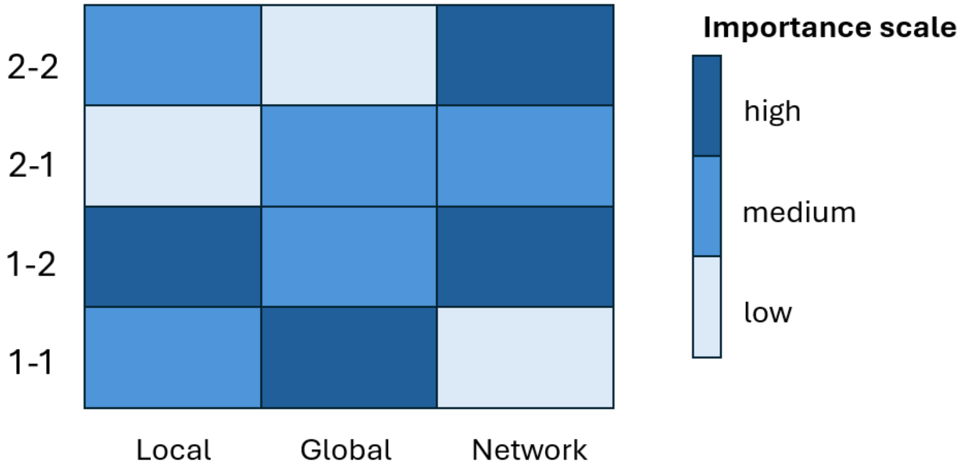

Figure 6.2: Heatmap table of configuration vs importance interpretation. *2-2*, *2-1*, *1-2* and *1-1* stand respectively for *2-in-2-out*, *2-in-1-out*, *1-in-2-out* and *1-in-1-out* configurations. *Network* means *network-related*.

.

different vessels can be assessed solely via their blood flow behaviour, allowing for a reduction of computational costs. To this end, the vessel topology feature is introduced, dividing vessels into categories, called topological configurations, based on blood flow direction in their proximity. The conclusions are drawn relying on the distribution across different topological configurations of other features, whose link with brain oxygen supply *importance* is more direct. Note that different interpretations of *importance* are considered in order to have a precise picture of the results.

In figure 6.2, a summary of the conclusions is visually represented. It is evident that the importance of a blood vessel for brain oxygen supply can be inferred from its topology. Concerning local importance, the 1-in-2-out configuration is the most relevant, followed by the 2-in-2-out and 1-in-1-out, approximately on the same level. The least significant in this sense is the 2-in-1-out configuration. The 1-in-1-out configuration is clearly the most important for the overall oxygen supply to the brain. It does not only supply the largest volume of tissue, but it is also very efficient, as comparing the transmembrane flux controlling for blood flow suggests. This is in line with what is postulated in [Schmid et al., 2021]. The least globally significant configuration is the 2-in-2-out one, while the 2-in-1-out and 1-in-2-out ones are joint second in the ranking. With respect to network-related importance, the occlusion of a 1-in-2-out vessel is found to be potentially dangerous for the perfusion of the tissue section. This agrees with literature about *in vivo* analyses of the somatosensory cortex of the mouse, due to the fact that 1-in-2-out vessels tend to be arterioles, or at least closer to the arterial side. For example, in [Shih et al., 2013], it is established that microinfarcts involving arterioles and venules have the most devastating effects on oxygen supply to the mouse brain. According to [Nishimura et al., 2007], arterioles are “bottlenecks in the link between surface arterioles and the tortuous network of microvessels” and there is evidence showing that large sections of brain tissue are supplied by an individual penetrating arteriole. [Lecoq et al., 2011] states that arterioles are crucial for oxygen supply in the olfactory nerve layer as well, also validating their prominent local importance. Microinfarcts involving 2-in-2-out vessels are determined to be harmful for the whole tissue section perfusion as well, extending the analogous result about blood flow in [Schmid et al., 2021]. The network-related importance of 2-in-1-out vessels, that tend to be close to the venous side, is not minor. To assess it more precisely, other information, comprising the total outflow from the considered tissue section, is probably needed. On the contrary, there is evidence that 1-in-1-out vessels are negligible in this sense. Thus, the idea suggested in [Schmid et al., 2021] about the danger deriving from their occlusion is confirmed only from a local perspective, and opposed from a network-related one. Given that the majority of vessels belong to the 1-in-1-out configuration, these results suggest an intrinsic resilience of the brain microvasculature to microinfarcts.

6.4 Limitations and perspectives

Setting aside the limitations of the model[4] shown in chapter 2, this work has a fundamental weakness. The impact of a vessel on oxygen supply, relying on the definitions given in section 6.2, is assessed quantitatively only in the case of global importance. Concerning the local and network-related importances, no mathematical measure is introduced, so that the conclusions made subsequently that involve them are not completely rigorous. Further analyses are thus needed to confirm a great part of the results. Another significant shortcoming of this study comes from the limitations of the statistical analysis conducted in chapter 5 (see section 5.3.1).

Gaia Stievano, PhD student at Bern University, is currently investigating the network-related importance of vessels [Stievano, nd]. In her work, a simulation analogous to the ones analysed in chapters 3, 4 and 5 is first run. Then, many simulations of single capillary occlusions are performed and classified according to the capillary topological configuration. The results obtained by Stievano seem to confirm the conclusions previously presented. Further work is still required to be conclusive both in terms of local and global configuration importance.

Future developments may also include a study of the relation between features and oxygen

---

[4] More details in [Stievano, nd].

supply measures that is not solely based on standard statistical methods. Indeed, machine learning algorithms could be built to predict the role of vessels in oxygenation of brain tissue, starting from the features extracted in chapters 3 and 4.

7 Bibliography

[Abramowitz and Stegun, 1970] Abramowitz, M. and Stegun, I. A. (1970). *Handbook of Mathematical Functions with Formulas, Graphs, and Mathematical Tables.* Dover. Ninth printing.

[Agarwal and Carare, 2021] Agarwal, N. and Carare, R. (2021). Cerebral vessels: An overview of anatomy, physiology, and role in the drainage of fluids and solutes. *Front. Neurol.*, 11(611485):page 1.

[Agbangba et al., 2024] Agbangba, C. E., Aide, E. S., Honfo, H., and Kakai, R. G. (2024). On the use of post-hoc tests in environmental and biological sciences: A critical review. *Heliyon*, 10(3):e25131.

[Altman and Dittmer, 1971] Altman, P. L. and Dittmer, D. S. (1971). *Respiration and Circulation.*

[Barbee and Cokelet, 1971] Barbee, J. H. and Cokelet, G. R. (1971). The fahraeus effect. *Microvascular Research*, 3(1):6–16.

[Bentley et al., 1993] Bentley, T. B., Meng, H., and Pittman, R. N. (1993). Temperature dependence of oxygen diffusion and consumption in mammalian striated muscle. *American Journal of Physiology - Heart and Circulatory Physiology*, 264(6):H1825–H1830.

[Blinder et al., 2013] Blinder, P., Tsai, P. S., Kaufhold, J., Knutsen, P., Suhl, H., and Kleinfeld, D. (2013). The cortical angiome: an interconnected vascular network with noncolumnar patterns of blood flow. *Nature Neuroscience*, 16(7):889–897.

[Chandran et al., 2012] Chandran, K. B., Yoganathan, A. P., and Rittgers, S. E. (2012). *Biofluid Mechanics: The Human Circulation, Second Edition.* CRC Press.

[Cho and Cho, 2011] Cho, Y. I. and Cho, D. J. (2011). Hemorheology and microvascular disorders. *Korean circulation journal*, 41(6):287–295.

[Christoforides et al., 1969] Christoforides, C., Laasberg, L. H., and Hedley-Whyte, J. (1969). Effect of temperature on solubility of o_2 in human plasma. *Journal of Applied Physiology*, 26(1):56–60.

[Clark et al., 1985] Clark, A., Federspiel, W., Clark, P., and Cokelet, G. (1985). Oxygen delivery from red cells. *Biophysical Journal*, 47(2):171–181.

[Corrada et al., 2016] Corrada, M. M., Sonnen, J. A., Kim, R. C., and Kawas, C. H. (2016). Microinfarcts are common and strongly related to dementia in the oldest-old: The 90+ study. *Alzheimer's dementia : the journal of the Alzheimer's Association*, 12(8):900–908.

[Daniel and Cross, 2013] Daniel, W. W. and Cross, C. L. (2013). *Biostatistics: A Foundation for Analysis in the Health Sciences*. Wiley. Chapter 8 for ANOVA and t-test, chapter 13 for nonparametric tests.

[Dean, 2005] Dean, L. (2005). *Blood Groups and Red Cell Antigens*. Internet version. Chapter 1, Blood and the cells it contains.

[Eggleton et al., 2000] Eggleton, C., Vadapalli, A., Roy, T., and Popel, A. (2000). Calculations of intracapillary oxygen tension distributions in muscle. *Mathematical Biosciences*, 167(2):123–143.

[Farine and Carter, 2022] Farine, D. R. and Carter, G. G. (2022). Permutation tests for hypothesis testing with animal social network data: Problems and potential solutions. *Methods in Ecology and Evolution*, 13(1):144–156.

[Feihl et al., 2009] Feihl, F., Liaudet, L., and Waeber, B. (2009). The macrocirculation and microcirculation of hypertension. *Current Science Inc*, 11:pages 182–189.

[Field, 2024] Field, A. (2024). *Discovering Statistics Using IBM SPSS Statistics*. Sage Pubns Ltd. Chapter about ANCOVA analysis (11).

[Goldman, 2008] Goldman, D. (2008). Theoretical models of microvascular oxygen transport to tissue. *Microcirculation*, 15(8):795–811.

[Goldman and Popel, 2000] Goldman, D. and Popel, A. (2000). A computational study of the effect of capillary network anastomoses and tortuosity on oxygen transport. *Journal of Theoretical Biology*, 206(2):181–194.

[Hall and Hall, 2020] Hall, J. E. and Hall, M. E. (2020). *Guyton and Hall Textbook of Medical Physiology*. Elsevier - Health Sciences Division. Chapter 61, page 743 for the brain and chapter 16, page 177 for the capillaries dimension.

[Han, 2012] Han, H. C. (2012). Twisted blood vessels: symptoms, etiology and biomechanical mechanisms. *Journal of vascular research*, 49(3):185–197.

[Hart et al., 2022] Hart, J., Weiss, M., and Brent, L. e. a. (2022). Common permutation methods in animal social network analysis do not control for non-independence. *Behav Ecol Sociobiol*, 76(151).

[Hellums, 1977] Hellums, J. D. (1977). The resistance to oxygen transport in the capillaries relative to that in the surrounding tissue. *Microvascular Research*, 13(1):131–136.

[Hirsch et al., 2012] Hirsch, S., Reichold, J., Schneider, M., Szekely, G., and Weber, B. (2012). Topology and hemodynamics of the cortical cerebrovascular system. *JCBFM*, 32:952–957.

[Hoque et al., 2021] Hoque, M. M., Abdelazim, H., Jenkins-Houk, C., Wright, D., Patel, B. M., and Chappell, J. C. (2021). The cerebral microvasculature: Basic and clinical perspectives on stroke and glioma. *Microcirculation (New York, N.Y. : 1994)*, 28(3):e12671.

[Ji et al., 2021] Ji, X., Ferreira, T., Friedman, B., Liu, R., Liechty, H., Bas, E., Chandrashekar, J., and Kleinfeld, D. (2021). Brain microvasculature has a common topology with local differences in geometry that match metabolic load. *Neuron*, 109(7):1168–1187.e13.

[Keppel, 1991] Keppel, G. (1991). *Design and Analysis: A Researcher's Handbook*. Pearson.

[Kim, 2015] Kim, H. Y. (2015). Statistical notes for clinical researchers: post-hoc multiple comparisons. *Restorative dentistry endodontics*, 40(2):172–176.

[Koch, 2020] Koch, T. (2020). *Mixed-dimension embedded models for flow and transport processes in porous media with embedded tubular network systems*. Universität Stuttgart, PhD thesis.

[Koch, 2022] Koch, T. (2022). Projection-based resolved interface 1d-3d mixed-dimension method for embedded tubular network systems. *Computers Mathematics with Applications*, 109:15–29.

[Koch et al., 2018] Koch, T., Heck, K., Schröder, N., Class, H., and Helmig, R. (2018). A new simulation framework for soil–root interaction, evaporation, root growth, and solute transport. *Vadose Zone Journal*, 17(1).

[Krogh, 1919] Krogh, A. (1919). The number and distribution of capillaries in muscles with calculations of the oxygen pressure head necessary for supplying the tissue. *The Journal of Physiology*, 52(6):409–415.

[Kövari et al., 2013] Kövari, E., Herrmann, F. R., Hof, P. R., and Bouras, C. (2013). The relationship between cerebral amyloid angiopathy and cortical microinfarcts in brain ageing and alzheimer's disease. *Neuropathology and applied neurobiology*, 39(5):498–509.

[Laerd Statistics, 2025] Laerd Statistics (Accessed October 7, 2025). Mann–Whitney U test using SPSS Statistics. `https://statistics.laerd.com/spss-tutorials/mann-whitney-u-test-using-spss-statistics.php`.

[Lecoq et al., 2011] Lecoq, J., Parpaleix, A., Roussakis, E., Ducros, M., Goulam Houssen, Y., Vinogradov, S. A., and Charpak, S. (2011). Simultaneous two-photon imaging of oxygen and blood flow in deep cerebral vessels. *Nature medicine*, 17(7):893–898.

[Liu et al., 1994] Liu, C. Y., Eskin, S. G., and Hellums, J. D. (1994). The oxygen permeability of cultured endothelial cell monolayers. In *Advances in Experimental Medicine and Biology*, pages 723–730. Springer Nature.

[Liu et al., 2024] Liu, Y., Bech, P., Tamura, K., Délez, L. T., Crochet, S., and Petersen, C. C. (2024). Cell class-specific long-range axonal projections of neurons in mouse whisker-related somatosensory cortices. *eLife Sciences Publications, Ltd.*

[Lyons et al., 2016] Lyons, D. G., Parpaleix, A., Roche, M., and Charpak, S. (2016). Mapping oxygen concentration in the awake mouse brain. *eLife*, 5:e12024.

[Lücker, 2017] Lücker, A. (2017). *Computational Modeling of Oxygen Transport in the Microcirculation: From an Experiment-Based Model to Theoretical Analyses.* ETH Zürich. PhD Thesis.

[Mahler et al., 1985] Mahler, M., Louy, C., Homsher, E., and Peskoff, A. (1985). Reappraisal of diffusion, solubility, and consumption of oxygen in frog skeletal muscle, with applications to muscle energy balance. *The Journal of General Physiology*, 86(1):105–134.

[Maldonado and Alsayouri, 2025] Maldonado, K. and Alsayouri, K. (2025). *Physiology, Brain.* StatPearls Publishing.

[Maneewongvatana and Mount, 1999] Maneewongvatana, S. and Mount, D. M. (1999). Analysis of approximate nearest neighbor searching with clustered point sets. *CoRR*, cs.CG/9901013.

[Midway et al., 2020] Midway, S., Robertson, M., Flinn, S., and Kaller, M. (2020). Comparing multiple comparisons: practical guidance for choosing the best multiple comparisons test. *PeerJ*, 8:e10387.

[Moeini et al., 2018] Moeini, M., Lu, X., Avti, P. K., Damseh, R., Bélanger, S., Picard, F., Boas, D., Kakkar, A., and Lesage, F. (2018). Compromised microvascular oxygen delivery increases brain tissue vulnerability with age. *Scientific Reports*, 8(1):8219.

[Moini et al., 2023] Moini, J., Gutierrez, A., and Avgeropoulos, N. (2023). *Clinical Neuroepidemiology of Acute and Chronic Disorders*. Academic Press.

[Nishimura et al., 2007] Nishimura, N., Schaffer, C. B., Friedman, B., Lyden, P. D., and Kleinfeld, D. (2007). Penetrating arterioles are a bottleneck in the perfusion of neocortex. *Proceedings of the National Academy of Sciences of the United States of America*, 104(1):365–370.

[Obrist, 2022] Obrist, D. (2022). Blood rheology lecture. YouTube video. Accessed: 2025-10-26.

[Popel, 1978] Popel, A. S. (1978). Analysis of capillary-tissue diffusion in multicapillary systems. *Mathematical Biosciences*, 39(3-4):187–211.

[Pries et al., 1990] Pries, A. R., Secomb, T. W., Gaehtgens, P., and Gross, J. F. (1990). Blood flow in microvascular networks. experiments and simulation. *Circulation research*, 67(4):826–834.

[Raju and Tadi, 2025] Raju, H. and Tadi, P. (2025). *Neuroanatomy, Somatosensory Cortex*. Treasure Island (FL): StatPearls Publishing.

[Rehman and Rehman, 2023] Rehman, I. and Rehman, A. (2023). *Anatomy, Thorax, Heart*. StatPearls Publishing, Treasure Island, FL, updated 28 aug 2023 edition. Accessed 31 Oct 2025.

[Sakadžić et al., 2014] Sakadžić, S., Mandeville, E. T., Gagnon, L., Musacchia, J. J., Yaseen, M. A., Yucel, M. A., Lefebvre, J., Lesage, F., Dale, A. M., Eikermann-Haerter, K., Ayata, C., Srinivasan, V. J., Lo, E. H., Devor, A., and Boas, D. A. (2014). Large arteriolar component of oxygen delivery implies a safe margin of oxygen supply to cerebral tissue. *Nature communications*, 5(5734).

[Sauer, 2012] Sauer, T. (2012). *Numerical Analysis*. Pearson.

[Schmid, 2017] Schmid, F. (2017). *Cerebral Blood Flow Modeling with Discrete Red Blood Cell Tracking, Analyzing Microvascular Networks and their Perfusion*. ETH Zürich. PhD Thesis.

[Schmid et al., 2017a] Schmid, F., Barret, M., Jenny, P., and Weber, B. (2017a). Vascular density and distribution in neocortex. *NeuroImage*.

[Schmid et al., 2021] Schmid, F., Conti, G., Jenny, P., and Weber, B. (2021). The severity of microstrokes depends on local vascular topology and baseline perfusion. *eLife*, 10(e60208):pages 1–25.

[Schmid et al., 2017b] Schmid, F., Tsai, P. S., Kleinfeld, D., J. P., and Weber, B. (2017b). Depth-dependent flow and pressure characteristics in cortical microvascular networks. *PLoS computational biology*, 13(2):e1005392.

[Secomb and Hsu, 1988] Secomb, T. W. and Hsu, R. (1988). Analysis of oxygen delivery to tissue by microvascular networks. In Mochizuki, M., Honig, C. R., Koyama, T., Goldstick, T. K., and Bruley, D. F., editors, *Oxygen Transport to Tissue X*, pages 95–103. Springer US, Boston, MA.

[Secomb and Pries, 2013] Secomb, T. W. and Pries, A. R. (2013). Blood viscosity in microvessels: experiment and theory. *Comptes rendus. Physique*, 14(6):470–478.

[Shih et al., 2013] Shih, A. Y., Blinder, P., Tsai, P. S., Friedman, B., Stanley, G., Lyden, P. D., and Kleinfeld, D. (2013). The smallest stroke: occlusion of one penetrating vessel leads to infarction and a cognitive deficit. *Nature neuroscience*, 16(1):55–63.

[Skrodzki, 2019] Skrodzki, M. (2019). The k-d tree data structure and a proof for neighborhood computation in expected logarithmic time. *ArXiv*, abs/1903.04936.

[Smith et al., 2012] Smith, E. E., Schneider, J. A., Wardlaw, J. M., and Greenberg, S. M. (2012). Cerebral microinfarcts: the invisible lesions. *The Lancet. Neurology*, 11(3):272–282.

[Stievano, nd] Stievano, G. (n.d.). *PhD Thesis (in progress)*. Universität Bern, PhD Thesis.

[Sultana et al., 2024] Sultana, O. F., Bandaru, M., Islam, M. A., and Reddy, P. H. (2024). Unraveling the complexity of human brain: Structure, function in healthy and disease states. *Ageing Research Reviews*, 100:102414.

[Taylor and Bordoni, 2025] Taylor, A. and Bordoni, B. (2025). *Histology, Blood Vascular System*. StatPearls.

[Toksvang and Berg, 2013] Toksvang, L. N. and Berg, R. M. G. (2013). Using a classic paper by robin fåhraeus and torsten lindqvist to teach basic hemorheology. *Advances in Physiology Education*, 37(2):129–133.

[Ulrik, 2001] Ulrik, B. (2001). A faster algorithm for betweenness centrality. *Journal of Mathematical Sociology*, 25(2):163–177.

[Ulrik, 2008] Ulrik, B. (2008). On variants of shortest-path betweenness centrality and their generic computation. *Social Networks*, 30(2):136–145.

[van Steen, 2010] van Steen, M. (2010). *Graph Theory and Complex Networks: An Introduction*. Maarten van Steen.

[Verma and Abdel-Salam, 2019] Verma, J. P. and Abdel-Salam, A.-S. G. (2019). *Testing Statistical Assumptions in Research*. Wiley. Chapter 4 for ANOVA and t-test, chapter 5 for nonparametric tests.

[Wilcox, 2021] Wilcox, R. R. (2021). *Introduction to Robust Estimation and Hypothesis Testing (Statistical Modeling and Decision Science)*. Academic Press. Chapter about ANCOVA analysis.

[Zhang et al., 2015] Zhang, C., Bélanger, S., Pouliot, P., and Lesage, F. (2015). Measurement of local partial pressure of oxygen in the brain tissue under normoxia and epilepsy with phosphorescence lifetime microscopy. *PLoS ONE*, 10(8):e0135536.

8 Appendix

A Model and simulations

Conservation of mass proof

To prove conservation of mass between the 1d and 3d compartments, let $\mathcal{V} \subset \Omega$ be an arbitrary section of the tissue and let $\mathcal{V}_\Lambda = \mathcal{V} \cap \Omega_\Lambda$. The transmembrane flux density into each point $x \in \mathcal{V}$ can be expressed as $q_c(x)$ or as $q_c(x)\mathbb{1}_{\mathcal{V}_\Lambda}(x)$, where $\mathbb{1}_{\mathcal{V}_\Lambda}(x)$ is the indicator function of $\mathcal{V}_\Lambda$. This transmembrane flux density comes from the subset of the vasculature that is embedded into it. In the 1d parametrization, such subset can be written as $\mathcal{L} = \lambda(\mathcal{V}_\Lambda)$. Exploiting 2.5, with $f(x) = q_c(x)\mathbb{1}_{\mathcal{V}_\Lambda}(x)$, it is possible to say that:

$$\int_{\mathcal{V}} q_c(x)dx = \int_{\mathcal{V}} q_c(x)\mathbb{1}_{\mathcal{V}_\Lambda}(x)dx = \int_{\Omega} q_c(x)\mathbb{1}_{\mathcal{V}_\Lambda}(x)dx = \int_{\Omega} -\hat{q}_c(\lambda(x))\delta_\Lambda(x)\mathbb{1}_{\mathcal{V}_\Lambda}(x)dx \tag{8.1}$$

$$= \int_{\Omega} -\hat{q}_c(\lambda(x))\delta_\Lambda(x)\mathbb{1}_{\mathcal{L}}(\lambda(x))dx \overset{(2.5)}{=} \int_{\Lambda} -\hat{q}_c(\lambda)\mathbb{1}_{\mathcal{L}}(\lambda)d\lambda = \int_{\mathcal{L}} -\hat{q}_c(\lambda)d\lambda \tag{8.2}$$

This means that the transmembrane flux in the 3d setting into an arbitrary section of the tissue $\mathcal{V}$, i.e. $\int_{\mathcal{V}} q_c(x)dx$, is equal to the outgoing transmembrane flux in the 1d setting in the corresponding portion $\mathcal{L}$ of the 1d domain, that is $\int_{\mathcal{L}} -\hat{q}_c(\lambda)d\lambda$. Conservation of mass from one compartment to the other is thus ensured.

Cylinder Surface Method

A more detailed explanation of the Cylinder Surface Method [Koch, 2022] is provided, aimed at computing the source term q_C. Let $\theta = \{(u_{i,\theta}, v_{i,\theta})\}_{1\leq i \leq n_\theta}$ be a vessel, where each $(u_{i,\theta}, v_{i,\theta}) \in E$ is a 1d element (see chapters 3, 4 for the definitions). The Cylinder Surface Method first retrieves the set $\mathcal{K}_{i,\theta}$ of finite volumes that intersect the walls of each 1d element, by considering the position of the 1d element and the radius of θ. Note that $\mathcal{K}_{i,\theta}$ is an approximation of the surface of a cylinder, hence the name of the method. Let $\lambda_{i,\theta}$ be the centre of the 1d element and $C_{i,\theta}$ be the circumference centered in $\lambda_{i,\theta}$, with radius equal to that of θ. The value of $\hat{q}_{C,(i,\theta)}$ is computed as follows:

$$\hat{q}_{C,(i,\theta)} = D_W \alpha_{pl}(1-\sigma)(P^{\circ}_{T,(i,\theta)} - P_{pl,(i,\theta)})|C_{i,\theta}| \tag{8.3}$$

where $P^{\circ}_{T,(i,\theta)} = \frac{1}{|C_{i,\theta}|}\int_{C_{i,\theta}} P_T$ is evaluated numerically and $P_{pl,(i,\theta)}$ is the oxygen partial pressure in plasma in $\lambda_{i,\theta}$. The source term $q_{C,(i,\theta)}$ is obtained distributing $\hat{q}_{C,(i,\theta)}$ on $\mathcal{K}_{i,\theta}$, as detailed in [Koch, 2022]. Figure 8.1, taken from [Koch, 2022], visually shows this procedure on a cross-section of a capillary.

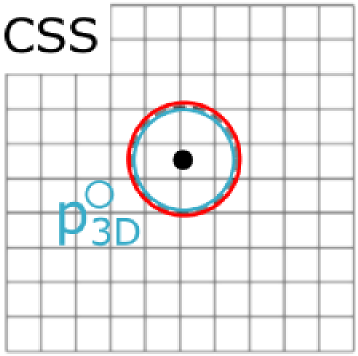

Figure 8.1: Visual representation of the Cylinder Surface Method (CSS) on a cross section of a capillary. The black dot represents the 1d element. p°_{3D} is the perimeter average on C_θ, i.e. $P^{\circ}_{T,(i,\theta)}$. The blue and red circles overlap with the circumference C_θ centered in the black dot. They represent respectively where P_T is evaluated to compute $\hat{q}_{C,(i,\theta)}$ and where the source term $q_{C,(i,\theta)}$ is placed.

.

Parameters of the model

The table 8.1 reports the values of the parameters of the oxygen supply model presented in chapter 2.

Par.	**Description**	**Value**	**Unit of measure**	**Reference**
α_{RBC}	Oxygen solubility in RBCs	$3.38 \cdot 10^{-5}$	$\mathrm{m}^3\mathrm{O}_2$ mmHg^{-1} m^{-3}	[Altman and Dittmer, 1971]
α_{pl}	Oxygen solubility in plasma	$2.82 \cdot 10^{-5}$	$\mathrm{m}^3\mathrm{O}_2$ mmHg^{-1} m^{-3}	[Christoforides et al., 1969]
$P_{\mathrm{RBC},50}$	Value of P_{RBC} at hemoglobin half saturation	47.9	mmHg	[Lücker, 2017]
K	Dissociation rate constant	44	s^{-1}	[Clark et al., 1985]
n	Hill exponent	2.65	Adimensional	[Clark et al., 1985]
D_{W}	Oxygen diffusivity in capillary wall	$8.73 \cdot 10^{-10}$	m^2 s^{-1}	[Liu et al., 1994]
σ	Oxygen permeability	0	Adimensional	model assumption
α_{T}	Oxygen solubility in tissue	$3.89 \cdot 10^{-5}$	$\mathrm{m}^3\mathrm{O}_2$ mmHg^{-1} m^{-3}	[Mahler et al., 1985]
D_{T}	Oxygen diffusivity in tissue	$2.41 \cdot 10^{-9}$	m^2 s^{-1}	[Bentley et al., 1993]
M_0	Oxygen consumption in tissue	$4 \cdot 10^{-4}$	$\mathrm{m}^3\mathrm{O}_2$ m^{-3} s^{-1}	[Lücker, 2017]]
$P_{\mathrm{T,crit}}$	Critical P_{T}	1.0	mmHg	[Goldman, 2008]

Table 8.1: Parameters adopted in simulations. *Par.* stands for *Parameter*.

B Finite difference methods

In sections 4.4.4 and 5.4.1, two finite difference methods are employed to compute respectively the gradient term and the laplacian operator.

Gradient term

To numerically evaluate the term $\nabla P_T(w_i) = [\partial_x P_T(w_i), \partial_y P_T(w_i), \partial_z P_T(w_i)]^T$, each partial derivative $\partial_j P_T(w_i)$, $j \in \{x, y, z\}$ is computed via a five point discretization approximation scheme [Sauer, 2012]:

$$\partial_j P_T(w_i) \approx \frac{-P_T(w^j_{i+2}) + 8P_T(w^j_{i+1}) - 8P_T(w^j_{i-1}) + P_T(w^j_{i-2})}{12l} \tag{8.4}$$

where $w^j_{i+q}, q \in \mathbb{Z}$ represents the cell center that is q positions ahead or behind in the j-th direction; l is the side length of a 3d finite element cube, that corresponds to the distance between the two cell centers of adjacent cubes.

Laplacian operator

The term $\Delta P_T(w_i) = \nabla \cdot (\nabla P_T(w_i)) = \partial_{xx} P_T(w_i) + \partial_{yy} P_T(w_i) + \partial_{zz} P_T(w_i)$ is numerically approximated in the following way. Each term $\partial_{xx} P_T(w_i)$ is computed thanks to a fourth-order central finite-difference stencil [Abramowitz and Stegun, 1970]:

$$\partial_{xx} P_T(w_i) \approx \frac{-P_T(w^j_{i+2}) + 16P_T(w^j_{i+1}) - 30P_T(w_i) + 16P_T(w^j_{i-1}) - P_T(w^j_{i-2})}{12l^2} \tag{8.5}$$

where $w^j_{i+q}, q \in \mathbb{Z}$ and l are defined as in the previous paragraph. The approximations of the second partial derivatives are subsequently summed.

Note: clamping

Note that in 8.4 and 8.5, as the domain Ω is bounded, w^j_{i+q} could lay outside of Ω, for some values of i and q. To avoid that, the indices are clamped to the valid grid range. In other words, if $i + q$ falls outside the domain bounds, it is set to the nearest valid boundary value.